Piezooptics in Non-Uniform Mechanical Fields

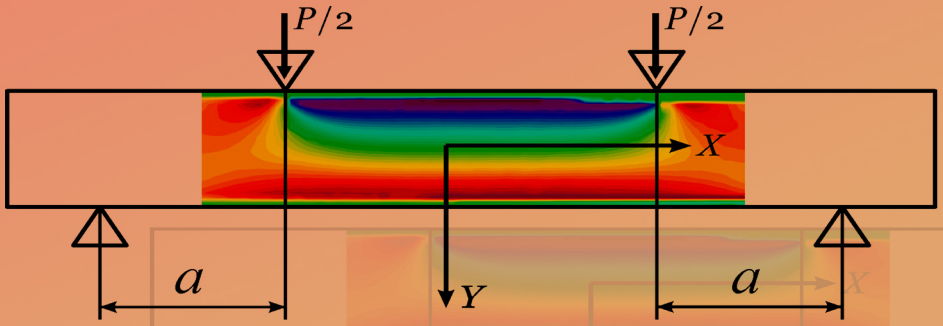

Rostyslav Vlokh
Igor Skab
Oleh Krupych
Dmitro Adamenko

Piezooptics in Non-Uniform Mechanical Fields

Piezooptics in Non-Uniform Mechanical Fields

By

Rostyslav Vlokh, Igor Skab,
Oleh Krupych and Dmitro Adamenko

Cambridge
Scholars
Publishing

Piezooptics in Non-Uniform Mechanical Fields

By Rostyslav Vlokh, Igor Skab, Oleh Krupych and Dmitro Adamenko

This book first published 2022

Cambridge Scholars Publishing

Lady Stephenson Library, Newcastle upon Tyne, NE6 2PA, UK

British Library Cataloguing in Publication Data
A catalogue record for this book is available from the British Library

ISBN (10): 1-5275-7689-2
ISBN (13): 978-1-5275-7689-6

TABLE OF CONTENTS

INTRODUCTION

The discovery of the effects of parametric optics, in particular, the piezooptic effect by D. Brewster in 1818 [1, 2], the magnetooptic effect by M. Faraday in 1845 [3], quadratic and linear electrooptic effects by Kerr and Pockels in 1875 and 1893, respectively [4, 5, 6] and the electrogyration effect by O.G. Vlokh in the second half of the XX century [7], took place over almost two centuries, which were associated primarily with significant experimental difficulties of studying these subtle phenomena. In addition, the absence of a symmetry-tensor apparatus of crystal physics had a significant effect on the long duration of this process. So, the equations for optical indicatrix deformation under the electrooptic effect for all point symmetry groups were obtained only in the 60s of the XX century [8, 9].

Despite the classical nature of the phenomena of parametric optics, they still remain the fundamental basis for the development of various optical devices. In particular, the photoelastic effect has long been used for non-destructive control of mechanical stresses of transparent optical elements, parts, and structures (including in tensor tomography), measurement of mechanical stress or pressure by a non-contact method, modulation of the state of polarization of optical radiation, and the like. In turn, in recent years, it has turned out that acoustooptic control of light radiation can be used in the capture of microparticles with an optical beam and manipulating them, for addressing optical beams that have various quantum states, in the framework of quantum cryptography and optical computer information processing, as well as in formation of a Bose-Einstein condensate [10].

The above circumstances make the further development of piezooptic materials science important and relevant. However, the existing experimental methods for studying the piezooptic properties of crystals are quite imperfect and lead to significant errors, which, in turn, does not allow to derive the most effective geometries in certain anisotropic crystalline materials.

This monograph is intended to familiarize the reader with the 2D-polarimetric and interferometric methods developed by the authors of the study of the piezooptic effect under the action of inhomogeneous mechanical stresses which have in advance known distribution across the

sample (namely, diametrical compression, mechanical torsion, and four-point bending). In addition, the monograph presents the results of experimental studies of the photoelastic properties of crystals, which provide for the determination of complete matrices of piezooptic and elastooptic coefficients.

SECTION 1

FUNDAMENTALS OF PHOTOELASTICITY. ANALYSIS OF STRESS HOMOGENEITY IN SAMPLES IN CLASSICAL PIEZOOPTIC EXPERIMENTS

1.1. Photoelasticity as a phenomenon of parametric optics

In the most general case, photoelasticity is an effect of changes in the refractive indices of optical medium under the influence of mechanical strains. Today, the phenomenon of photoelasticity is widely used in many fields of science and technology, in particular when checking mechanical stresses in transparent bodies [11–13], in remote optical sensors of stresses [14] and accelerometers [15–17], tensor-field stress tomography [18–22], and polarizing optical modulators [23, 24]. Moreover, of great importance is utilization of the photoelastic effect in various acoustooptic devices (deflectors, modulators, spectral filters, etc.), which are widely used in many modern techniques [25–28]. In addition, the photoelastic properties of materials should be taken into account when developing electrooptic devices. Practical applications of the photoelasticity effect mentioned above require complete and thorough information on so-called piezooptic and elastooptic coefficients.

The photoelasticity can be termed as "ancient" among various phenomena of parametric optics (i.e., the optics of media in external or internal fields). The first description of the photoelastic effect in optically isotropic media, amorphous solids and cubic crystals has been made by David Brewster at the beginning of the 19th century [1, 2]. Within the framework of this theory, an optical birefringence Δn induced by a mechanical stress σ is expressed as follows:

$$\Delta n = K\sigma. \tag{1.1}$$

Different terms are used to denote the K coefficient. In particular, it is called a Brewster constant, a relative piezooptic coefficient, a relative photoelastic coefficient, or a stress-optical coefficient. The latter term is chiefly used by manufacturers of optical glass as a standard characteristic of any optical material [29, 30].

Since the scalar equation (1.1) is valid only for optically isotropic materials, one has to pass to a tensor relation in a more general case of anisotropic material. This relation has been suggested by Pockels [6]:

$$\delta B_{ij} = \sum_{k=1}^{3}\sum_{l=1}^{3} \pi_{ijkl}\sigma_{kl} \quad (i, j, k, l = 1\ldots3), \tag{1.2}$$

where δB_{ij} is the increment of dielectric impermeability tensor component (a so-called tensor of optical polarization constant) B_{ij} and σ_{kl} denote the component of mechanical stress tensor, and π_{ijkl} the tensor component of piezooptic coefficients, which is measured in the units of $m^2/N = Pa^{-1} = 10^{12}$ B (B = Brewster).

Neglecting the phenomena associated with antisymmetricity of the dielectric impermeability and the mechanical stress tensors (i.e., in the approximation $B_{ij} = B_{ji}$ and $\sigma_{kl} = \sigma_{lk}$), one can rewrite equation (1.2) in a matrix form (or a Voigt notation):

$$\delta B_{\lambda} = \pi_{\lambda\mu}\sigma_{\mu} \quad (\lambda, \mu = 1\ldots6), \tag{1.3}$$

where $\sigma_1 = \sigma_{11}$, $\sigma_2 = \sigma_{22}$, $\sigma_3 = \sigma_{33}$, $\sigma_4 = \sigma_{23}$, $\sigma_5 = \sigma_{13}$ and $\sigma_6 = \sigma_{12}$, $\delta B_1 = \delta B_{11}$, $\delta B_2 = \delta B_{22}$, $\delta B_3 = \delta B_{33}$, $\delta B_4 = \delta B_{23}$, $\delta B_5 = \delta B_{13}$ and $\delta B_6 = \delta B_{12}$, $\pi_{\lambda\mu} = \pi_{ijkl}$ if $\mu = 1\ldots3$ and $\pi_{\lambda\mu} = 2\pi_{ijkl}$ if $\mu = 4\ldots6$. Here and below, the Einstein rule is used for summation over repeating indices.

Equations (1.2) and (1.3) are mathematical formulations of the piezooptic effect. If the values δB_{λ} are expressed through mechanical strains, the term "elastooptic effect" is mainly used. In the matrix form, it can be written as

$$\delta B_{\lambda} = p_{\lambda\mu}\varepsilon_{\mu} \quad (\lambda, \mu = 1\ldots6), \tag{1.4}$$

where $p_{\lambda\mu}$ and ε_{μ} are the components of elastooptic coefficients and mechanical strain tensors, respectively.

It is known that the mechanical strain tensor and the mechanical stress tensor are coupled via the Hooke's law:

$$\varepsilon_\mu = S_{\mu\theta}\sigma_\theta, \tag{1.5}$$

$$\sigma_\mu = C_{\mu\theta}\varepsilon_\theta, \tag{1.6}$$

where $S_{\mu\theta}$ and $C_{\mu\theta}$ are the components of elastic compliance and elastic stiffness tensors, respectively.

Thus, the piezooptic and elastooptic coefficients are coupled through the $S_{\mu\theta}$ and $C_{\mu\theta}$ tensors:

$$\begin{aligned} \pi_{\lambda\mu} &= p_{\lambda\theta}S_{\theta\mu}, \\ p_{\lambda\mu} &= \pi_{\lambda\theta}C_{\theta\mu}. \end{aligned} \tag{1.7}$$

Therefore, by determining experimentally the complete matrices of two of the four tensors involved in the relations (1.7), one can calculate the two other tensors.

The values δB_λ can be expressed through a change in the refractive indices, using the relation $B_q = (n_q)^{-2}$ and differentiating it:

$$\delta B_q = -\frac{2}{n_q^3}\delta n_q. \tag{1.8}$$

Here n_q implies the initial refractive index and δn_q the change in the refractive index occurring due to mechanical stresses (or strains).

Substituting formula (1.8) into (1.3) and (1.4), one obtains the relation that links the δn_q values with the mechanical stresses or strains:

$$\begin{aligned} \delta n_q &= -\frac{1}{2}n_q^3\pi_{qm}\sigma_m = K_{qm}\sigma_m, \\ \delta n_q &= -\frac{1}{2}n_q^3 p_{qm}\varepsilon_m, \end{aligned} \tag{1.9}$$

where K_{qm} denotes the photoelastic coefficient.

It follows from the relation (1.3) that, in general, the piezooptic tensor (as well as the elastooptic one) can be represented by a 6×6 matrix, which contains 36 independent coefficients. For a convenience, this matrix is usually divided into four sub-matrices **A**, **B**, **C** and **D**:

$$\pi_{qm} = \left[\begin{array}{ccc:ccc} \pi_{11} & \pi_{12} & \pi_{13} & \pi_{14} & \pi_{15} & \pi_{16} \\ \pi_{21} & \pi_{22} & \pi_{23} & \pi_{24} & \pi_{25} & \pi_{26} \\ \pi_{31} & \pi_{32} & \pi_{33} & \pi_{34} & \pi_{35} & \pi_{36} \\ \hdashline \pi_{41} & \pi_{42} & \pi_{43} & \pi_{44} & \pi_{45} & \pi_{46} \\ \pi_{51} & \pi_{52} & \pi_{53} & \pi_{54} & \pi_{55} & \pi_{56} \\ \pi_{61} & \pi_{62} & \pi_{63} & \pi_{64} & \pi_{65} & \pi_{66} \end{array}\right] = \begin{bmatrix} \mathbf{A} & \mathbf{B} \\ \mathbf{C} & \mathbf{D} \end{bmatrix}, \tag{1.10}$$

$$\mathbf{A} = \begin{bmatrix} \pi_{11} & \pi_{12} & \pi_{13} \\ \pi_{21} & \pi_{22} & \pi_{23} \\ \pi_{31} & \pi_{32} & \pi_{33} \end{bmatrix}, \mathbf{B} = \begin{bmatrix} \pi_{14} & \pi_{15} & \pi_{16} \\ \pi_{24} & \pi_{25} & \pi_{26} \\ \pi_{34} & \pi_{35} & \pi_{36} \end{bmatrix},$$
$$\mathbf{C} = \begin{bmatrix} \pi_{41} & \pi_{42} & \pi_{43} \\ \pi_{51} & \pi_{52} & \pi_{53} \\ \pi_{61} & \pi_{62} & \pi_{63} \end{bmatrix}, \mathbf{D} = \begin{bmatrix} \pi_{44} & \pi_{45} & \pi_{46} \\ \pi_{54} & \pi_{55} & \pi_{56} \\ \pi_{64} & \pi_{65} & \pi_{66} \end{bmatrix}. \tag{1.11}$$

The sub-matrix **A** includes the "principal" piezooptic coefficients that describe the changes in the principal components of the dielectric impermeability tensor (δB_1, δB_2 and δB_3). This corresponds to the change in the ellipsoid of refractive indices (or the so-called optical indicatrix) that occurs along the principal coordinate axes under the action of stretching or compressing stresses (i.e., under the action of normal components σ_1, σ_2 and σ_3 of the mechanical stress tensor). The sub-matrix **B** contains the "shift" (or "shifting") piezooptic coefficients that describe the changes in the optical indicatrix under the action of shear (shift) stresses (i.e., the shear components σ_4, σ_5 and σ_6 of the mechanical stress tensor). Finally, the "rotating" (see the sub-matrix **C**) and the "rotating-shifting" (the sub-matrix **D**) piezooptic coefficients describe the changes in the "rotating" components δB_4, δB_5 and δB_6 of the dielectric impermeability tensor (i.e., those that cause rotation of the optical indicatrix) under the action of normal (σ_1, σ_2 and σ_3) and shear (σ_4, σ_5 and σ_6) components of the mechanical stress tensor, respectively.

Symmetry of a material medium allows for reducing the number of independent components of the piezooptic and elastooptic tensors. In particular, the matrix (1.10) contains only twelve nonzero coefficients in case of an amorphous (glassy) material, of which only two coefficients are independent:

$$\pi_{qm} = \left[\begin{array}{ccc:ccc} \pi_{11} & \pi_{12} & \pi_{12} & 0 & 0 & 0 \\ \pi_{12} & \pi_{11} & \pi_{12} & 0 & 0 & 0 \\ \pi_{12} & \pi_{12} & \pi_{11} & 0 & 0 & 0 \\ \hdashline 0 & 0 & 0 & (\pi_{11}-\pi_{12}) & 0 & 0 \\ 0 & 0 & 0 & 0 & (\pi_{11}-\pi_{12}) & 0 \\ 0 & 0 & 0 & 0 & 0 & (\pi_{11}-\pi_{12}) \end{array}\right]. \quad (1.12)$$

For the crystals that belong to the cubic system, the number of independent components of the piezooptic and elastooptic tensors increases to three or four, while for the hexagonal system we have from six to eight components. In the same way, one can obtain seven to ten independent components for the tetragonal system, eight to twelve for the trigonal system, twelve for the orthorhombic system, twenty for the monoclinic system, and thirty six for the triclinic one.

1.2. Polarimetric method for measuring photoelastic constants

In experimental mechanics and glass production, various polarimetric methods [31–36] are commonly used to investigate photoelasticity properties. Historically, most of these methods have used visual or photographic recording of image of a sample, which is obtained in polarized light. At the end of the twentieth century, solid-state digital video cameras and computer technologies has been developed and widely spread. This has started production of the polarimeters for determining stress-induced optical birefringence, which are based upon digital image processing [37–43].

Over the past two decades, a number of 2D polarimeters (or imaging polarimeters) have been built at the O. G. Vlokh Institute of Physical Optics (Lviv, Ukraine) for the visible and infrared spectral ranges. All of them represent modifications of a basic 2D polarimeter configuration (Fig. 1-1) [44, 45]. This scheme includes a radiation source, a polarization generator, a sample under analysis, an analyzer, and an electronic section.

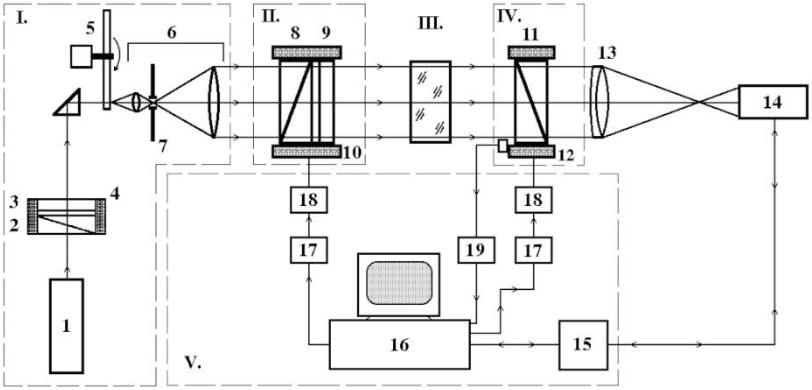

Fig. 1-1. Basic configuration of 2D polarimeter:
(I) radiation source: (1) gas laser, (2) linear polarizer, (3) quarter-wave plate, (4) rotation device, (5) coherence scrambler, (6) beam expander, (7) spatial filter;
(II) polarization generator: (8) linear polarizer, (9) quarter-wave plate, (10) rotation device,
(III) sample under analysis;
(IV) analyzer: (11) linear polarizer, (12) rotation device;
(V) electronic section: (15) video camera interface, (16) computer, (17) stepper motor controller, (18) stepper motor, (19) zero-position sensor controller of analyzer.
Adapted with permission from Vasylkiv, Y., Kvasnyuk, O., Krupych, O., Mys, O., Maksymuk, O., & Vlokh, R. (2009). Reconstruction of 3D stress fields basing on piezooptic experiment. Ukr. J. Phys. Opt., 10(1), 22–37. © O. G. Vlokh Institute of Physical Optics.

Now let us describe in brief the main sections of this configuration.

Radiation source. The objective of this section is to create an almost plane monochromatic light wave with circular polarization and controlled intensity. It includes a gas laser (1), a radiation-intensity controller (2)–(4), a coherence scrambler (5) and a beam expander (6) with a pinhole spatial filter (7). In our scheme, a helium-neon laser emits a monochromatic linearly polarized light with the wavelength 632.8 nm and the power 3 mW.

A radiation-intensity controller consists of a linear polarizer, i.e. a Glan prism (2) and a quarter-wave plate (3). Note that the fast axis of the quarter-wave plate makes the angle 45 deg with the transmission axis of polarizer. Taken together, these components form a circular polarizer, which is placed on a rotation device (4), which makes it possible to adjust the intensity of the incident light by rotating the circular polarizer around the axis of light beam. This rotation is controlled by a stepper motor.

After the radiation-intensity controller, the light beam passes through a coherence scrambler (5). The aim of this device is eliminating undesirable speckle patterns in the image, which arise from the interference of coherent laser light diffracted at the components of optical scheme. The coherence scrambler represents a grounded glass disk that scatters light with a speckle structure. This speckle structure is changing continuously, since this disk is being rotated using an electric motor. As a result of averaging that occurs during exposure of sample, the effect of "spotting" disappears and an improved image arises, which is like the image obtained with incoherent light.

After that, the light beam enters a beam expander (6), which is built according to a reciprocal Keppler telescopic system. To "clean" the beam from scattered and diffracted light, a spatial filter (7) (i.e., a pinhole diaphragm) is installed behind the first short-focus lens at the waist place. At the output of the beam expander, a collimated light beam with the diameter ~ 20 mm is obtained.

Hence, utilization of laser radiation source in the 2D polarimeter provides a high degree of monochromaticity and, at the same time, the coherence scrambler eliminates the speckle structure of images, which would have been otherwise inherent for the polarimetric systems based on monochromatic sources.

Finally, a high-quality collimated beam of circularly polarized light is obtained at the output of this section. This decreases any noises and increases the measurement accuracy.

Polarization generator. The objective of this section is to create a predetermined polarization state of the light wave, which is given by the azimuth and the ellipticity, at the entrance of sample. It includes a first linear polarizer (a Glan prism (8)) and a compensator (a quarter-wave plate (9)).

The ellipticity K of the light wave at the output of the polarization generator is determined by the angle φ between the fast axis of the compensator and the transmission axis of the linear polarizer. The actual value of the optical phase difference of the compensator Γ_c is slightly different from its ideal value of 90 deg. Then the actual value of the ellipticity K reads as

$$K = \tan(\varepsilon),\ \varepsilon = \frac{1}{2}\operatorname{asin}[\sin(\Gamma_c)\sin(2\varphi)], \tag{1.13}$$

where ε is the ellipticity angle. The azimuth θ of the polarization ellipse is determined by the angular position of the fast axis c and the Γ_c value:

$$\theta = c + \delta c,\ \tan(2\delta c) = \cos(\Gamma_c)\ \tan(2\varphi). \tag{1.14}$$

Here δc implies the azimuth correction associated with imperfections of the compensator.

Since the azimuth p of the linear polarizer and the angle φ between the transmission axis of the linear polarizer and the fast axis of the compensator are directly set during experiment, the parameter c becomes

$$c = p + \varphi. \tag{1.15}$$

Hence, by rotating the composite elliptical polarizer consisting of the linear polarizer and the compensator, any prescribed azimuth θ of the major axis of the polarization ellipse and any ellipticity K of the polarization can be set at the output.

A rotary device (10) enables rotation of the compensator (9) with respect to the linear polarizer (8), as well as joint rotation of the two latter components around the optical axis of the 2D polarimeter. Note that the composite elliptical polarizer is rotated by a stepper motor. As a consequence, the section of polarization generator provides a range of all possible azimuths from 0 to 180 deg and the range of ellipticities from –1 to +1.

Sample under test. Besides of a sample itself, this section also contains some additional devices. In particular, this can be a cuvette with immersion liquid, a device for rotating the sample or a loading device. The dimensions of the analyzed area of sample are determined by the diameter of collimated light beam at the output of the composite elliptical polarizer. In its turn, this diameter is given by the linear dimensions of the Glan polarization prism (8) and equals to ~ 20 mm.

Analyzer. The objective of this section is to analyze the polarization state of the light beam at the output of the sample. It comprises a second linear polarizer (a Glan prism (11)) arranged at a rotation device (12), which is controlled by a stepper motor. The rotation device is equipped with a zero-position sensor connected to a computer. This is due to a need in setting precisely a laboratory coordinate system when determining the azimuth angles.

After the light has passed through the analyzer, the image of spatial intensity distribution over the light beam section is formed, by means of a lens (13), in the plane of photosensitive matrix of a detector, a video camera (14). For example, it can be a camera based on a charge-coupled device. Then the sensitive area of the photodetector contains 795 horizontal and 596 vertical elements. The choice of the lens mentioned above depends on the

size of the sample under test, the resolution of the photodetector and the overall dimensions of the 2D polarimeter.

Electronic section. This section includes a video-camera interface (15), a computer (16), stepper-motor controllers (17), stepper motors (18) and a zero-position sensor controller of an analyzer (19). The interface of the video camera (15) provides reading the image of the intensity distribution line by line, digitizing it and transferring the corresponding data to the computer memory. According to control signals, the stepper-motor controllers (17) generate sequences of pulses, that are fed to windings of the stepper motors (18). They determine the directions of rotation of motors and the rotation angles

In the 2D polarimeter presented above, the rotary stages have the minimum rotation step of 0.012 deg and the accuracy 0.001 deg of angular positioning. Finally, the computer (16) carries out the operation control of all the elements of the polarimeter according to a preset measurement algorithm, accumulates and processes the data, and presents and saves the experimental results.

Original software of the 2D polarimeter forms a shell for controlling its work. In particular, it controls the stepper motors, reads the image from the video camera, presents it on the computer display, processes the overall image and the data for a certain image pixel, fits the data for angular dependences with the sine function, initialize the analyzer; “binds” the polarizer to the analyzer, calibrates the image shift arising from the analyzer rotations, implements the algorithm of polarization-optical measurements, and calculates the resultant Jones matrix of the optical system. Moreover, it enables one to control the 2D polarimeter in manual and automatic measurement mode.

The basic configuration of the 2D polarimeter considered above is universal in the sense that it provides implementing different methods for measuring the parameters of optical anisotropy, depending on the complexity of task designated by experimenter.

1.3. Non-uniformity of mechanical stresses in a sample under axial compression

A significant negative aspect of photoelasticity studies is that the piezooptic coefficients $\pi_{\lambda\mu}$ of crystals are usually measured with large errors. Quite often, the latter exceed tens of percents and, in some cases, become as large as the value of the coefficient itself (see, e.g., Refs. [46–48]).

To understand the reasons for this disappointing situation, one has to analyze a typical scheme of traditional photoelastic measurements

performed in crystal optics. For instance, the sample to which axial compression is applied has usually a shape of a parallelepiped close to a cube [49]. Usually, a strained sample is placed into a single-beam polarimeter or a double-arm interferometer (e.g., Michelson or Mach–Zender interferometers). Then the sample is irradiated by a laser beam with the diameter ~ 1 mm. As a rule, the mechanical strain is changed during the experiment in order to measure a so-called "half-wave mechanical strain". It is obvious that these experimental procedures contain a number of possible sources of measurement errors.

1.3.1. Experimental procedures and results

In order to visualize better the sources of measurement errors of the piezooptic coefficients, we use the same basic configuration of the 2D polarimeter [45] (see Fig. 1-1) and the measurement technique presented in the work [50]. To perform the measurements, the quarter-wave plate (9) is oriented so that its fast axis forms the angle 45 deg with the transmission axis of the polarizer (8). Then the circularly polarized light is formed at the output of the polarization generator. This light is incident on the sample which is prepared in the shape of a plane-parallel plate.

The propagation of light through the sample changes the state of light polarization. To determine the polarization state of the light emerged from the sample, the analyzer is rotated in the angular range from 0 to 180 deg with the step of 4.5 deg. Note that the sample image is recorded for every azimuthal position of the analyzer. Once the analyzer has reached the angle 90 deg, the light beam is shut out and the background image is recorded. The overall time of the measuring procedure is less than 30 seconds.

In case when the circularly polarized light enters the sample as described by the model of linear optical retarder, the light intensity I at the analyzer output is determined by the formula

$$I = \frac{I_0}{2}\left\{1 + \sin\Gamma \sin\left[2\left(a - \zeta\right)\right]\right\}, \tag{1.16}$$

with I_0 being the intensity of light incident on the sample, a the azimuth of the transmission axis of polarizer, ζ the orientation angle of the principal axes of cross-section of the optical indicatrix with the plane perpendicular to the light beam, $\Gamma = 2\pi\Delta/\lambda = 2\pi d(\Delta n)/\lambda$ the optical phase difference, Δ the optical retardation, λ the light wavelength, d the sample thickness, and Δn the optical birefringence.

After recording and filtering of the images, the azimuthal dependences of the intensity I are fitted by the sine function for each pixel:

$$I = C_1 + C_2 \sin\left[2\left(a - C_3\right)\right], \tag{1.17}$$

where C_1, C_2 and C_3 are fitting coefficients.

By comparing formulae (1.16) and (1.17), one can write out the fitting coefficients as follows:

$$C_1 = \frac{I_0}{2},\ C_2 = \frac{I_0}{2}\sin\left(\Gamma\right),\ C_3 = \zeta. \tag{1.18}$$

The Γ value is determined only by the fitting coefficients C_1 and C_2:

$$\sin\Gamma = \frac{C_2}{C_1}. \tag{1.19}$$

In its turn, the angular orientation of the intensity minimum is given by the orientation ζ of the principal axis of the optical indicatrix, which is equal to the coefficient C_3.

After fitting the light intensity for each pixel of the sample image behind the analyzer as a function of polarization azimuth, one can construct 2D maps of the optical anisotropy parameters for the sample. These parameters comprise the optical retardation Δ and the orientation angle ζ of the principal axis of the optical indicatrix.

As a demonstration of accuracy of our experiments, we present in Fig. 1-2 the spatial distributions of optical retardation and the orientation of the principal axis of the optical indicatrix for “empty” polarimeter with no sample inserted.

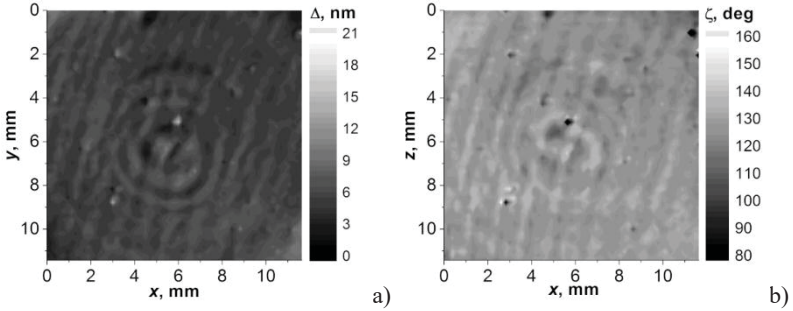

Fig. 1-2. Images of distributions of optical retardation (a) and orientation of major principal axis of the optical indicatrix (b), as measured for the polarimeter with no sample inserted into optical scheme.
Adapted with permission from Vasylkiv, Y., Kvasnyuk, O., Krupych, O., Mys, O., Maksymuk, O., & Vlokh, R. (2009). Reconstruction of 3D stress fields basing on piezooptic experiment. Ukr. J. Phys. Opt., 10(1), 22–37. © O. G. Vlokh Institute of Physical Optics.

Of course, the optical retardation for the air and isotropic optical elements such as lenses and polarizers should be equal to zero. However, some false "background" retardation still exists. It is due to experimental errors caused mainly by multiple light reflections in the optical elements and small misalignments of the optical axes of those elements, which are being rotated during the experiment. Following from the results presented in Fig. 1-2, one can determine the apparatus-driven errors in evaluating the optical retardation and the orientation of optical indicatrix. These are equal to ±3.5 nm and ±5 deg, respectively.

A loading device used in this experiment (see Fig. 1-3 and Ref. [50]) has been selected basing on the analysis [14, 15], which provides the most uniform distribution of stresses within the sample.

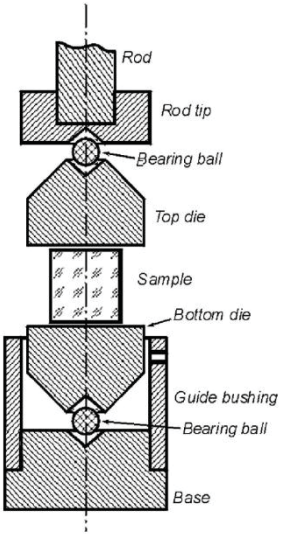

Fig. 1-3. Scheme of the loading device.
Note: We use a cardboard between the sample and the top (bottom) die as and intermediate layer, in order to eliminate inhomogeneity of the corresponding surfaces and decrease the friction force between these surfaces.
Adapted with permission from Vasylkiv, Y., Kvasnyuk, O., Krupych, O., Mys, O., Maksymuk, O., & Vlokh, R. (2009). Reconstruction of 3D stress fields basing on piezooptic experiment. Ukr. J. Phys. Opt., 10(1), 22–37. © O. G. Vlokh Institute of Physical Optics.

The sample in the shape of cube with the dimensions $11.45(x)\times11.3(y)\times11.45(z)$ mm^3 has been prepared from a BK7 glass (according to Schott classification). Its refractive index at the light wavelength $\lambda = 632.8$ nm is equal to $n = 1.51466$, while the photoelastic coefficient $K = (n_0)^3(\pi_{11} - \pi_{12})/2$ at the wavelength $\lambda = 550$ nm is equal to $K = 2.76$ m^2/N [51]. The dispersion of the piezooptic coefficients in a narrow spectral region 550–632.8 nm has been neglected.

The distributions of the optical retardation and the orientation of principal axis of the optical indicatrix for the glass sample with no mechanical stress applied are presented in Fig. 1-4. It follows from these results that the residual optical birefringence Δn is smaller than 6×10^{-7}. Moreover, a comparison of the maps presented in Fig. 1-3 and Fig. 1-4 testifies that the major part of this birefringence is false, being caused by specific features of both the experimental setup and the method used. In other terms, we deal simply with an apparatus error. In fact, the

birefringence as small as $\Delta n \approx 6\times10^{-7}$ merely represents the accuracy for the birefringence achieved in the experiment.

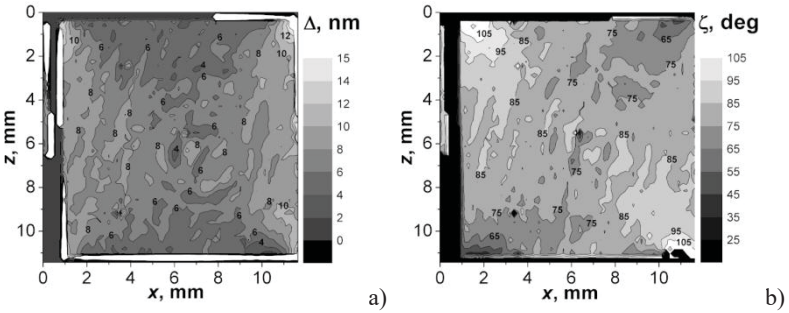

Fig. 1-4. Images of distributions of optical retardation (a) and orientation of principal axis of the optical indicatrix (b) for a glass sample with no mechanical stress applied.

Adapted with permission from Vasylkiv, Y., Kvasnyuk, O., Krupych, O., Mys, O., Maksymuk, O., & Vlokh, R. (2009). Reconstruction of 3D stress fields basing on piezooptic experiment. Ukr. J. Phys. Opt., 10(1), 22–37. © O. G. Vlokh Institute of Physical Optics.

Fig. 1-5 displays the distributions of the optical retardation and the orientation of principal axis of the optical indicatrix for the glass sample under conditions when the mechanical stress $\sigma_3 = -1.93\times10^6$ N/m^2 is applied. It is important that repeated experiments accompanied with realignments of sample have not led to notable difference in the distributions of optical parameters. However, the maximum of the optical retardation has become located at different points. Namely, it has been close to the lateral, upper or bottom edges of the sample in different experiments. These shifts are probably caused by some misalignments of stress-application scheme, which lead to appearance of additional components of the stress tensor.

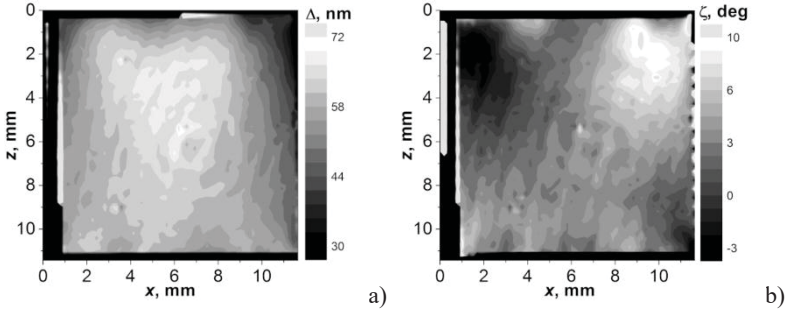

Fig. 1-5. Images of distributions of optical retardation (a) and orientation of principal axis of the optical indicatrix (b) for a glass sample under the mechanical stress $\sigma_3 = -1.93\times10^6$ N/m^2 applied.

Adapted with permission from Vasylkiv, Y., Kvasnyuk, O., Krupych, O., Mys, O., Maksymuk, O., & Vlokh, R. (2009). Reconstruction of 3D stress fields basing on piezooptic experiment. Ukr. J. Phys. Opt., 10(1), 22–37. © O. G. Vlokh Institute of Physical Optics.

The optical phase differences within the cross-section of the sample and the cross-section of laser beam (with the diameter 1.5 mm) propagating through the center of the cross-section are compared in Table 1-1. The relative error for the optical retardation inside the whole cross-section of the sample reaches the magnitude of 14%, while the relative error for the circular cross-section of laser beam is about 4%. In other words, the error for the experiments with non-expanded laser beam can be reduced at least by 3.5 times under condition that the mechanical stress in the spatial region where the laser beam propagates is known in advance.

Table 1-1. Optical retardation for the whole cross-section of sample and the cross-section of laser beam propagating through the sample center

Number of the experiment	Retardation for the whole cross-section of sample			Retardation for the cross-section of laser beam		
	Mean value, nm	Absolute error, nm	Relative error, %	Mean value, nm	Absolute error, nm	Relative error, %
1	58.11	8.53	14.66	66.06	1.71	2.59
2	58.50	9.12	15.58	67.99	3.18	4.67
3	55.72	7.73	13.87	63.09	2.85	4.50
4	55.74	9.51	17.07	61.33	2.53	4.13
5	55.72	5.73	10.30	60.33	2.23	3.71
6	56.58	6.84	12.09	62.44	2.78	4.46
Mean value	56.72	7.91	13.94	63.54	2.55	4.01

1.3.2. Reconstruction of mechanical stresses. Mechanical model and numerical simulations

Let us assume that the experimental conditions provide a possibility for uniform application of mechanical load along the z direction of sample and that the sample is initially optically homogeneous and isotropic. Let the optical radiation propagate along the y direction. Then the inhomogeneity of mechanical stresses inside the sample can appear only due to a friction force between upper and lower sample surfaces and the intermediate cardboard layers. The maximal friction forces $dF_{\max}$ are proportional to the loading stress σ_3,

$$dF_{\max} = k\sigma_3 dS, \tag{1.20}$$

where $k = 0.22$ is the friction coefficient for the case of friction between the glass and the paper (see Ref. [52]), and dS denotes a small element of square of the sample surface.

The friction forces mentioned are directed from the lateral faces of sample to the central z axis (see Fig. 1-6), thus leading to appearance of barrel-shaped distortion of the sample under the compressive stress σ_3.

In the first approximation, one can take into account the following boundary conditions for this type of inhomogeneously stressed sample:

(1) $\sigma_1 = \sigma_2 = 0$ on the four lateral faces of sample;

(2) $\sigma_1^{\max} = \sigma_2^{\max} = k\sigma_3$ on the upper and lower faces;

(3) $\sigma_3 = -1.93\times10^6$ N/m^2 on all the faces in our experiment and simulations.

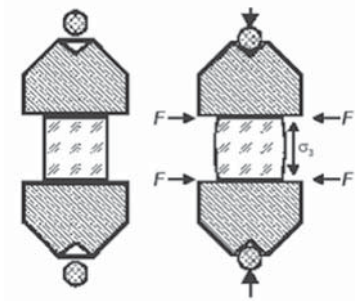

Fig. 1-6. Barrel-shaped distortion of sample under a compressive stress σ_3.
Adapted with permission from Vasylkiv, Y., Kvasnyuk, O., Krupych, O., Mys, O., Maksymuk, O., & Vlokh, R. (2009). Reconstruction of 3D stress fields basing on piezooptic experiment. Ukr. J. Phys. Opt., 10(1), 22–37. © O. G. Vlokh Institute of Physical Optics.

Let us use the approach presented in the work [53] for the superposition of three solutions, each of which being a solution of the problem for the elastic layer. The general solution of the Lame's equation in the absence of volume forces can be written as a sum of three solutions for the displacement vectors u, v and w along the x, y and z directions, respectively.

Simulations of the distribution of optical retardation have been performed on the basis of integral Jones matrix approach. The sample under analysis has been divided into 1000 (10×10×10) elementary (optically uniform) cells. The resulting Jones matrices $\mathbf{J}^{ij}$ for each of 100 elementary beams (i, j = 1...10) have been obtained by multiplying the Jones matrices of 10 elementary cells, through which each elementary beam has passed along the y direction:

$$\mathbf{J}^{ij} = \prod_{n=1}^{10} \mathbf{J}_n^{ij}. \tag{1.21}$$

Here $\mathbf{J}_n^{ij}$ is the Jones matrix of the elementary cell:

$$\mathbf{J}_n^{ij} = \begin{vmatrix} e^{i\Gamma_n^{ij}/2}\cos^2\zeta_n^{ij} + e^{-i\Gamma_n^{ij}/2}\sin^2\zeta_n^{ij} & i\sin(\Gamma_n^{ij}/2)\sin 2\zeta_n^{ij} \\ i\sin(\Gamma_n^{ij}/2)\sin 2\zeta_n^{ij} & e^{i\Gamma_n^{ij}/2}\sin^2\zeta_n^{ij} + e^{-i\Gamma_n^{ij}/2}\cos^2\zeta_n^{ij} \end{vmatrix}. \tag{1.22}$$

Γ_n^{ij} represents the optical phase difference of the elementary cell,

$$\Gamma_n^{ij} = \frac{\pi d_n^{ij}}{\lambda} n_0^3 (\pi_{11} - \pi_{12}) \sqrt{\left[(\sigma_1)_n^{ij} - (\sigma_3)_n^{ij}\right]^2 + \left[2(\sigma_5)_n^{ij}\right]^2}, \tag{1.23}$$

and ζ_n^{ij} denotes the angle of orientation of quasi-principal axes of the optical indicatrix,

$$\zeta_n^{ij} = \frac{1}{2}\operatorname{atan}\frac{2(\sigma_5)_n^{ij}}{(\sigma_1)_n^{ij} - (\sigma_3)_n^{ij}}. \tag{1.24}$$

Because the Jones vector of the elementary beam at the sample output reads as

$$\mathbf{E}_{out}^{ij} = \begin{pmatrix} E_1^{ij} \\ E_3^{ij} \end{pmatrix} = \mathbf{J}^{ij}\mathbf{E}_{circ},\ \mathbf{E}_{circ} = \frac{1}{\sqrt{2}}\begin{pmatrix} 1 \\ i \end{pmatrix}, \tag{1.25}$$

the resulting phase difference for each elementary beam is determined by the ratio

$$\Gamma^{ij} = \frac{\pi}{2} + \arg\left(\frac{E_1^{ij}}{E_3^{ij}}\right) = \frac{\pi}{2} - \arg\left(\frac{E_3^{ij}}{E_1^{ij}}\right). \tag{1.26}$$

Then the optical retardation $\Delta = \Gamma\lambda/2\pi$ can be calculated.

To match the calculated distribution of the optical retardation with the experimental one, it has been taken into account that the pressure on the upper face of sample has the form of half-period of the sinusoid shifted to the left, which corresponds to non-ideal setting of the sample:

$$\sigma_3\big|_{z=c} = -N_1\left[-0,05\sin\pi\frac{x}{a}\sin\pi\frac{y}{b} + 0,3\frac{\pi^2}{48}\left(1-\frac{x}{a}\right)\left(1-\frac{y}{b}\right)\right]. \tag{1.27}$$

In order to account for a barrel-shaped distortion, the stress on the side faces satisfies the boundary conditions

$$\begin{aligned} &\sigma_1\big|_{x=0,\,a} = 0, \quad \sigma_2\big|_{x=0,\,a} = -0.2\times\sigma_3\sin\pi\frac{z}{c}\sin\pi\frac{y}{b}, \\ &\sigma_2\big|_{y=0,\,b} = 0, \quad \sigma_1\big|_{y=0,\,b} = -0.2\times\sigma_3\sin\pi\frac{x}{a}\sin\pi\frac{z}{c}. \end{aligned} \tag{1.28}$$

Fig. 1-7 shows the simulation data for the piezo-induced optical retardation and orientation of optical indicatrix which takes into account a barrel-like deformation of the sample under pressure and inaccuracy of its setting with respect to the axis of pressure application.

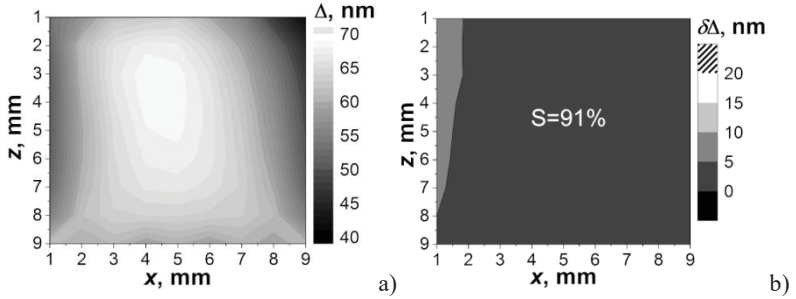

Fig. 1-7. Maps of simulated optical retardation (a) and difference of experimental (see Fig. 1-5a) and simulated optical retardations (b).
Adapted with permission from Vasylkiv, Y., Kvasnyuk, O., Krupych, O., Mys, O., Maksymuk, O., & Vlokh, R. (2009). Reconstruction of 3D stress fields basing on piezooptic experiment. Ukr. J. Phys. Opt., 10(1), 22–37. © O. G. Vlokh Institute of Physical Optics.

Fig. 1-7b indicates that the major part (91%) of the cross-section is correlated with the experimental results. Nonetheless, its small part (9%) still disagrees with the experimental data. It is probably caused by some warp of the top die in the upper left side of the sample, along with some sliding between the sample and the die. This can be accounted for while reducing the friction coefficient down to the value $k = 0.1$ (Fig. 1-8). In this case the experimental and simulation results have the similarity 98%.

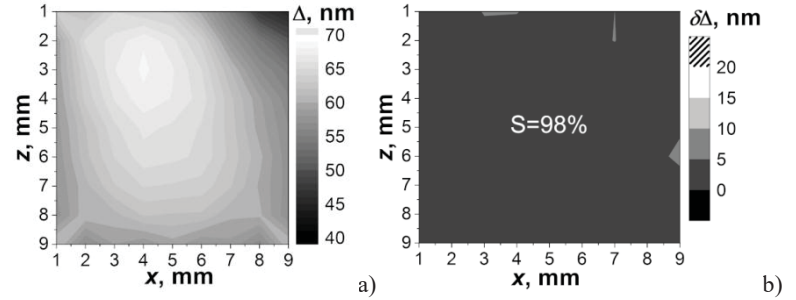

Fig. 1-8. Maps of simulated optical retardation (a) and difference of experimental (see Fig. 1-5a) and simulated optical retardations (b), as obtained after sliding between the sample and the die is taken into account.
Adapted with permission from Vasylkiv, Y., Kvasnyuk, O., Krupych, O., Mys, O., Maksymuk, O., & Vlokh, R. (2009). Reconstruction of 3D stress fields basing on piezooptic experiment. Ukr. J. Phys. Opt., 10(1), 22–37. © O. G. Vlokh Institute of Physical Optics.

By analyzing the simulated mechanical-stress distribution, the following conclusions can be made:

- loading of sample in a common manner gives rise not only to the component σ_3 of the mechanical stress tensor, but also to all the other components of this tensor;
- the distribution of mechanical stress tensor components inside the sample is inhomogeneous;
- the σ_3 component in the vicinity of geometrical center of the sample is one order of magnitude larger than the σ_1 component and two orders of magnitude larger than the other stress components;
- the σ_3 component in the center of the sample reaches a value 26% higher than the stress actually loaded, while the deviation of this component within the sample volume amounts to 32%;
- the deviations of the other stress components exceed hundred per cents and, moreover, the signs of the shift stress components are different in different parts of the sample.

Let us assume that a non-expanded laser beam with the cross-section area ~ 2 mm^2 propagates through the sample center parallel to the y axis. The optical phase difference for this light propagation direction is equal to 65.7 deg. On the other hand, the optical phase difference for the case of homogeneously distributed mechanical stress ($\sigma_3 = -1.93\times10^6$ N/m^2) can be calculated with the formula

$$\Gamma = 2\pi d n_0^3 \left(\pi_{11} - \pi_{12}\right)\sigma_3 / \lambda. \tag{1.29}$$

It is equal to 60.1 deg. Hence, the actual value of the optical phase difference is smaller by 8.5% than the measured one. This means that in any practical piezooptic experiment, which does not take the distribution of mechanical stresses into account, the piezooptic coefficients determined experimentally differ from their actual values at least by 8.5%.

Of course, only complete reconstruction of the stress field inside a sample and a consistent consideration of the stress components at each sample point would allow one to obtain a correct value of the piezooptic coefficient. In our case the latter is equal to $(\pi_{11} - \pi_{12}) = 1.59\times10^{-12}$ m^2/N.

Summing up the results, we conclude that the greatest contribution into inhomogeneous distribution of mechanical stress originates from the imperfection of pressing surface of a poisson, the sample non-parallelism, and the friction between the poissons and the sample faces. At the same

time, the enormous errors appearing in typical piezooptic experiments are mainly caused by the friction forces that exist inside an intermediate contact layer between the upper and lower sample surfaces and the corresponding substrates, as well as by the misalignments of mechanical loading. The friction force leads to a barrel-shaped distortion of samples and the inevitable appearance of all components of the mechanical stress tensor, in spite of the fact that a uniaxial pressure has been initially applied.

Unlike the simplest experiment with an isotropic medium discussed above, the distribution of mechanical stresses in the case of anisotropic media will be even more complicated, and the requirements for the loading device and the sample more strict. A possible way out of this situation is to use the technique described above to investigate the piezooptic effect in crystals. It allows for determining the degree of inhomogeneity of the spatial field of mechanical stresses inside the sample and increasing the accuracy of the piezooptic coefficients.

It has been shown above that, instead of a uniform stress state which has traditionally been a priori supposed, uniaxial compressing of a parallelepiped-shaped sample results in a non-uniform distribution of mechanical stresses, with uncontrolled inhomogeneity. Therefore, it is almost impossible to obtain a uniform stress distribution when measuring piezooptic coefficients. Then it would be advisable to use such sample-loading methods which lead to a non-uniform, though known beforehand mechanical stress distribution.

1.4. Optimal geometric proportions of samples for piezooptic experiments

As shown above, the mechanical stress tensor components are non-uniformly distributed in any parallelepiped-shaped sample, even if a uniaxial compressing load is applied to this sample.

The reasons why a complicated spatial distribution of the stress components appears lie in misalignments of sample loading and a barrel-shaped distortion of rectangular samples. As a result, the error in determination of the mechanical stress tensor component σ_3 is about 30%. This error can be reduced down to ~ 14% by accurately aligning the sample in a pressure setup and carefully complying the condition of parallelism of the opposite sample surfaces. However, the barrel-shaped distortion, which appears due to the friction forces arising between the upper and lower sample surfaces and the appropriate substrates, cannot be eliminated completely.

To increase the accuracy of piezooptic experiments, we have suggested a number of methods for sample loading, which produce spatially inhomogeneous distributions of the stress components, of which coordinate dependences are known in advance. A diametrical compression of a disk, mechanical torsion of a rod and four-point bending of a bar are among these methods. They have turned out to be precise enough when determining the piezooptic coefficients. Moreover, some of them (e.g., the method of four-point bending) enables one to determine all of the piezooptic tensor components.

Nonetheless, these methods reveal a substantial practical disadvantage: they require a lot of samples with predetermined sizes and different crystallographic orientations. This necessitates growing of many (large enough) crystalline boules and utilizing complex procedures for manufacturing and precise processing the samples.

Returning to uniaxial compressing of a parallelepiped-shaped sample, one may ask the following questions:

- Could the loading-related errors of piezooptic experiments be minimized by optimizing a geometrical shape of a sample?
- Which are those optimal geometrical parameters of the sample and, first of all, the ratio of its width to its length, which make the errors caused by mechanical stress inhomogeneity inside the sample small or, at least, smaller than the errors typical for the polarimetric or interferometric experiments themselves?

One can try to solve this problem by means of simulations of the mechanical stress distributions in isotropic glass samples [54].

Let us consider a parallelepiped-shaped isotropic BK7-glass sample with a square cross-section ($a = b$) and different ratios of its width to height ($a : c$ = 1:1, 1:3 and 1:5). Let the compression load be applied along the z axis. Assume that the loading force is uniformly distributed over the upper and lower surfaces and the substrates are covered by a layer of paper. Then the coefficient of friction between the glass and the paper is equal to $k = 0.22$ [52]. Obviously, the friction forces appearing between the upper and lower sample faces and the substrates covered by the paper should lead to a barrel-shaped distortion of the sample.

The algorithm for solving the elastic equilibrium equation is similar to that used above. It has been described in detail in Refs. [50, 54]. Its application results in a spatial distribution of mechanical stress tensor components in the sample. Having obtained the distributions for all of the stress components, we have simulated the optical phase difference for the

case of light propagating along the y axis. The corresponding algorithm is based on dividing the sample into cells and using the Jones matrices (see the relations (1.21)–(1.26)). Within this algorithm, the sample has been divided into 10 layers, which are taken as being mechanically and optically homogeneous along the light propagation direction. Each of the layers has been divided into 10×10 cells.

Figs. 1.9–1.14 display the main results of our simulations performed for the parallelepiped-shaped isotropic glass samples with the square cross-sections ($a = b$) and different width-to-height ratios ($a : c$ = 1:1, 1:3 and 1:5). The stress tensor components have been normalized at the nominal compressive stress $\sigma_3 = P/a^2$, with P being the loading force.

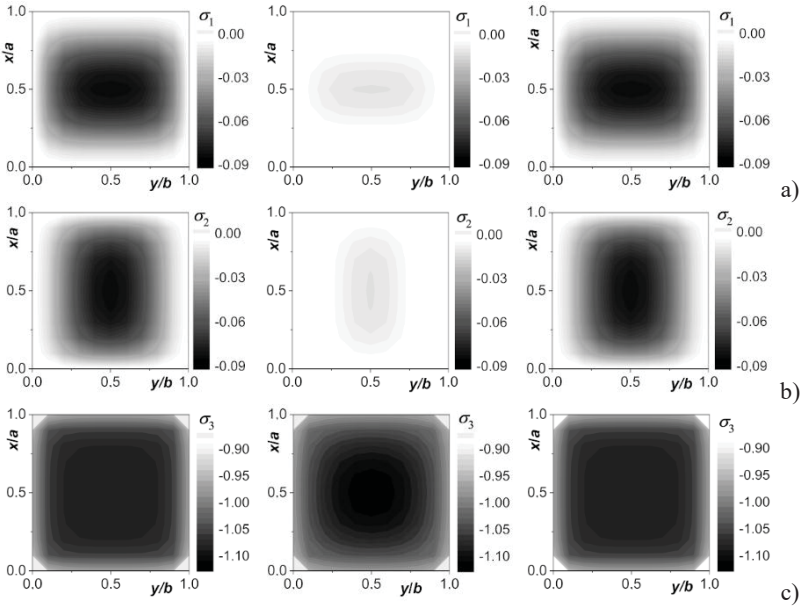

Fig. 1-9. Distributions of mechanical stress tensor components σ_1 (a), σ_2 (b) and σ_3 (c) for a parallelepiped-shaped isotropic glass sample with the dimensions $a = b$ and $a : c$ = 1:1. Left, central and right columns correspond to the cross-sections $z = 0.2c$, $0.5c$ and $0.8c$, respectively.
Adapted with permission from Kvasnyuk, O., Vasylkiv, Y., Krupych, O., & Vlokh, R. (2014). Preferable geometrical parameters of samples for piezooptic experiments. Ukr. J. Phys. Opt., 15(4), 195–206. © O. G. Vlokh Institute of Physical Optics.

For the sample of cubic shape ($a : c$ = 1:1), the stress components σ_1 and σ_2 change from zero on the side surfaces to a minimum in the centers of all

cross-sections (Figs. 1.9a–1.9b). Negative values of these components point to the compressive normal stresses that vary from –0.013 in the central plane (at $z = 0.5c$) to –0.085 at $z = 0.2c$ and $z = 0.8c$. The component σ_3 reaches its minimum, –1.12, in the center of the sample and increases to –1.088 at $z = 0.2c$ and $z = 0.8c$ (Fig. 1-9c). This means that the actual value of the component $|\sigma_3|$ in the center of the sample is 12% higher than that expected within the idealized model of uniform stress state.

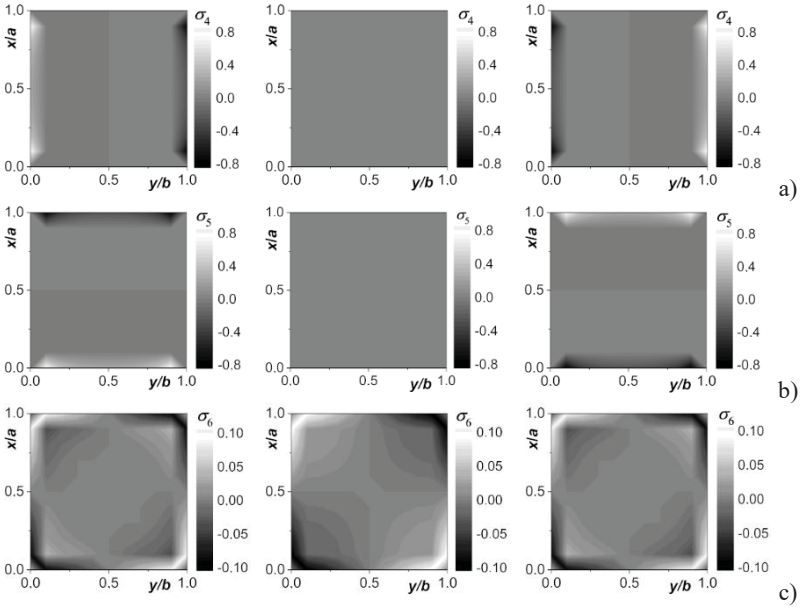

Fig. 1-10. Distributions of mechanical stress tensor components σ_4 (a), σ_5 (b) and σ_6 (c) for a parallelepiped-shaped isotropic glass sample with the dimensions $a = b$ and $a : c = 1:1$. Left, central and right columns correspond to the cross-sections $z = 0.2c$, $0.5c$ and $0.8c$, respectively.
Adapted with permission from Kvasnyuk, O., Vasylkiv, Y., Krupych, O., & Vlokh, R. (2014). Preferable geometrical parameters of samples for piezooptic experiments. Ukr. J. Phys. Opt., 15(4), 195–206. © O. G. Vlokh Institute of Physical Optics.

The components $|\sigma_4|$ and $|\sigma_5|$ exceed 0.8 in thin layers close to the side faces in the cross-sections $z = 0.2c$ and $z = 0.8c$ (see Figs. 1.10a–1.10b). They are equal to zero in the central plane of the sample (at $z = 0.5c$). On the other hand, the component $|\sigma_6|$, which must have been absent in the ideal model, reaches 0.1 even in the "middle" cross-section $z = 0.5c$,

although it remains equal to zero just at the center of all sections (Fig. 1-10c).

Given the results obtained, we should note that the appearance of additional nonzero stress components can lead to incorrect determination of the actual stress and, as a result, to an error for the piezooptic coefficients. In our case, the approximate estimate of the error typical for the σ_3 component is 12% for the sample with $a : c = 1:1$.

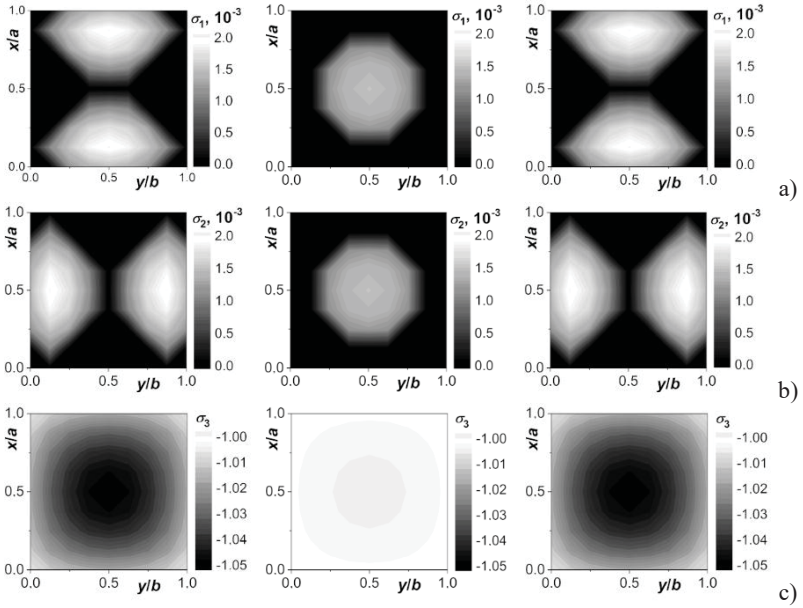

Fig. 1-11. Distributions of mechanical stress tensor components σ_1 (a), σ_2 (b) and σ_3 (c) for parallelepiped-shaped isotropic glass sample with $a = b$ and $a : c = 1:3$. Left, central and right columns correspond to the cross-sections $z = 0.2c$, $0.5c$ and $0.8c$, respectively.

Adapted with permission from Kvasnyuk, O., Vasylkiv, Y., Krupych, O., & Vlokh, R. (2014). Preferable geometrical parameters of samples for piezooptic experiments. Ukr. J. Phys. Opt., 15(4), 195–206. © O. G. Vlokh Institute of Physical Optics.

For the sample with $a : c = 1:3$, the mechanical stress tensor components σ_1 and σ_2 (Figs. 1.11a–1.11b) achieve 0.0015 in the "middle" cross-section ($z = 0.5c$) and 0.002 in the cross-sections given by $z = 0.2c$ and $z = 0.8c$. In its turn, the component σ_3 varies from –1.005 to –1 at $z = 0.5c$ and from –1.05 to –1 when we approach the upper ($z = 0.2c$) and lower ($z = 0.8c$) faces of the sample (Fig. 1-11c).

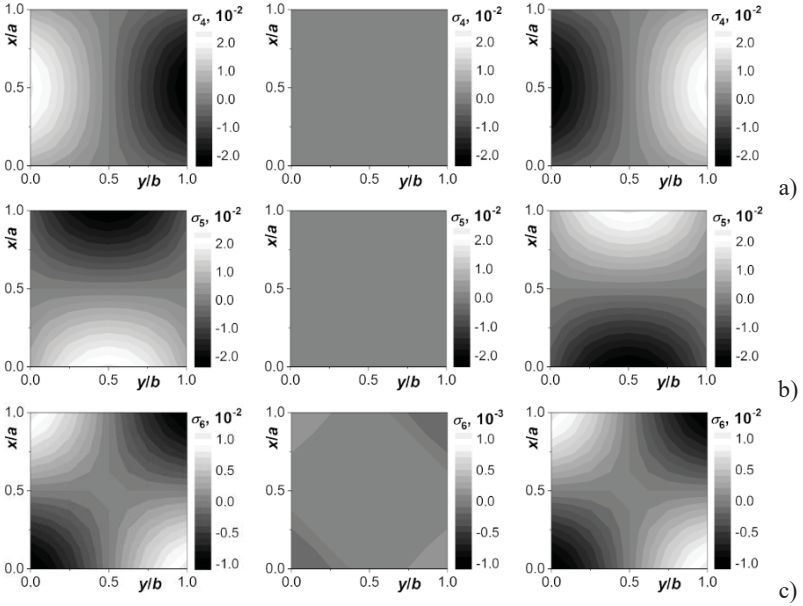

Fig. 1-12. Distributions of mechanical stress tensor components σ_4 (a), σ_5 (b) and σ_6 (c) for parallelepiped-shaped isotropic glass sample with $a = b$ and $a : c = 1{:}3$. Left, central and right columns correspond to the cross-sections $z = 0.2c$, $0.5c$ and $0.8c$, respectively.

Adapted with permission from Kvasnyuk, O., Vasylkiv, Y., Krupych, O., & Vlokh, R. (2014). Preferable geometrical parameters of samples for piezooptic experiments. Ukr. J. Phys. Opt., 15(4), 195–206. © O. G. Vlokh Institute of Physical Optics.

The components $|\sigma_4|$ and $|\sigma_5|$ are equal to zero in the central cross-section ($z = 0.5c$), whereas in the cross-sections $z = 0.2c$ and $z = 0.8c$ they increase to ~ 0.023 when y and x approach b and a, respectively (Figs. 1-12a–1-12b). The component $|\sigma_6|$ remains the smallest and does not exceed 0.01 (Fig. 1-12c).

Hence, the component σ_3 is at least two orders of magnitude higher than the other stress tensor components. Therefore it contributes dominantly into the effective stress. Since the maximal value of the actual stress $\sigma_3 = -1.05$ deviates from the idealized value $\sigma_3 = -1$, the maximal error for the component σ_3 can be estimated as 5% for the sample with $a : c = 1{:}3$. It should be noted that this error is reduced by an order of magnitude in the central part of the sample, where it is only 0.5%. The latter value does not exceed the error inherent in the polarization or interference optical methods.

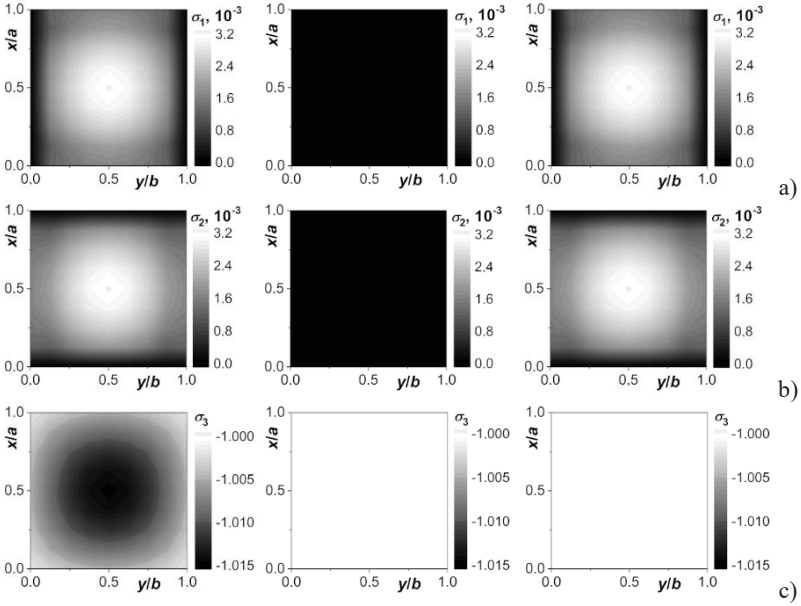

Fig. 1-13. Distributions of mechanical stress tensor components σ_1 (a), σ_2 (b) and σ_3 (c) for parallelepiped-shaped isotropic glass sample with $a = b$ and $a : c = 1{:}5$. Left, central and right columns correspond to the cross-sections $z = 0.2c$, $0.5c$ and $0.8c$, respectively.

Adapted with permission from Kvasnyuk, O., Vasylkiv, Y., Krupych, O., & Vlokh, R. (2014). Preferable geometrical parameters of samples for piezooptic experiments. Ukr. J. Phys. Opt., 15(4), 195–206. © O. G. Vlokh Institute of Physical Optics.

For the sample with $a : c = 1{:}5$, the stress components σ_1 and σ_2 equal to zero in the "middle" cross-section ($z = 0.5c$) and reach the value 0.003 at $z = 0.2c$ and $z = 0.8c$ (see Figs. 1.13a–1.13b). The component σ_3 varies from –1.0001 to –1 at $z = 0.5c$ and from –1.015 to –1 at $z = 0.2c$ and $z = 0.8c$ (Fig. 1-13c).

The components $|\sigma_4|$ and $|\sigma_5|$ amount to 0.008 at the side sample faces in the sections $z = 0.2c$ and $z = 0.8c$ and remain equal to zero at $z = 0.5c$ (Figs. 1-14a–1-14b). However, the component $|\sigma_6|$ reaches its maximum (0.006) near the upper and lower surfaces of the sample (see Fig. 1-14c).

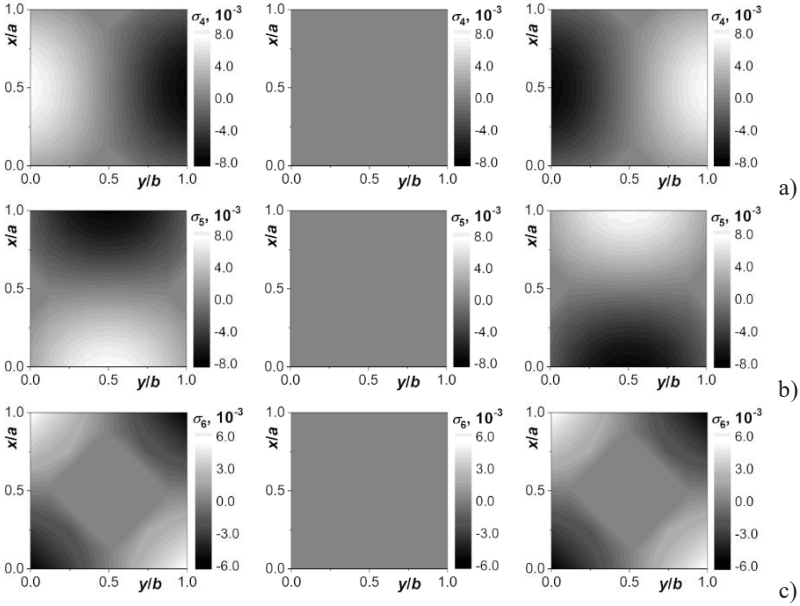

Fig. 1-14. Distributions of mechanical stress tensor components σ_4 (a), σ_5 (b) and σ_6 (c) for parallelepiped-shaped isotropic glass sample with $a = b$ and $a : c = 1{:}5$. Left, central and right columns correspond to the cross-sections $z = 0.2c$, $0.5c$ and $0.8c$, respectively.

Adapted with permission from Kvasnyuk, O., Vasylkiv, Y., Krupych, O., & Vlokh, R. (2014). Preferable geometrical parameters of samples for piezooptic experiments. Ukr. J. Phys. Opt., 15(4), 195–206. © O. G. Vlokh Institute of Physical Optics.

Thus, the maximum error of determination of the component σ_3 does not exceed 1.5% for the sample with $a : c = 1{:}5$. It is governed by the component σ_3 near the top and bottom surfaces of the sample. Since this error is an order of magnitude smaller in the central part of the sample, it can be neglected when determining the piezooptic coefficients.

As the last stage of our analysis, we have simulated the changes occurring in the optical phase difference, which are associated with inhomogeneous stress distribution. The optical phase difference is determined as $\delta\Gamma^{ij} = \Gamma^{ij}_{\mathrm{hom}} - \Gamma^{ij}_{\mathrm{inh}}$, where $\Gamma^{ij}_{\mathrm{hom}}$ and $\Gamma^{ij}_{\mathrm{inh}}$ are the total optical phase differences determined from the ratio (1.26) respectively for the cases of homogeneous (a single nonzero stress component is nonzero, $\sigma_3 = 2.4\times10^6$ N/m^2) and inhomogeneous (all the stress components differ from zero) stress distributions.

For all values $a : c$ in case of homogeneous distribution of the stresses, the optical phase difference is the same and equals to $\Gamma_{\text{hom}}^{ij} = 39$ deg at the sample thickness 10^{-2} m. Fig. 1-15 shows the phase difference distributions obtained for the samples with $a : c = 1{:}1$, 1:3 and 1:5.

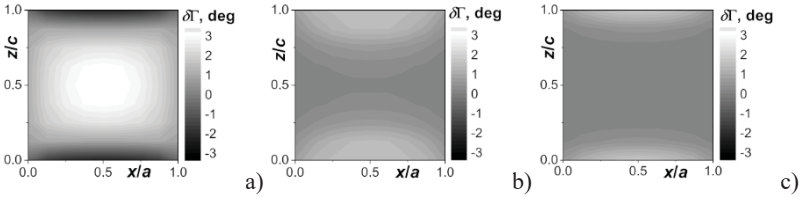

Fig. 1-15. Distributions of optical phase difference changes, as simulated for the samples with $a : c$ equal to 1:1 (a), 1:3 (b) and 1:5 (c).
Adapted with permission from Kvasnyuk, O., Vasylkiv, Y., Krupych, O., & Vlokh, R. (2014). Preferable geometrical parameters of samples for piezooptic experiments. Ukr. J. Phys. Opt., 15(4), 195–206. © O. G. Vlokh Institute of Physical Optics.

It is worth noting that, even in case of the most inhomogeneous distribution of mechanical stresses ($a : c = 1{:}1$), the rotation angle of the optical indicatrix within the homogeneous cells located near the upper and lower surfaces does not exceed 2 deg and remains negligibly small in the central part of the sample. When the beam propagates through the center of the cross-section of sample, the relative errors for the optical phase difference are equal to 8.4, 0.4 and 0.00025% for the cases of $a : c = 1{:}1$, 1:3 and 1:5, respectively. In the case of $a : c = 1{:}3$, the maximal error for the optical phase difference does not exceed 3.8% even if one takes the entire cross-section of the sample into account. Let us deal with the sample size $3{\times}3{\times}9$ mm^3 and the optical beam diameter ~ 2 mm. Then the error can be further reduced at least down to ≤ 0.7%. Notice that this result agrees well with the experimental results presented in the work [55].

Hence, the error of experimental determination of the piezooptic coefficients, which is caused by the friction between the surfaces of the sample and the substrates, can be reduced by selecting the optimal geometric parameters of samples. At the same time, the optimal ratio of width a to height c for the isotropic samples with the square cross-section ($a = b$) amounts to 1:3. Then we arrive at a reasonable compromise between the accuracy of measurements and the practical requirements for the sample dimensions.

SECTION 2

POLARIMETRIC METHOD FOR DETERMINING PIEZOOPTIC COEFFICIENTS USING CRYSTALLINE DISKS COMPRESSED ALONG THEIR DIAMETER

As already noted, uniaxial compression of a parallelepiped sample results in a non-uniform distribution of mechanical stresses in this sample, so that the stress heterogeneity remains uncontrolled. A possible alternative in the piezooptic studies can be such loading methods that lead to non-uniform distributions of mechanical stresses in a sample, which are known in advance. In particular, this can be torsion of a rod, bending of a bar or a uniaxial compression of a disk along its diameter [55]. In this section, we analyze the abilities of the latter method used for measuring the piezooptic coefficients in crystals of different symmetry groups [56, 57].

2.1. Distribution of mechanical stresses in a compressed disk

Let the origin of Cartesian laboratory coordinate system be in the centre of a disk, the z axis be perpendicular to the disk plane, and the y axis parallel to the direction of loading force P (Fig. 2-1). Then the loading force has the only component $P = P_y = P_2$. Since the loading of a crystalline disk along its diameter creates a 2D stressed state ("plane" stress), there are only three nonzero components of mechanical stress tensor in the disk: $\sigma_1 = \sigma_x$, $\sigma_2 = \sigma_y$ and $\sigma_6 = \tau_{xy}$. They depend on the coordinates x and y as follows [55]:

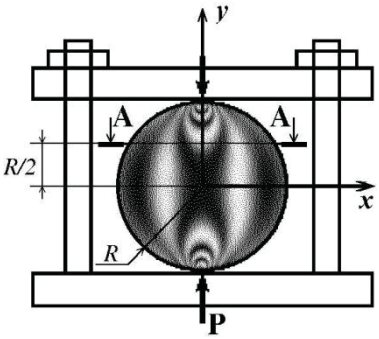

Fig. 2-1. Diagram of disk loading and selection of laboratory coordinate system [55].

$$\sigma_1(x,y) = -\frac{2P_2}{\pi d}\left\{\frac{(R-y)x^2}{\left[x^2+(R-y)^2\right]^2} + \frac{(R+y)x^2}{\left[x^2+(R+y)^2\right]^2} - \frac{1}{2R}\right\}, \tag{2.1}$$

$$\sigma_2(x,y) = -\frac{2P_2}{\pi d}\left\{\frac{(R-y)^3}{\left[x^2+(R-y)^2\right]^2} + \frac{(R+y)^3}{\left[x^2+(R+y)^2\right]^2} - \frac{1}{2R}\right\}, \tag{2.2}$$

$$\sigma_6(x,y) = \frac{2P_2}{\pi d}\left\{\frac{(R-y)^2 x}{\left[x^2+(R-y)^2\right]^2} - \frac{(R+y)^2 x}{\left[x^2+(R+y)^2\right]^2}\right\}, \tag{2.3}$$

where d and R are the thickness and the radius of the disk, respectively.

The mechanical stresses along the horizontal diameter parallel to the x axis (i.e., under condition $y = 0$) are described by the relations

$$\begin{aligned}
\sigma_1(x,0) &= -\frac{2P_2}{\pi d}\left[\frac{2Rx^2}{\left(x^2+R^2\right)^2} - \frac{1}{2R}\right], \\
\sigma_2(x,0) &= -\frac{2P_2}{\pi d}\left[\frac{2R^3}{\left(x^2+R^2\right)^2} - \frac{1}{2R}\right], \\
\sigma_6(x,0) &= 0,
\end{aligned} \tag{2.4}$$

while along the vertical diameter ($x = 0$) we have

$$\sigma_1(0,y)=\frac{P_2}{\pi dR},$$
$$\sigma_2(0,y)=-\frac{2P_2}{\pi d}\left[\frac{2R}{R^2-y^2}-\frac{1}{2R}\right], \tag{2.5}$$
$$\sigma_6(0,y)=0.$$

As seen from the relations (2.4) and (2.5), the component σ_6 is zero at the horizontal and vertical diameters, whereas the components σ_1 and σ_2 differ from zero. This means that the principal axes of the mechanical stress tensor coincide with the axes of the laboratory system. For the other sample points which are outside the diameters specified above, all the three stress components (σ_1, σ_2 and σ_6) are nonzero.

Let us consider the distribution of mechanical stress components along the chords parallel to the axes x or y. For the case $y = R/2$ (i.e., the horizontal chord parallel to the x axis: see section A–A in Fig. 2-1), these components can be written as follows:

$$\sigma_1\left(x,\frac{R}{2}\right)=-\frac{P_2}{\pi d}\left[\frac{Rx^2}{\left(x^2+R^2/4\right)^2}+\frac{3Rx^2}{\left(x^2+9R^2/4\right)^2}-\frac{1}{R}\right], \tag{2.6}$$

$$\sigma_2\left(x,\frac{R}{2}\right)=-\frac{P_2}{\pi d}\left[\frac{R^3}{4\left(x^2+R^2/4\right)^2}+\frac{27R^3}{4\left(x^2+9R^2/4\right)^2}-\frac{1}{R}\right], \tag{2.7}$$

$$\sigma_6\left(x,\frac{R}{2}\right)=\frac{P_2}{2\pi d}\left[\frac{R^2x}{\left(x^2+R^2/4\right)^2}-\frac{9R^2x}{\left(x^2+9R^2/4\right)^2}\right]. \tag{2.8}$$

In the case $x = R/2$ (the vertical chord parallel to the y axis) we have

$$\sigma_1\left(\frac{R}{2},y\right)=-\frac{P_2}{\pi d}\left[\frac{(R-y)R^2}{2\left\{(R-y)^2+R^2/4\right\}^2}+\frac{(R+y)R^2}{2\left\{(R+y)^2+R^2/4\right\}^2}-\frac{1}{R}\right], \tag{2.9}$$

$$\sigma_2\left(\frac{R}{2},y\right)=-\frac{2P_2}{\pi d}\left[\frac{(R-y)^3}{\left\{(R-y)^2+R^2/4\right\}^2}+\frac{(R+y)^3}{\left\{(R+y)^2+R^2/4\right\}^2}-\frac{1}{2R}\right], \tag{2.10}$$

$$\sigma_6\left(\frac{R}{2},y\right)=\frac{P_2}{\pi d}\left[\frac{(R-y)^2R}{\left\{(R-y)^2+R^2/4\right\}^2}-\frac{(R+y)^2R}{\left\{(R+y)^2+R^2/4\right\}^2}\right]. \tag{2.11}$$

Unlike amorphous media, crystals manifest anisotropic physical properties. Then it would be convenient to choose a so-called "crystal physical" coordinate system. This Cartesian system is coupled with the symmetry elements, of which axes are oriented in a certain way with respect to the crystallographic coordinate system formed from the basic vectors of Bravais lattice. As a rule, the constitutive tensors (in particular, the tensor of dielectric constants, the dielectric impermeability tensor, and the piezoelectric, electro-optic and piezooptic tensors) are written just in the crystal physical coordinate system. As a consequence, it is necessary to take into account the mutual orientation of the crystal physical coordinate system of the sample and the laboratory coordinate system (see Fig. 2-1).

As a matter of fact, when the crystalline disk is of the *z*-cut (i.e., the plane of disk is parallel to the crystallographic plane (001)) and the *x* and *y* axes of the crystal physical coordinate system coincide with the *x* and *y* axes of the laboratory coordinate system, all of the above formulae remain unchanged. For the crystalline disks of *x*-cut (100) or *y*-cut (010), similar relations can be derived for the mechanical stress tensor components, which differ only by the indices.

Having the relations for the stress components σ_m and using the mathematical expression for the piezooptic effect (1.3), one can calculate the changes in the components of optical-frequency impermeability tensor and so the refractive indices. On their basis, the formulae describing the induced optical birefringence and the rotation angle of optical indicatrix can be derived. These relations will be used when calculating the piezooptic coefficients of crystals, issuing from the experimental results derived for the optical birefringence and the optical indicatrix orientation angle in diametrically compressed crystalline disks.

2.2. Determination of piezooptic coefficients of lithium niobate crystals using a diametrically compressed disk

The procedure described above has been applied for determining piezooptic coefficients for a trigonal crystal of lithium niobate ($LiNbO_3$) [58, 59]. Let us consider a disk made of $LiNbO_3$ crystal, where the coordinate system of the optical indicatrix coincides with the laboratory coordinate system. The piezooptic tensor for the point symmetry group 3*m*, which characterizes $LiNbO_3$, looks like

$$\pi_{ij} = \begin{bmatrix} \pi_{11} & \pi_{12} & \pi_{13} & \pi_{14} & 0 & 0 \\ \pi_{12} & \pi_{11} & \pi_{13} & -\pi_{14} & 0 & 0 \\ \pi_{31} & \pi_{31} & \pi_{33} & 0 & 0 & 0 \\ \pi_{41} & -\pi_{41} & 0 & \pi_{44} & 0 & 0 \\ 0 & 0 & 0 & 0 & \pi_{44} & 2\pi_{41} \\ 0 & 0 & 0 & 0 & \pi_{14} & \pi_{66} \end{bmatrix}. \tag{2.12}$$

2.2.1. *z*-cut disk

Taking into account formulae (2.1)–(2.3) for the mechanical stresses and the relationship $\pi_{11} - \pi_{12} = \pi_{66}$ peculiar for the crystals of symmetry groups $3m$, 32 and $\bar{3}m$, one can obtain the following equation for the cross-section of optical indicatrix by the plane $z = 0$ of $LiNbO_3$ [58]:

$$\begin{aligned} &\left(B_{11} + \pi_{11}\sigma_1 + \pi_{12}\sigma_2\right)x^2 + \left(B_{11} + \pi_{12}\sigma_1 + \pi_{11}\sigma_2\right)y^2 + \\ &+2\left(\pi_{11} - \pi_{12}\right)\sigma_6 xy = 1. \end{aligned} \tag{2.13}$$

Solving this equation, one can obtain the following relations for the rotation angle ζ_3 of optical indicatrix around the z axis and the optical birefringence Δn induced by mechanical compression:

$$\mathrm{tg}2\zeta_3 = \frac{2\left(\pi_{11} - \pi_{12}\right)\sigma_6}{\left(B_{11} + \pi_{11}\sigma_1 + \pi_{12}\sigma_2\right) - \left(B_{11} + \pi_{12}\sigma_1 + \pi_{11}\sigma_2\right)} = \frac{2\sigma_6}{\left(\sigma_1 - \sigma_2\right)}, \tag{2.14}$$

$$\Delta n_{12} = -\frac{1}{2}n_0^3\left(\pi_{11} - \pi_{12}\right)\sqrt{\left(\sigma_1 - \sigma_2\right)^2 + 4\sigma_6^2}. \tag{2.15}$$

Fig. 2-2 shows the coordinate distributions of the optical indicatrix rotation angle and the induced birefringence obtained from the numerical simulations based on the relations (2.14) and (2.15) for the z-cut of $LiNbO_3$ crystals. Here the mechanical stresses have been determined from the relations (2.1)–(2.3). The following numerical values are used in the calculations: the applied force $P = 100$ N, the disk thickness $d = 2$ mm, the disk radius $R = 10$ mm, $\pi_{11} - \pi_{12} = -0.47$ B, the ordinary refractive index $n_o = 2.287$, the extraordinary refractive index $n_e = 2.203$, and the wavelength $\lambda = 632.8$ nm [60, 61].

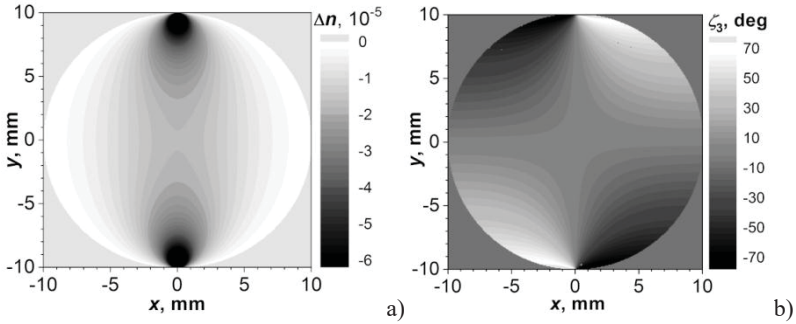

Fig. 2-2. 2D maps of induced birefringence (a) and optical indicatrix rotation angle (b), as calculated for the crystalline $LiNbO_3$ disk compressed along its *y* axis [58]. *Adapted with permission from Vasylkiv, Y., Savaryn, V., Smaga, I., Krupych, O., Skab, I., & Vlokh, R. (2011). Studies of piezooptic coefficients in $LiNbO_3$ crystals using a crystalline disk compressed along its diameter. Ukr. J. Phys. Opt., 12(4), 180–190. © O. G. Vlokh Institute of Physical Optics.*

Let us analyze the distribution of the birefringence in the *xy*-plane. Along the diameter $x = 0$ (i.e., the vertical diameter parallel to the vector of applied force), the σ_6 component is zero, whereas the σ_1 and σ_2 components are equal to

$$\sigma_1 = \frac{P}{\pi d R}, \tag{2.16}$$

$$\sigma_2 = -\frac{2P}{\pi d}\left[\frac{2R}{R^2 - y^2} - \frac{1}{2R}\right]. \tag{2.17}$$

The birefringence along this diameter is given by

$$\Delta n_{12} = -\frac{1}{2} n_0^3 \left(\pi_{11} - \pi_{12}\right)\left(\sigma_1 - \sigma_2\right) = -n_0^3 \left(\pi_{11} - \pi_{12}\right)\frac{2RP}{\pi d\left(R^2 - y^2\right)}, \tag{2.18}$$

whereas the optical indicatrix rotation remains zero, according to the relation (2.14). Note, however, that the birefringence at the origin of the coordinate system differs from zero:

$$\Delta n_{12} = -n_0^3 \left(\pi_{11} - \pi_{12}\right)\frac{2P}{\pi d R}. \tag{2.19}$$

Using the relation (2.18) and the nonlinear dependence of the birefringence Δn on the coordinate y obtained experimentally, one can determine the value $\pi_{11} - \pi_{12}$.

Under condition $y = 0$, corresponding to the horizontal diameter perpendicular to the mechanical force, the σ_6 component remains zero, whereas the σ_1 and σ_2 components are equal to

$$\sigma_1 = -\frac{2P}{\pi d}\left[\frac{2Rx^2}{\left(x^2+R^2\right)^2} - \frac{1}{2R}\right], \tag{2.20}$$

$$\sigma_2 = -\frac{2P}{\pi d}\left[\frac{2R^3}{\left(x^2+R^2\right)^2} - \frac{1}{2R}\right]. \tag{2.21}$$

In this case we have $\tan 2\zeta_3 = 0$, while the birefringence can be written as

$$\Delta n_{12} = \frac{1}{2} n_0^3 \left(\pi_{11} - \pi_{12}\right)\left(\sigma_1 - \sigma_2\right) = n_0^3 \frac{2P}{\pi d}\left(\pi_{11} - \pi_{12}\right)\frac{R\left(R^2 - x^2\right)}{\left(R^2 + x^2\right)^2}. \tag{2.22}$$

The value $\pi_{11} - \pi_{12}$ (and, therefore, the coefficient π_{66}) can be determined from the relations (2.18) or (2.22), provided that the coordinate distributions of the birefringence along the diameters parallel to the x and y axes, are known. Besides, the coefficients π_{11} and π_{12} can be determined separately, using a standard interferometric technique [62].

2.2.2. *x*-cut disk

When the $LiNbO_3$ disk is cut perpendicular to the crystallographic x axis and the compressive force is applied along the z axis, the following components of the mechanical stress tensor are nonzero:

$$\sigma_2 = -\frac{2P}{\pi d}\left[\frac{\left(R-z\right)y^2}{\left(y^2+\left(R-z\right)^2\right)^2} + \frac{\left(R+z\right)y^2}{\left(y^2+\left(R+z\right)^2\right)^2} - \frac{1}{2R}\right], \tag{2.23}$$

$$\sigma_3 = -\frac{2P}{\pi d}\left[\frac{\left(R-z\right)^3}{\left(y^2+\left(R-z\right)^2\right)^2} + \frac{\left(R+z\right)^3}{\left(y^2+\left(R+z\right)^2\right)^2} - \frac{1}{2R}\right], \tag{2.24}$$

$$\sigma_4 = \frac{2P}{\pi d}\left[\frac{(R-z)^2 y}{\left(y^2+(R-z)^2\right)^2} - \frac{(R+z)^2 y}{\left(y^2+(R+z)^2\right)^2}\right], \tag{2.25}$$

Then the optical indicatrix equation becomes as follows:

$$\begin{aligned}&(B_1+\pi_{12}\sigma_2+\pi_{13}\sigma_3+\pi_{14}\sigma_4)x^2+\\&+(B_1+\pi_{11}\sigma_2+\pi_{13}\sigma_3-\pi_{14}\sigma_4)y^2+\\&+(B_3+\pi_{31}\sigma_2+\pi_{33}\sigma_3)z^2+2(\pi_{44}\sigma_4-\pi_{41}\sigma_2)yz=1.\end{aligned} \tag{2.26}$$

One can obtain the relations that describe the birefringence increment and the optical indicatrix rotation, using formula (2.26). For instance, for the light propagating along the *x* axis we get

$$\delta(\Delta n)_{23} = \frac{1}{2}\left[n_o^3(\pi_{11}\sigma_2+\pi_{13}\sigma_3-\pi_{14}\sigma_4)-n_e^3(\pi_{31}\sigma_2+\pi_{33}\sigma_3)\right], \tag{2.27}$$

$$\begin{aligned}&\tan 2\zeta_1 = \frac{2(\pi_{44}\sigma_4-\pi_{41}\sigma_2)}{B_2-B_3+(\pi_{11}-\pi_{31})\sigma_2+(\pi_{13}-\pi_{33})\sigma_3-\pi_{14}\sigma_4} \approx\\&\approx \frac{\bar{n}^3}{\Delta n_{32}}(\pi_{44}\sigma_4-\pi_{41}\sigma_2),\end{aligned} \tag{2.28}$$

where $\bar{n} = (n_3+n_2)/2$ and $\Delta n_{32} = n_3+n_2$.

Taking into account the relations (2.23)–(2.25), (2.27) and (2.28), we obtain under the condition $y = 0$ that

$$\sigma_2 = \frac{P}{\pi dR}, \tag{2.29}$$

$$\sigma_3 = -\frac{2P}{\pi d}\left[\frac{2R}{R^2-z^2}-\frac{1}{2R}\right], \tag{2.30}$$

$$\sigma_4 = 0. \tag{2.31}$$

Then the relation (2.27) for the birefringence increment takes the form

$$\delta(\Delta n)_{23} = \frac{P}{2\pi dR}\left[\left(n_o^3\pi_{11}-n_e^3\pi_{31}\right)+\left(n_e^3\pi_{33}-n_o^3\pi_{13}\right)\frac{3R^2+z^2}{R^2-z^2}\right]. \tag{2.32}$$

For the center of the disk ($z = y = 0$) we have

$$\delta(\Delta n)_{23} = \frac{P}{2\pi dR}\left[n_o^3(\pi_{11} - 3\pi_{13}) - n_e^3(\pi_{31} - 3\pi_{33})\right]. \quad (2.33)$$

Using the relation (2.32) and the dependence of birefringence increment on the z coordinate calculated for the $LiNbO_3$ crystals (Fig. 2-3), one can determine the combination $n_e^3\pi_{33} - n_o^3\pi_{13}$ of the piezooptic coefficients. In our simulations, we have taken the following piezooptic coefficients: $\pi_{11} = -0.38$ B, $\pi_{13} = 0.8$ B, $\pi_{31} = 0.5$ B and $\pi_{33} = 0.2$ B [60].

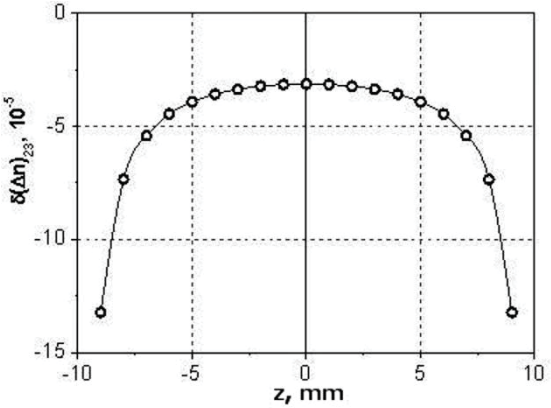

Fig. 2-3. Coordinate distribution of birefringence increment calculated along the compression diameter ($y = 0$) for x-cut $LiNbO_3$ disk: $P \parallel z$, $P = 100$ N, $d = 2$ mm and $R = 10$ mm [58].

Adapted with permission from Vasylkiv, Y., Savaryn, V., Smaga, I., Krupych, O., Skab, I., & Vlokh, R. (2011). Studies of piezooptic coefficients in $LiNbO_3$ crystals using a crystalline disk compressed along its diameter. Ukr. J. Phys. Opt., 12(4), 180–190. © O. G. Vlokh Institute of Physical Optics.

Subsequently, the combination of piezooptic coefficients $n_o^3\pi_{11} - n_e^3\pi_{31}$ can be determined using (2.33) and a known combination $n_e^3\pi_{33} - n_o^3\pi_{13}$. Moreover, the coefficient π_{41} can be found from the formula (2.28) whenever the optical indicatrix rotation angle is determined in the centre of the disk:

$$\tan 2\zeta_1 = \frac{\overline{n}^3}{\Delta n_{32}}\pi_{41}\frac{P}{\pi dR}. \quad (2.34)$$

As seen from the relation (2.28), the optical indicatrix rotation ζ_1 does not depend on the z coordinate and remains sufficiently small (for $LiNbO_3$ crystals we have $\zeta_1 = 0.01$ deg if $\pi_{41} = -0.88$ B [62]).

For the diameter perpendicular to the mechanical force ($z = 0$), we consider the following stress tensor components:

$$\sigma_2 = -\frac{2P}{\pi d}\left[\frac{2Ry^2}{\left(y^2+R^2\right)^2} - \frac{1}{2R}\right], \tag{2.35}$$

$$\sigma_3 = -\frac{2P}{\pi d}\left[\frac{2R^3}{\left(y^2+R^2\right)^2} - \frac{1}{2R}\right], \tag{2.36}$$

$$\sigma_4 = 0, \tag{2.37}$$

Then the birefringence increment is given by

$$\delta\left(\Delta n\right)_{23} = \frac{P\left(R^2-y^2\right)}{\pi d} \times \\ \times \frac{\left(n_o^3\pi_{11} - n_e^3\pi_{31}\right)\left(R^2-y^2\right) + \left(n_e^3\pi_{33} - n_o^3\pi_{13}\right)\left(3R^2+y^2\right)}{2R\left(y^2+R^2\right)^2}. \tag{2.38}$$

At $y = 0$, the birefringence increment in the centre of the disk reads as

$$\delta\left(\Delta n\right)_{23} = \frac{P}{2\pi dR}\left[n_o^3\left(\pi_{11}-3\pi_{13}\right) - n_e^3\left(\pi_{31}-3\pi_{33}\right)\right]. \tag{2.39}$$

Using the dependence of birefringence increment on the y coordinate (see Fig. 2-4), one can determine the combination of piezooptic coefficients given by formula (2.39).

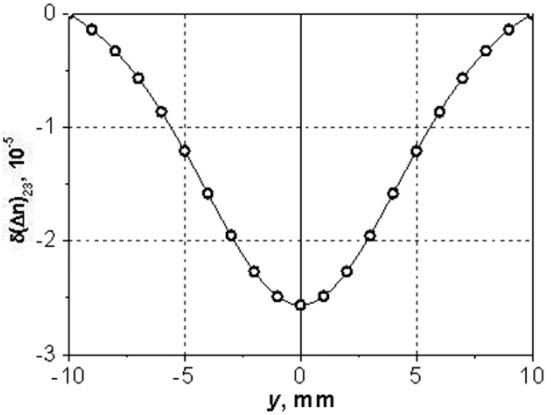

Fig. 2-4. Coordinate distribution of birefringence increment calculated along the diameter $z = 0$ for compressed x-cut $LiNbO_3$ disk: $P \parallel z$, $P = 100$ N, $d = 2$ mm and $R = 10$ mm [58].

Adapted with permission from Vasylkiv, Y., Savaryn, V., Smaga, I., Krupych, O., Skab, I., & Vlokh, R. (2011). Studies of piezooptic coefficients in $LiNbO_3$ crystals using a crystalline disk compressed along its diameter. Ukr. J. Phys. Opt., 12(4), 180–190. © O. G. Vlokh Institute of Physical Optics.

It is worthwhile to note that the optical indicatrix rotation angle, which is expressed by the formula

$$\mathrm{tg}2\zeta_1 = -\frac{\bar{n}^3}{\Delta n_{32}}\pi_{41}\sigma_2 = -\frac{\bar{n}^3}{\Delta n_{32}}\pi_{41}\frac{P}{\pi dR}\frac{\left(R^2 - y^2\right)^2}{\left(y^2 + R^2\right)^2}, \tag{2.40}$$

depends on the y coordinate. Then this relation can serve as an additional tool for determining the coefficient π_{41}. The corresponding dependence is displayed in Fig. 2-5.

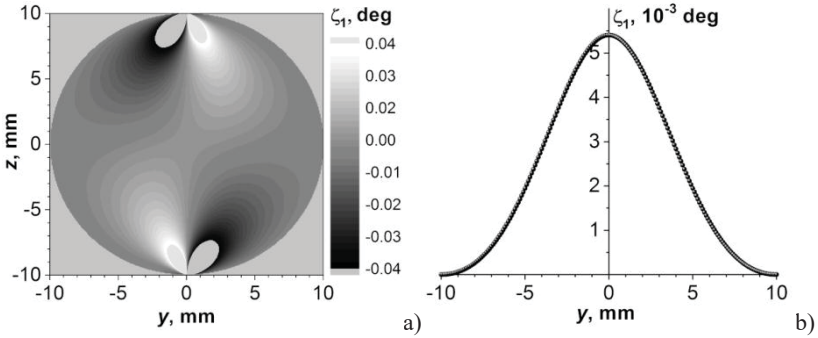

Fig. 2-5. Coordinate distributions of optical indicatrix rotation calculated within the cross-section (a) and along the diameter $z = 0$ (b) for compressed x-cut $LiNbO_3$ disk: $P \parallel z$, $P = 100$ N, $d = 2$ mm and $R = 10$ mm [58].

Adapted with permission from Vasylkiv, Y., Savaryn, V., Smaga, I., Krupych, O., Skab, I., & Vlokh, R. (2011). Studies of piezooptic coefficients in $LiNbO_3$ crystals using a crystalline disk compressed along its diameter. Ukr. J. Phys. Opt., 12(4), 180–190. © O. G. Vlokh Institute of Physical Optics.

2.2.3. *y*-cut disk

Let us deal with the $LiNbO_3$ disk perpendicular to the y axis and a compressive force be applied along the x axis. Then the stress components are determined by the relations

$$\sigma_3 = -\frac{2P}{\pi d}\left[\frac{(R-x)z^2}{\left(z^2+(R-x)^2\right)^2}+\frac{(R+x)z^2}{\left(z^2+(R+x)^2\right)^2}-\frac{1}{2R}\right], \tag{2.41}$$

$$\sigma_1 = -\frac{2P}{\pi d}\left[\frac{(R-x)^3}{\left(z^2+(R-x)^2\right)^2}+\frac{(R+x)^3}{\left(z^2+(R+x)^2\right)^2}-\frac{1}{2R}\right], \tag{2.42}$$

$$\sigma_5 = \frac{2P}{\pi d}\left[\frac{(R-x)^2 z}{\left(z^2+(R-x)^2\right)^2}-\frac{(R+x)^2 z}{\left(z^2+(R+x)^2\right)^2}\right]. \tag{2.43}$$

In this case, the equation for the optical indicatrix reads as

$$\left(B_1+\pi_{11}\sigma_1+\pi_{13}\sigma_3\right)x^2+\left(B_1+\pi_{12}\sigma_1+\pi_{13}\sigma_3\right)y^2+$$
$$+\left(B_3+\pi_{31}\sigma_1+\pi_{33}\sigma_3\right)z^2+2\pi_{41}\sigma_1 yz+2\pi_{44}\sigma_5 xz+4\pi_{14}\sigma_6 xy=1. \quad (2.44)$$

Then the birefringence increment takes the form

$$\delta\left(\Delta n\right)_{31}\approx\frac{1}{2}\left[n_o^3\left(\pi_{11}\sigma_1+\pi_{13}\sigma_3\right)-n_e^3\left(\pi_{31}\sigma_1+\pi_{33}\sigma_3\right)\right], \quad (2.45)$$

and the rotation ζ_2 of optical indicatrix about the y axis is given by the relation

$$\tan 2\zeta_2=\frac{2\pi_{44}\sigma_5}{B_1-B_3+\left(\pi_{11}-\pi_{31}\right)\sigma_1+\left(\pi_{13}-\pi_{33}\right)\sigma_3}\approx$$
$$\approx\pi_{44}\sigma_5\frac{\bar{n}^3}{\Delta n_{31}}=\pi_{44}\frac{\bar{n}^3}{\Delta n_{31}}\frac{2P}{\pi d}\left[\frac{\left(R-x\right)^2 z}{\left(z^2+\left(R-x\right)^2\right)^2}-\frac{\left(R+x\right)^2 z}{\left(z^2+\left(R+x\right)^2\right)^2}\right]. \quad (2.46)$$

Formula (2.46) enables one to determine the coefficient π_{44}, using the experimental dependences of optical indicatrix rotation on the x and z coordinates. The corresponding coordinate dependence of optical indicatrix rotation obtained by numerical simulations is shown in Fig. 2-6. Here we have taken the piezooptic coefficient value π_{44} = 2.25 B [60].

The birefringence increment in the direction perpendicular to the compression axis (x = 0) is as follows:

$$\delta(\Delta n)_{23}=\frac{P\left(R^2-z^2\right)}{\pi d}\times$$
$$\times\frac{\left(n_e^3\pi_{31}-n_o^3\pi_{11}\right)\left(3R^2+z^2\right)+\left(n_o^3\pi_{13}-n_e^3\pi_{33}\right)\left(R^2-z^2\right)}{2R\left(z^2+R^2\right)^2}. \quad (2.47)$$

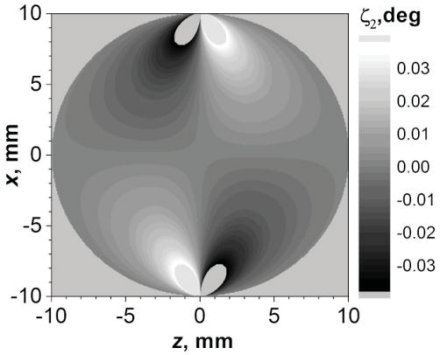

Fig. 2-6. 2D map of optical indicatrix rotation calculated for the compressed *y*-cut $LiNbO_3$ disk: $P \parallel x$, $P = 100$ N, $d = 2$ mm and $R = 10$ mm [58].
Adapted with permission from Vasylkiv, Y., Savaryn, V., Smaga, I., Krupych, O., Skab, I., & Vlokh, R. (2011). Studies of piezooptic coefficients in $LiNbO_3$ crystals using a crystalline disk compressed along its diameter. Ukr. J. Phys. Opt., 12(4), 180–190. © O. G. Vlokh Institute of Physical Optics.

Then the dependence of birefringence increment at the x axis ($z = 0$) is defined as

$$\delta(\Delta n)_{31} \approx -\frac{P}{2R\pi d}\left[\left(n_o^3\pi_{11} - n_e^3\pi_{31}\right)\frac{3R^2 + x^2}{\left(R^2 - x^2\right)} + \left(n_e^3\pi_{33} - n_o^3\pi_{13}\right)\right]. \quad (2.48)$$

Hence, combinations of the piezooptic coefficients can be determined basing on the coordinate dependences of birefringence increment along the vertical ($z = 0$) and horizontal ($x = 0$) diameters.

The phenomenological relations describing the induced changes in the birefringence and the optical indicatrix rotation for crystalline disks have been derived for all the principal crystalline sections of all the symmetry groups [57] (see Appendix A). They can be used in practice while calculating the piezooptic coefficients or their combinations. For this purpose, one has to fit experimental dependences of the optical anisotropy parameters along the diameters and along the chords parallel and perpendicular to the compression direction using the corresponding formulae. Then the piezooptic coefficients under interest can be obtained as the fitting coefficients.

2.2.4. Experimental procedures and results

In order to check experimentally our method for determining the piezooptic coefficients, we have employed the 2D polarimeter described in detail in paragraph 1.2.1. Here a circularly polarized incident beam, which is not sensitive to orientation of the optical indicatrix, has been used for measuring the optical birefringence. A crystalline sample can be described by a standard linear-retarder model. In other words, it is characterized by the two parameters of optical anisotropy, the orientation angle of optical indicatrix and the linear birefringence.

In the first experiment [58], we have prepared a sample of $LiNbO_3$ made in the shape of disk, with the radius 7.5 mm, the thickness 3 mm, and the sample faces perpendicular to the crystal physical axis *z*. Then the *yz*-plane is parallel to one of the mirror symmetry planes. The loading force (P = 19.8 N) has been applied along the diameter parallel to the *y* axis.

As a result, 2D distributions of the induced birefringence and the optical indicatrix rotation have been obtained for the compressed sample. After fitting the experimental distribution of the birefringence along the compression axis by the relation (2.18), we have calculated the piezooptic coefficient $|\pi_{66}| = |\pi_{11} - \pi_{12}| = 0.20$ B. This value is less than that obtained in the work [60] ($\pi_{11} - \pi_{12} = -0.47$ B) using the interferometric method and a traditional sample-loading scheme. For comparison, the coefficient $\pi_{66} = \pi_{11} - \pi_{12}$ has also been measured with the four-point bend method [63, 64]. The value obtained in these experiments (–0.57±0.08 B) is almost three times larger than that obtained in the experiment with compressed disk.

Hence, the piezooptic coefficient obtained in our compressed-disk experiment differs significantly from the data obtained using the other methods, including the data reported in Ref. [60]. To explain this discrepancy, we have repeated our experiments with the same configuration of the 2D polarimeter but a different crystalline sample.

The second disk-shaped $LiNbO_3$ sample has been prepared from a plate with a minimal residual birefringence along the z direction. The diameter of the disk is equal to 13.74 mm and its thickness 2.32 mm (see Fig. 2-7). The loading force is applied along the y axis.

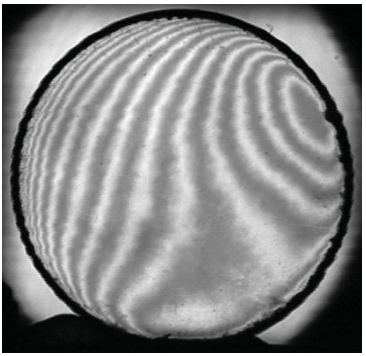

Fig. 2-7. Pattern of a disk-shaped crystalline sample seen with a polarimeter. Interference fringes are caused by multiple reflections from sample surfaces and indicate their imperfect parallelism.
Adapted with permission from Savaryn, V., Krupych, O., & Vlokh, R. (2014). Refined measurements of piezooptic coefficient π_{66} for the lithium niobate crystals, using a crystalline disk compressed along its diameter. Ukr. J. Phys. Opt., 15(1), 30–37. © O. G. Vlokh Institute of Physical Optics.

To provide circular polarization of the incident beam, the fast axis of the compensator has been initially set parallel to the transmission axis of the polarizer. The corresponding azimuth is indicated as C_0. After that, the compensator has been rotated such that the angular position $C_1 = C_0 - 45$ deg is achieved.

The birefringence Δn_{12} induced by compressing the z-cut $LiNbO_3$ disk along its y axis is expressed by the relation (2.15). Then the optical retardation Δ can be written as

$$\Delta = d\Delta n_{12} = -\frac{d}{2} n_o^3 \left(\pi_{11} - \pi_{12}\right) \sqrt{\left(\sigma_1 - \sigma_2\right)^2 + 4\sigma_6^2}\,. \tag{2.49}$$

For the case of diameter of "load" ($x = 0$), the dependence of the optical retardation Δ on the y coordinate is expressed through the birefringence Δn_{12} given by (2.18):

$$\Delta = d\Delta n_{12} = -\frac{d}{2} n_0^3 \pi_{66} \frac{2RP}{\pi d\left(R^2 - y^2\right)} = -\frac{P}{\pi} n_0^3 \pi_{66} \frac{R}{R^2 - y^2}. \qquad (2.50)$$

Taking formula (2.22) into account, one can write the dependence of optical retardation Δ on the x coordinate for the alternative "perpendicular" diameter ($y = 0$) as follows:

$$\Delta = -\frac{d}{2} n_0^3 \pi_{66} \frac{2P}{\pi d} \frac{R(R^2 - x^2)}{(R^2 + x^2)^2} = -\frac{P}{\pi} n_0^3 \pi_{66} \frac{R(R^2 - x^2)}{(R^2 + x^2)^2}. \qquad (2.51)$$

Hence, the coefficient π_{66} can be determined by fitting, with the functions (2.50) or (2.51), either of the experimental dependences of optical retardation Δ on the coordinate along the "loading" or "perpendicular" diameters.

The coordinate dependences of the optical retardation and the optical indicatrix orientation in the sample have been obtained experimentally at the loading forces 0, 16.30 and 57.06 N. An example is presented in Fig. 2-8. The both dependences agree quite well with the theoretical formulae (2.14) and (2.49).

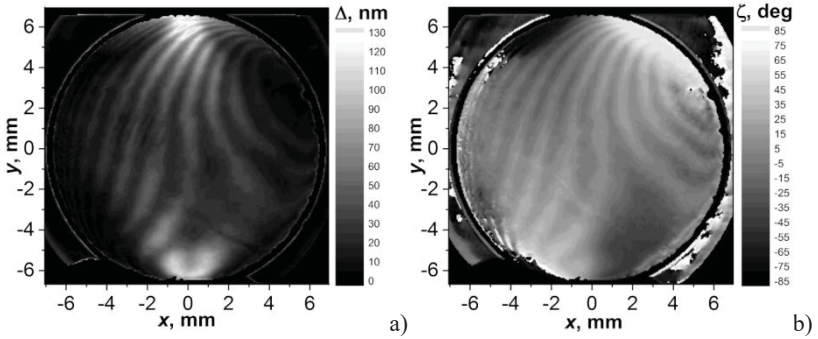

Fig. 2-8. 2D maps of optical retardation (a) and optical indicatrix rotation angle (b) induced in a disk-shaped $LiNbO_3$ sample by the loading force 57.06 N ($\lambda = 632.8$ nm). Compensator orientation is given by $C_1 = C_0 - 45$ deg.

Adapted with permission from Savaryn, V., Krupych, O., & Vlokh, R. (2014). Refined measurements of piezooptic coefficient π_{66} for the lithium niobate crystals, using a crystalline disk compressed along its diameter. Ukr. J. Phys. Opt., 15(1), 30–37. © O. G. Vlokh Institute of Physical Optics.

After that, the spatial distribution of the optical retardation obtained at the loading force 16.30 N has been subtracted from the distribution corresponding to the loading force 57.06 N. The resulting "difference" distribution of the optical retardation increment $\delta\Delta$ is shown in Fig. 2-9. Using this distribution, we have obtained the coordinate dependences of the $\delta\Delta$ parameter for the both cases of "loading" and "perpendicular" diameters.

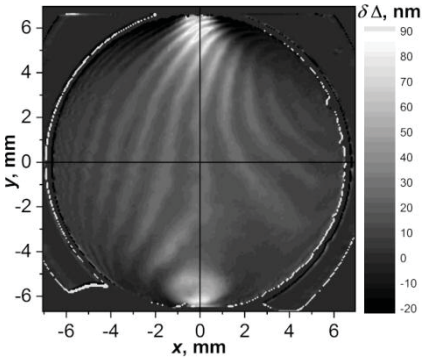

Fig. 2-9. 2D map of optical retardation increment $\delta\Delta$ in a disk-shaped $LiNbO_3$ sample, as observed after changing the loading force from 16.30 to 57.06 N (λ = 632.8 nm). Compensator orientation is given by $C_1 = C_0 - 45$ deg.
Adapted with permission from Savaryn, V., Krupych, O., & Vlokh, R. (2014). Refined measurements of piezooptic coefficient π_{66} for the lithium niobate crystals, using a crystalline disk compressed along its diameter. Ukr. J. Phys. Opt., 15(1), 30–37. © O. G. Vlokh Institute of Physical Optics.

Fig. 2-10a presents the experimental data and the fitting curve, from which the coefficient $\pi_{66} = -0.571 \pm 0.012$ B has been calculated.

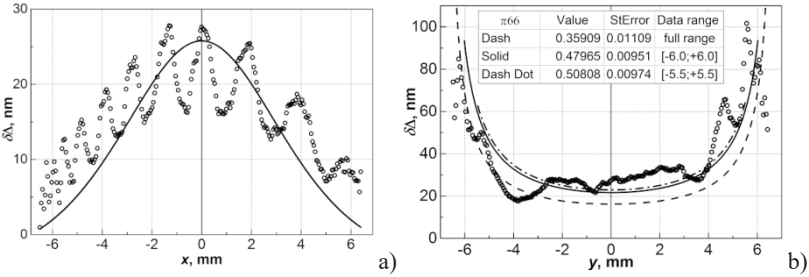

Fig. 2-10. Dependences of optical retardation increment $\delta\Delta$ on the x coordinate (along "perpendicular" diameter) (a) and on the y coordinate (along diameter of "load") (b), as calculated for a disk-shaped $LiNbO_3$ sample after changing the loading force from 16.30 to 57.06 N ($\lambda = 632.8$ nm). Compensator orientation is given by $C_1 = C_0 - 45$ deg.

Adapted with permission from Savaryn, V., Krupych, O., & Vlokh, R. (2014). Refined measurements of piezooptic coefficient π_{66} for the lithium niobate crystals, using a crystalline disk compressed along its diameter. Ukr. J. Phys. Opt., 15(1), 30–37. © O. G. Vlokh Institute of Physical Optics.

The dependence of $\delta\Delta$ on the x coordinate for the "perpendicular" diameter has been fitted by the function given by (2.51), with replacement of P and Δ by ΔP and $\delta\Delta$:

$$\delta\Delta = -\frac{\Delta P}{\pi} n_0^3 \pi_{66} \frac{R(R^2 - x^2)}{(R^2 + x^2)^2}. \tag{2.52}$$

The dependence $\delta\Delta$ on the y coordinate for the "loading" diameter has been fitted by the dependence similar to equation (2.50):

$$\delta\Delta = -\frac{\Delta P}{\pi} n_0^3 \pi_{66} \frac{R}{R^2 - y^2}. \tag{2.53}$$

It can be seen from the relation (2.53) that, in the vicinity of the points where the loading force is applied ($|y| \to R$), the denominator approaches zero, which gives rise to $\delta\Delta$ singularity. The reason for its appearance can be found in formula (2.2). Indeed, according to (2.2), the component σ_2 becomes infinite when $x = 0$ and $|y| = R$. This means that the relation (2.2) represents a limited model which cannot be applied to the spatial regions

close to the points where the loading force is applied. The question arises: for which range of y coordinate one can apply formula (2.53) such that the approach remained correct from the viewpoint of data fitting?

To solve this problem practically, we have fitted the experimental data in the following different ranges (see Fig. 2-10b): $|y| < 6.5$ mm $\approx 0.95R$ (i.e., the full data range); $|y| < 6.0$ mm $\approx 0.88R$; $|y| < 5.5$ mm $\approx 0.80R$.

The piezooptic coefficients π_{66} obtained for these data ranges amount to 0.359±0.010, –0.480±0.010 and –0.508±0.010 B, respectively. It is evident that narrowing of the data range (from the overall one to the range defined by $|y| < 0.80R$) brings the π_{66} value closer to that obtained in the case of "perpendicular" diameter. Further reduction of the data range does not increase the π_{66} value, although the quality of fitting deteriorates due to negative influence of multiple-reflection fringes. Thus, the optimal data range for the case of "loading" diameter is $|y| < 0.80R$. The corresponding value of the piezooptic coefficient π_{66} is equal to –0.508±0.010 B.

To increase the resulting accuracy for the piezooptic coefficient π_{66}, we have repeated the procedure described above in case when the circular polarization of the incident beam has the opposite sign. To do this, the compensator has been rotated from its initial azimuthal position $C_1 = C_0 - 45$ deg to the position $C_2 = C_0 + 45$ deg. The experimental dependences and the fitting results for this case are depicted in Fig. 2-11.

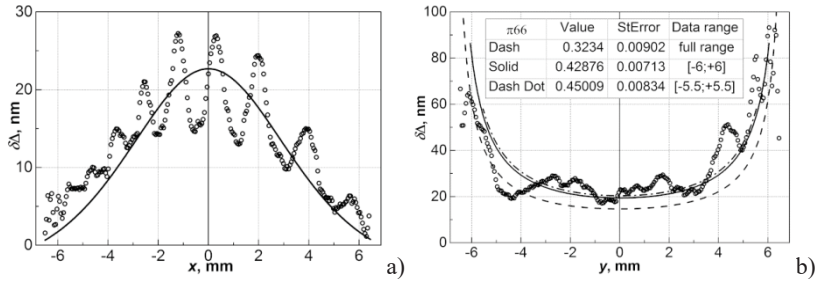

Fig. 2-11. Dependences of optical retardation increment $\delta\Delta$ on the x coordinate (along "perpendicular" diameter) (a) and on the y coordinate (along diameter of "load") (b), as measured for a disk-shaped $LiNbO_3$ sample after changing the loading force from 16.30 to 57.06 N ($\lambda = 632.8$ nm). Compensator orientation is given by $C_2 = C_0 + 45$ deg.

Adapted with permission from Savaryn, V., Krupych, O., & Vlokh, R. (2014). Refined measurements of piezooptic coefficient π_{66} for the lithium niobate crystals, using a crystalline disk compressed along its diameter. Ukr. J. Phys. Opt., 15(1), 30–37. © O. G. Vlokh Institute of Physical Optics.

We obtain the piezooptic coefficient π_{66} equal to –0.502±0.009 B for the case of "perpendicular" diameter (Fig. 2-11a) and –0.450±0.008 B for the diameter of "load" (Fig. 2-11b). Hence, the average value and the error of the piezooptic coefficient π_{66} amount to $\langle \pi_{66} \rangle = -0.508$ B and $\Delta\pi_{66} = 0.049$ B, respectively. The corresponding confidence interval for the π_{66} parameter is given by [–0.459 B; –0.557 B], which is consistent with both the data reported in the work [60] ($\pi_{66} = -0.47$ B) and the data obtained using the four-point bending method [64] ($\pi_{66} = -0.573 \pm 0.079$ B).

These considerations explain exhaustively the inaccurate value of the piezooptic coefficient π_{66} reported in Ref. [58] for the $LiNbO_3$ crystals. Namely, the reason for this error is unreasonable choice of the fitting interval. Instead of the correct interval [$-0.8R$; $+0.8R$] providing the correct results, in [58] the interval equal to the full disk diameter ([$-R$; $+R$]) has been chosen. This feature must be properly taken into account when calculating the piezooptic coefficients from the experimental dependences of optical retardation along the diameter of "load".

Summarizing, the method for measuring piezooptic coefficients, which is based on diametrical compression of disk-shaped samples, can be successfully used to study either crystalline or amorphous materials.

SECTION 3

OPTICAL ANISOTROPY OF CRYSTALS INDUCED BY MECHANICAL TORSION

3.1. Torsion-optical method for measuring piezooptic coefficients

When measuring piezooptic coefficients, one has to solve a problem of non-uniform distribution of mechanical stresses in a sample under study, which appears due to barrel-like deformations. In particular, a solution becomes possible whenever one forms the mechanical stresses with a predetermined 2D configuration. The example may be a so-called four-point bending method [65], in which a spatial distribution of mechanical stresses is predetermined. This method is often used to determine the piezooptic coefficients.

The above consideration is also valid when a torsion moment is applied to a sample. Moreover, the use of torsion allows for determining the values of so-called non-principal piezooptic coefficients $\pi_{\lambda\mu}$ ($\lambda = 1\ldots6$ and $\mu = 4\ldots6$). Usually, these coefficients are not determined at all due to complicated geometric conditions of appropriate experiments or are simply recalculated in a cumbersome way from the results of indirect measurements [66, 67], thus leading to increasing errors.

To explain a possibility for measuring the non-principal piezooptic coefficients with the torsion-optic method, we remind that twisting of rods with circular sections of a radius R by a moment M_z applied to the ends of rod around the z axis results in appearance of only shear components of the mechanical stress tensor [68]:

$$\sigma_\mu = \frac{2M_z}{\pi R^4}\left(x\delta_{4\mu} - y\delta_{5\mu}\right), \tag{3.1}$$

where $\delta_{4\mu}$ and $\delta_{5\mu}$ are the Kronecker symbols. Thus, the mechanical stress components σ_4 and σ_5 appear when a cylindrical sample is twisted around

the z axis. These components are linearly dependent on the x and y coordinates, respectively. They become zero at $x = y = 0$ (i.e., just at the torsion axis).

According to ASTM (American Society for Testing and Materials) standards [69], one has to determine any piezooptic coefficient (even that for an isotropic material) with at least three different methods used during the phase-difference measurements, e.g. four-point bending, compression and stretching. On the other hand, an acoustooptic Dixon−Cohen method can be used, which also allows for determining the elastooptic coefficients [70, 71] with sufficiently high accuracy (3% in the case of principal and 10% in the case of non-principal coefficients). However, this method cannot determine the signs of elastooptic coefficients.

In this regard, it is advisable to analyze the conditions under which non-principal piezooptic coefficients can be determined due to twisting of crystals and to obtain the appropriate analytical relations for the crystals of different point symmetry groups [72]. Such an analysis is based on the equation for optical indicatrix deformed by a torsion moment [73].

3.1.1. Isotropic media and crystals related to cubic system

In the case of light propagation in a twisted isotropic medium (e.g., in an initially isotropic fiber [74]), the piezooptic matrix (1.10) contains a single independent coefficient $\pi_{44} = \pi_{55} = \pi_{66}$, which describes the change in refractive indices due to shear stresses. All the other coefficients associated with the shear stresses are zero.

Let us consider the optical indicatrix equation for an isotropic medium twisted around the z axis (for the isotropic media, we choose the xyz system as a laboratory coordinate system):

$$B_{11}^0 x^2 + B_{11}^0 y^2 + B_{11}^0 z^2 + 2\pi_{44}\sigma_{23}(x)yz + 2\pi_{44}\sigma_{13}(y)xz = 1, \tag{3.2}$$

where $\pi_{44} = \pi_{11} - \pi_{12}$. When the light propagates along the z axis, the equation that describes the cross-section of the optical indicatrix by the plane $z = 0$ is given by

$$B_{11}^0 x^2 + B_{11}^0 y^2 = 1. \tag{3.3}$$

Equation (3.3) shows that the cross-section of the optical indicatrix by the plane $z = 0$ is a circle. This indicates that the torsion moment does not induce the birefringence along the z direction. For the light propagation

along any other direction perpendicular to the torsion axis (e.g., along the y axis), the equation for the cross-section of optical indicatrix by the corresponding orthogonal plane (e.g., with the plane $y = 0$) is as follows:

$$B_{11}^0 x^2 + B_{11}^0 z^2 + 2\pi_{44}\sigma_{13}(y)xz = 1. \tag{3.4}$$

Under these conditions, the induced birefringence can be written as

$$\Delta n_{13} = n^3 \pi_{44} \sigma_{13}(y) = n^3 \pi_{44} \frac{2M_z}{\pi R^4} y. \tag{3.5}$$

As seen from the relation (3.5), the birefringence is linearly dependent on the y coordinate that corresponds to the direction of propagation of the light wave. However, the total birefringence along this direction should be zero, since the origin of the coordinate system ($y = 0$) is located in the geometric centre of the sample. This statement can be easily proved using the Jones matrix approach.

To do this, we consider a sample divided into, e.g., 6000 uniform layers of the same thickness d_m, which are perpendicular to the y axis. The resultant Jones matrix for this sample can be obtained by multiplying the Jones matrices of all elementary layers [72]:

$$J = \prod_{m=1}^{6000} J_m, \tag{3.6}$$

where

$$J_m = \begin{vmatrix} \cos\left(\frac{\Gamma_m}{2}\right) + i\sin\left(\frac{\Gamma_m}{2}\right)\cos 2\zeta_m & i\sin(\Gamma_m/2)\sin 2\zeta_m \\ i\sin(\Gamma_m/2)\sin 2\zeta_m & \cos\left(\frac{\Gamma_m}{2}\right) - i\sin\left(\frac{\Gamma_m}{2}\right)\cos 2\zeta_m \end{vmatrix}. \tag{3.7}$$

In formula (3.7), $\Gamma_m = 2\pi d_m \left\{ n^3 \pi_{44} \frac{2M_z}{\pi R^4} y \right\} / \lambda$ is the phase difference of the elementary layer m, which is induced by the torsion stress, λ denotes the wavelength of light wave, and ζ_m the orientation angle of optical indicatrix.

In the mathematical simulation, the following parameters have been used: $M_z = 0.16$ N×m, $n = 2.0$, R =3 mm, $\pi_{44} = 5.0 \times 10^{-12}$ m^2/N and $\lambda = 632.8$ nm. Since the imaginary part of the component j_{11} of the resultant Jones matrix is equal to $\mathrm{Im} j_{11} = \sin(\Gamma/2)\cos 2\zeta$ at $\zeta = \pm 45$ deg, the effective induced phase difference can generally be obtained from the relation $\Gamma = 2\mathrm{asin}(\mathrm{Im} j_{11})$, and the corresponding effective birefringence from the expression $\Delta n = \Gamma\lambda/4\pi R$. As a result, we have obtained that both the resultant phase difference and the effective birefringence are zero.

Moreover, the average value of the function $\Delta n_{13} = f(y)$ determined by the relation (3.5) is also zero:

$$\Delta n_{13} = \frac{1}{2\sigma_{13}} n^3 \pi_{44} \int_{-\sigma_{13}}^{+\sigma_{13}} \sigma_{13}(y) d\sigma_{13} = \frac{1}{2y} n^3 \pi_{44} \frac{2M_z}{\pi R^4} \int_{-y}^{+y} y dy = 0. \qquad (3.8)$$

Indeed, the optical-indicatrix rotation angle can be represented as $\zeta_y = +45$ deg at $y > 0$ and $\zeta_y = -45$ deg at $y < 0$. Due to this circumstance, the birefringence becomes equal to zero when the light passes the entire sample. In other words, the piezooptic coefficient π_{44} cannot be determined in this experimental geometry. The fact that the birefringence does not depend on the *x* and *z* coordinates represents a drawback of this geometry.

Let us consider an inclined incidence of light beam with respect to the torsion axis, e.g. the incidence at an angle 45 deg with respect to the y and z axes (Fig. 3-1).

Then the impermeability tensor must be rewritten in some coordinate system $x'y'z'$, which is rotated by the angle 45 deg around the *x* axis. The optical indicatrix equation in this coordinate system is as follows:

$$\begin{aligned} &B_{11}^0 x'^2 + (B_{11}^0 - \pi_{44}\sigma_{23}(x)) y'^2 + (B_{11}^0 + \pi_{44}\sigma_{23}(x)) z'^2 + \\ &+\sqrt{2}\pi_{44}\sigma_{13}(y) x'z' - \sqrt{2}\pi_{44}\sigma_{13}(y) x'y' = 1. \end{aligned} \qquad (3.9)$$

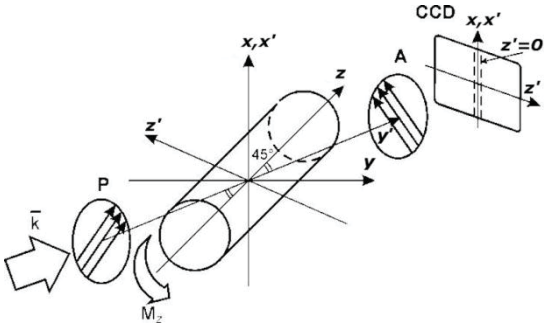

Fig. 3-1. Experimental geometry used to determine piezooptic coefficient π_{44} in isotropic media or crystals of cubic system [72].
Skab, I., Smaga, I., Savaryn, V., Vasylkiv, Yu., Vlokh, R.: Torsion method for measuring piezooptic coefficients. Cryst. Res. Technol. 2011. 46(1). 23–36. Copyright Wiley-VCH GmbH. Reproduced with permission.

For the case of light propagation along the y' axis, one has to consider the cross-section of the optical indicatrix (3.9) by the plane $y' = 0$:

$$B_{11}^0 x'^2 + (B_{11}^0 + \pi_{44}\sigma_{23}(x))z'^2 + \sqrt{2}\pi_{44}\sigma_{13}(y)x'z' = 1. \tag{3.10}$$

Following from equation (3.10), the eigenvalues of the imprmeability tensor and the principal refractive indices are given respectively by the expressions:

$$B'_{1,\,33} = B_{11}^0 + \frac{1}{2}\pi_{44}\sigma_{23}(x) \pm \frac{1}{2}\pi_{44}\sqrt{\sigma_{23}^2(x) + 2\sigma_{13}^2(y)}, \tag{3.11}$$

$$n_{1',3'} = n - \frac{1}{4}n^3\pi_{44}\left(\sigma_{23}(x) \pm \sqrt{\sigma_{23}^2(x) + 2\sigma_{13}^2(y)}\right). \tag{3.12}$$

It follows from formula (3.12) that the induced birefringence is determined not only by the component σ_{13} but also by the component σ_{23}:

$$\Delta n_{1'3'} = \frac{1}{2}n^3\pi_{44}\sqrt{\sigma_{23}^2(x) + 2\sigma_{13}^2(y)}. \tag{3.13}$$

In this case we deal with the cross-sections $z'x'$ or $z'x$ orthogonal to the light beam. Then the component σ_{13} must depend on the y and z'

coordinates, while the component σ_{23} must depend only on the x coordinate. If we scan the light beam along the x axis, the equations $z' = 0$ and $\sigma_{13} = 0$ can be satisfied. Hence, the relation (3.13) is reduced to

$$\Delta n_{1'3'} = \frac{1}{2} n^3 \pi_{44} \sigma_{23}(x) = n^3 \pi_{44} \frac{M_z}{\pi R^4} x, \tag{3.14}$$

In its turn, the piezooptic coefficient π_{44} can be determined from the relation (3.14):

$$\pi_{44} = \pi_{11} - \pi_{12} = \frac{\Delta n_{1'3'} \pi R^4}{n^3 M_z x}. \tag{3.15}$$

The above analysis is also valid for the crystals of cubic system, provided that the inequality $\pi_{44} \neq \pi_{11} - \pi_{12}$ holds for the piezooptic coefficients of the point symmetry groups 23 and *m*3. Besides, in the case of light incidence at some nonzero angle with respect to the torsion axis, an immersion liquid must be used in the experiment.

3.1.2. Crystals and textures of point symmetry groups 422, $4mm$, $\bar{4}2m$, $4/mmm$, 622, $6mm$, $\bar{6}m2$, $6/mmm$, $\infty 2$, ∞m and ∞/mm

The piezooptic tensor (1.10) for this type of medium contains two independent coefficients associated with the shear stresses. It differs by the inequality $\pi_{44} = \pi_{55} \neq \pi_{66}$ from the tensor peculiar for the crystals of cubic system.

For these media, the piezooptic coefficient π_{44} can be determined under the following experimental conditions: (i) application of the torsion moment $\mathbf{M}$ with some nonzero components and (ii) direction of light propagation (i.e., direction of the wave vector $\mathbf{k}$) defined as $(M_x, k \| y)$, $(M_y, k \| x)$, $(M_z, k \| x)$ or $(M_z, k \| y)$. This is because, for all of these experimental geometries, the induced birefringence increment depends quadratically on the components of mechanical stress tensor and, as a result, on the squared optical path [73]. At the same time, the shear stress components change their signs where the principal planes of the Cartesian coordinate system intersect one another, i.e. in the planes that cross the torsion axis. In such a

case, the above-mentioned quadratic relationship would lead to the appearance of birefringence increment of the same sign in front and behind the coordinate planes. As a result, the total birefringence increment is not zero.

We obtain the relation which can be used for determining the effective birefringence (e.g., in the case $(M_z, k \| x)$) from the Jones matrices and the relations (3.6) and (3.7). In this case the induced birefringence is equal to $\delta(\Delta n)_{23} = \dfrac{2n_o^2 n_e^2 (n_o^3 + n_e^3)}{n_o^2 - n_e^2} \pi_{44}^2 \dfrac{M_z^2}{\pi^2 R^8} x^2$ and, therefore, the phase difference is determined by the relation $\Gamma_m = 2\pi d_m \left\{ \dfrac{2n_o^2 n_e^2 (n_o^3 + n_e^3)}{n_o^2 - n_e^2} \pi_{44}^2 \dfrac{M_z^2}{\pi^2 R^8} x^2 \right\} / \lambda$.

In our simulations, we have found that the effective birefringence increment is $\sim 3.7 \times 10^{-7}$ (here we choose the simulation parameters the same as in the case of isotropic media, i.e. $n_o = 2.0$ and $n_e = 1.99$).

On the other hand, the average value of the function $\delta(\Delta n)_{23} = f(x)$ describing the coordinate dependence of the birefringence can be written as

$$\begin{aligned} \delta(\Delta n)_{23} &= \frac{1}{4\sigma_{23}} \frac{n_o^2 n_e^2 (n_o^3 + n_e^3)}{n_o^2 - n_e^2} \pi_{44}^2 \int_{-\sigma_{23}}^{+\sigma_{23}} \sigma_{23}^2(x) d\sigma_{23} = \\ &= \frac{1}{x} \frac{n_o^2 n_e^2 (n_o^3 + n_e^3)}{n_o^2 - n_e^2} \pi_{44}^2 \frac{M_z^2}{\pi^2 R^8} \int_{-x}^{+x} x^2 dx = \frac{n_o^2 n_e^2 (n_o^3 + n_e^3)}{n_o^2 - n_e^2} \pi_{44}^2 \frac{M_z^2}{\pi^2 R^8} \frac{2x^2}{3}. \end{aligned} \tag{3.16}$$

For the case $x = R$, $n_o \approx n_e = \bar{n}$ and $n_o - n_e = \Delta n$, the equation (3.16) reads as

$$\delta(\Delta n)_{23} = \frac{2}{3} \frac{\bar{n}^6}{\Delta n} \pi_{44}^2 \frac{M_z^2}{\pi^2 R^6}. \tag{3.17}$$

Thus, following from (3.17) and the data derived for the dependence of induced birefringence on the torsion momentum (Fig. 3-2a), one can easily determine the corresponding piezooptic coefficient:

$$\pi_{44} = \frac{\pi R^3}{\bar{n}^3 M_z} \sqrt{\frac{3}{2} \Delta n \, \delta(\Delta n)_{23}}. \tag{3.18}$$

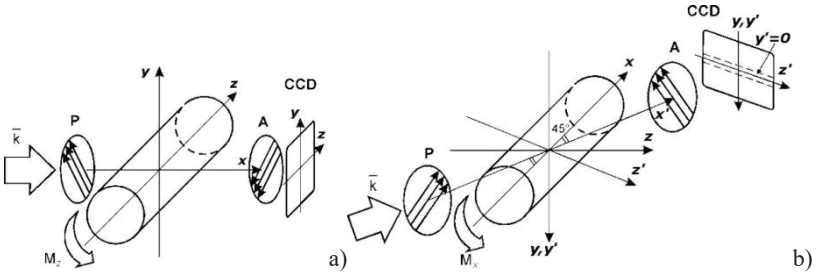

Fig. 3-2. Experimental geometries used for measuring piezooptic coefficients π_{44} (a) and π_{66} (b) in the crystals and textures that belong to the point symmetry groups 422, $4mm$, $\bar{4}2m$, $4/mmm$, 622, $6mm$, $\bar{6}m2$, $6/mmm$, $\infty 2$, ∞m and ∞/mm [72].

Skab, I., Smaga, I., Savaryn, V., Vasylkiv, Yu., Vlokh, R.: Torsion method for measuring piezooptic coefficients. Cryst. Res. Technol. 2011. 46(1). 23–36. Copyright Wiley-VCH GmbH. Reproduced with permission.

It should be noted that the induced birefringence increment obtained by us in the simulations ($\sim 3.7\times10^{-7}$) is a value that can be determined, e.g., with a standard Senarmont method. However, the most important conclusion from the above consideration is that, in the case of relatively simple (e.g., linear or quadratic) coordinate dependence of the birefringence, its value obtained by the Jones matrix method is the same as the value obtained by averaging the function $\delta(\Delta n)_{ij} = f(x)$. This allows one to use the average of coordinate dependence of the birefringence as a true value. In addition, the piezooptic coefficient π_{44} can be determined using the method described above for the isotropic media, i.e. in the geometry when the light propagates at some angle with respect to the z or y axis and a torsion moment is applied around the z axis.

Now let us consider the possible ways of determining the coefficient π_{66}. For the experimental geometries $(M_x, k \| z)$ or $(M_y, k \| z)$, the dependences of the birefringence on the torsion moment acquire the forms

$$\Delta n_{12} = n_o^3 \pi_{66} \sigma_{12} = n_o^3 \pi_{66} \frac{2M_x}{\pi R^4} z \qquad \text{or} \qquad \Delta n_{12} = n_o^3 \pi_{66} \sigma_{12} = n_o^3 \pi_{66} \frac{2M_y}{\pi R^4} z,$$

respectively. For instance, for the experimental geometry $(M_y, k \| z)$, the total birefringence on the optical path from $+z$ to $-z$ can be defined as the average value of the function

$$\Delta n_{12} = \frac{1}{2\sigma_{12}} n_o^3 \pi_{66} \int_{-\sigma_{12}}^{+\sigma_{12}} \sigma_{12}(z) d\sigma_{12} = \frac{1}{z} n_o^3 \pi_{66} \frac{M_y}{\pi R^4} \int_{-z}^{+z} z dz = 0. \qquad (3.19)$$

As seen from the relation (3.19), the total birefringence is equal to zero. In other words, it is necessary to use some other experimental geometry in order to determine the coefficient π_{66}.

In particular, inclined light incidence with respect to the torsion axis can be used for this purpose. Let the light propagate along the bisector of x and z axes (Fig. 3-2b). Under the action of torsion moment applied around the x axis, the optical indicatrix changes under the influence of the mechanical stress components σ_{12} and σ_{13} and takes the form $B_{11}^0 x^2 + B_{11}^0 y^2 + B_{33}^0 z^2 + 2\pi_{44}\sigma_{13} xz + 2\pi_{66}\sigma_{12} xy = 1$. If one rewrites this relation in the $x'y'z'$ coordinate system, which is rotated relative to the xyz coordinate system by an angle 45 deg around the y axis, it takes the form:

$$\begin{aligned} &\left(0.5(B_{11}^0 + B_{33}^0) + \pi_{44}\sigma_{13}(y)\right) x'^2 + B_{11}^0 y'^2 + \\ &+\left(0.5(B_{11}^0 + B_{33}^0) - \pi_{44}\sigma_{13}(y)\right) z'^2 - \\ &-\sqrt{2}\pi_{66}\sigma_{12}(z) z'y' + (B_{33}^0 - B_{11}^0) x'z' + \\ &+\sqrt{2}\pi_{66}\sigma_{12}(z) x'y' = 1. \end{aligned} \qquad (3.20)$$

The cross-section of the ellipsoid (3.20) by the plane $x' = 0$ orthogonal to the direction of light propagation gives the following equation of the ellipse:

$$B_{11}^0 y'^2 + \left(\frac{1}{2}(B_{11}^0 + B_{33}^0) - \pi_{44}\sigma_{13}(y)\right) z'^2 - \sqrt{2}\pi_{66}\sigma_{12}(z) z'y' = 1. \qquad (3.21)$$

From equation (3.21), the eigenvalues of the refractive indices can be obtained:

$$
\begin{aligned}
n_{2'} &= n_o - \frac{1}{2} n_o^3 \frac{n_o^2 n_e^2 \pi_{66}^2 \sigma_{12}^2(z)}{n_e^2 - n_o^2 + 2 n_o^2 n_e^2 \pi_{44} \sigma_{13}(y)}, \\
n_{3'} &= \frac{n_o n_e \sqrt{2}}{\sqrt{n_o^2 + n_e^2}} + \frac{1}{2} \left(\frac{n_o n_e \sqrt{2}}{\sqrt{n_o^2 + n_e^2}} \right)^3 \times \\
&\times \left(\pi_{44} \sigma_{13}(y) + \frac{n_o^2 n_e^2 \pi_{66}^2 \sigma_{12}^2(z)}{n_e^2 - n_o^2 + 2 n_o^2 n_e^2 \pi_{44} \sigma_{13}(y)} \right).
\end{aligned}
\tag{3.22}
$$

Then, from the relations (3.21) and (3.22), the induced birefringence increment is obtained as

$$
\begin{aligned}
\delta(\Delta n)_{2'3'} &= \frac{1}{2} \left(\frac{n_o n_e \sqrt{2}}{\sqrt{n_o^2 + n_e^2}} \right)^3 \pi_{44} \sigma_{13}(y) + \\
&+ \frac{1}{2} \left(n_o^3 + \left(\frac{n_o n_e \sqrt{2}}{\sqrt{n_o^2 + n_e^2}} \right)^3 \right) \frac{n_o^2 n_e^2 \pi_{66}^2 \sigma_{12}^2(z)}{n_e^2 - n_o^2 + n_o^2 n_e^2 2 \pi_{44} \sigma_{13}(y)} = \\
&= \left(\frac{n_o n_e \sqrt{2}}{\sqrt{n_o^2 + n_e^2}} \right)^3 \pi_{44} \frac{M_x}{\pi R^4} y + \\
&+ \left(n_o^3 + \left(\frac{n_o n_e \sqrt{2}}{\sqrt{n_o^2 + n_e^2}} \right)^3 \right) \frac{2 n_o^2 n_e^2 \pi_{66}^2 \frac{M_x^2}{\pi^2 R^8} z^2}{n_e^2 - n_o^2 + 4 n_o^2 n_e^2 \pi_{44} \frac{M_x}{\pi R^4} y}.
\end{aligned}
\tag{3.23}
$$

The rotation angle of optical indicatrix is given by

$$\tan 2\zeta_{x'} = \frac{2\sqrt{2}n_o^2 n_e^2 \pi_{66}\sigma_{12}(z)}{n_e^2 - n_o^2 + 2n_o^2 n_e^2 \pi_{44}\sigma_{13}(y)} = \\ = \frac{4\sqrt{2}n_o^2 n_e^2 \pi_{66}\dfrac{M_x}{\pi R^4} z}{n_e^2 - n_o^2 + 4n_o^2 n_e^2 \pi_{44}\dfrac{M_x}{\pi R^4} y}. \tag{3.24}$$

Formulae (3.23) and (3.24) can easily be simplified for the case of light propagation in the $x'z'$ plane ($y' = y = 0$):

$$\delta(\Delta n)_{2'3'} = 2\left(n_o^3 + \left(\frac{n_o n_e \sqrt{2}}{\sqrt{n_o^2 + n_e^2}} \right)^3 \right) \frac{n_o^2 n_e^2 \pi_{66}^2 \dfrac{M_x^2}{\pi^2 R^8} z^2}{n_e^2 - n_o^2}, \tag{3.25}$$

$$\tan 2\zeta_{x'} = \frac{4\sqrt{2}n_o^2 n_e^2 \pi_{66}\dfrac{M_x}{\pi R^4} z}{n_e^2 - n_o^2}. \tag{3.26}$$

Then the total value of the birefringence at the light propagation from $+z$ to $-z$ is determined by the averaged function

$$\delta(\Delta n)_{2'3'} = \frac{1}{Z} \frac{n_o^2 n_e^2 \pi_{66}^2 \dfrac{M_x^2}{\pi^2 R^8}}{n_e^2 - n_o^2} \left(n_o^3 + \left(\frac{n_o n_e \sqrt{2}}{\sqrt{n_o^2 + n_e^2}} \right)^3 \right) \int_{-z}^{+z} z^2 dz = \\ = \frac{2n_o^2 n_e^2 \pi_{66}^2 \dfrac{M_x^2}{\pi^2 R^8}}{3(n_e^2 - n_o^2)} \left(n_o^3 + \left(\frac{n_o n_e \sqrt{2}}{\sqrt{n_o^2 + n_e^2}} \right)^3 \right) z^2 = \\ = \frac{2n_o^2 n_e^2 \pi_{66}^2 M_x^2}{3(n_e^2 - n_o^2)\pi^2 R^6} \left(n_o^3 + \left(\frac{n_o n_e \sqrt{2}}{\sqrt{n_o^2 + n_e^2}} \right)^3 \right), \tag{3.27}$$

which is simplified to

$$\delta(\Delta n)_{2'3'} = \frac{2\bar{n}^6 \pi_{66}^2 M_x^2}{3\Delta n \pi^2 R^6} \tag{3.28}$$

under the conditions $n_o \approx n_e = \bar{n}$ and $n_o - n_e = \Delta n$. Using equation (3.28) and the data for the dependence of induced birefringence increment on the torsion moment, one can determine the corresponding piezooptic coefficient:

$$\pi_{66} = \frac{\pi R^3}{\bar{n}^3 M_x} \sqrt{\frac{3}{2} \Delta n \, \delta(\Delta n)_{2'3'}}. \tag{3.29}$$

Note that we have the equality $\pi_{66} = \pi_{11} - \pi_{12}$ for the crystals belonging to the point symmetry groups 622, $6mm$, $\bar{6}m2$, $6/mmm$, $\infty 2$, ∞m, ∞/mm, whereas the last two coefficients can be determined, e.g., using the four-point bending method [65].

3.1.3. Crystals and textures of point symmetry groups 6, $\bar{6}$, $6/m$, ∞ and ∞/m

The piezooptic tensor (1.10) for this type of media is characterized by the presence of four independent coefficients (π_{44}, π_{45}, π_{62}, $\pi_{66} = \pi_{11} - \pi_{12}$), which describe the change in the refractive indices arising under influence of shear stresses:

$$\pi_{\lambda\mu} = \begin{bmatrix} \pi_{11} & \pi_{12} & \pi_{13} & 0 & 0 & 2\pi_{62} \\ \pi_{12} & \pi_{11} & \pi_{13} & 0 & 0 & -2\pi_{62} \\ \pi_{31} & \pi_{31} & \pi_{33} & 0 & 0 & 0 \\ 0 & 0 & 0 & \pi_{44} & \pi_{45} & 0 \\ 0 & 0 & 0 & -\pi_{45} & \pi_{44} & 0 \\ -\pi_{62} & \pi_{62} & 0 & 0 & 0 & \pi_{66} \end{bmatrix}. \tag{3.30}$$

The piezooptic coefficient π_{62} can be determined, e.g., with the following experimental geometries: $(M_x, k \| x)$, $(M_x, k \| y)$, $(M_y, k \| x)$ or $(M_y, k \| y)$ [72].

Let the additional condition $y = 0$ be imposed (Fig. 3-3a). In the case of experimental geometry $(M_x, k \| x)$, the induced birefringence increment can be written as

$$\delta(\Delta n)_{23} = n_o^3 \pi_{62} \sigma_{12}(z) = 2 n_o^3 \pi_{62} \frac{M_x}{\pi R^4} z. \tag{3.31}$$

Then we obtain

$$\pi_{62} = \frac{\delta(\Delta n)_{23}}{n_o^3 \sigma_{12}(z)} = \frac{\delta(\Delta n)_{23} \pi R^4}{2 n_o^3 M_x z} \tag{3.32}$$

for the piezooptic coefficient π_{62}. The relation (3.32) allows one to measure the coefficient π_{62} in the experimental geometry $(M_x, k \| x)$.

When we have the condition $z = 0$ (Fig. 3-3b), the induced birefringence becomes as follows:

$$\begin{aligned} \delta(\Delta n)_{23} &= \frac{1}{2}(n_o^3 + n_e^3) \frac{n_o^2 n_e^2 \pi_{45}^2 \sigma_{13}^2(y)}{n_o^2 - n_e^2} = \\ &= 2(n_o^3 + n_e^3) \frac{n_o^2 n_e^2 \pi_{45}^2 M_x^2 y^2}{(n_o^2 - n_e^2) \pi^2 R^8}. \end{aligned} \tag{3.33}$$

Assuming that $n_o \approx n_e = \bar{n}$ and $n_o - n_e = \Delta n$, equation (3.33) is simplified to the form

$$\delta(\Delta n)_{23} = \frac{\bar{n}^6 \pi_{45}^2 \sigma_{13}^2(y)}{2 \Delta n} = 2 \bar{n}^6 \frac{\pi_{45}^2 M_x^2 y^2}{\Delta n \pi^2 R^8}, \tag{3.34}$$

and the piezooptic coefficient π_{45} is given by the relation

$$\pi_{45} = \frac{\sqrt{2\Delta n\,\delta(\Delta n)_{23}}}{\bar{n}^3\sigma_{13}(y)} = \frac{\pi R^4}{\bar{n}^3 M_x y}\sqrt{\frac{1}{2}\Delta n\,\delta(\Delta n)_{23}}\,. \tag{3.35}$$

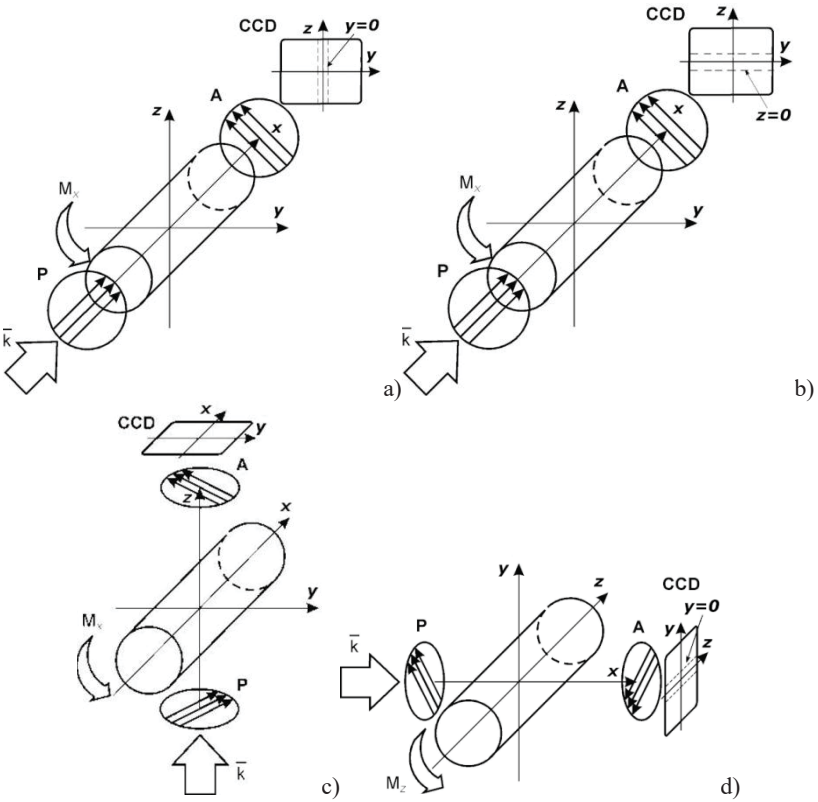

Fig. 3-3. Experimental geometries for measuring piezooptic coefficients π_{62} (a), π_{45} (b), π_{66} (c) and π_{44} (d) in the crystals and textures belonging to the point symmetry groups 6, $\bar{6}$, $6/m$, ∞ and ∞/m [72].
Skab, I., Smaga, I., Savaryn, V., Vasylkiv, Yu., Vlokh, R.: Torsion method for measuring piezooptic coefficients. Cryst. Res. Technol. 2011. 46(1). 23–36. Copyright Wiley-VCH GmbH. Reproduced with permission.

At the same time, the induced birefringence increment, which is determined by equation (3.34), has the value $\sim 5\times10^{-7}$ with the same initial simulation parameters.

Instead, the piezooptic coefficient π_{66} can be determined by examining the induced rotation angle of optical indicatrix ζ_z about the z axis, provided that the coefficient π_{62} is already known. In this case, one arrives at the result $\pi_{66} = 2\pi_{62} \tan 2\zeta_z$ in the experimental geometries $(M_x, k \| z)$ or $(M_y, k \| z)$ (see Fig. 3-3c).

The piezooptic coefficient π_{44} can be determined using the experimental geometry $(M_z, k \| x)$ under the condition $y = 0$ (Fig. 3-3d). In this case, the induced birefringence increment is equal to

$$\begin{aligned} \delta(\Delta n)_{23} &= \frac{1}{2}(n_o^3 + n_e^3)\frac{n_o^2 n_e^2 \pi_{44}^2 \sigma_{23}^2(x)}{n_o^2 - n_e^2} = \\ &= 2(n_o^3 + n_e^3)\frac{n_o^2 n_e^2 \pi_{44}^2 M_z^2 x^2}{(n_o^2 - n_e^2)\pi^2 R^8}. \end{aligned} \tag{3.36}$$

Using the approximation $n_o \approx n_e = \bar{n}$ and $n_o - n_e = \Delta n$, one can rewrite the relation (3.36) as

$$\delta(\Delta n)_{23} = \frac{\bar{n}^6 \pi_{44}^2 \sigma_{23}^2(x)}{2\Delta n} = \frac{2\bar{n}^6 \pi_{44}^2 M_z^2 x^2}{\Delta n \pi^2 R^8}. \tag{3.37}$$

Then the function (3.37) average over the optical path from $x = -R$ to $x = R$ amounts to

$$\delta(\Delta n)_{23} = \frac{1}{R}\frac{\bar{n}^6 \pi_{44}^2 M_z^2}{\Delta n \pi^2 R^8}\int_{-R}^{R} x^2 dx = \frac{2}{3}\frac{\bar{n}^6 \pi_{44}^2 M_z^2}{\Delta n \pi^2 R^6}, \tag{3.38}$$

and the piezooptic coefficient π_{44} is determined by the relation

$$\pi_{44} = \frac{\pi R^3}{\bar{n}^3 M_z}\sqrt{\frac{3}{2}\Delta n\, \delta(\Delta n)_{23}}. \tag{3.39}$$

Hence, all of the non-principal piezooptic coefficients for the hexagonal point symmetry groups can be determined experimentally with the torsion-optic method.

3.1.4. Crystals of point symmetry groups 4, $\bar{4}$ and $4/m$

The piezooptic tensor (1.10) of the crystals belonging to the point symmetry groups 4, $\bar{4}$ and $4/m$ contains four independent piezooptic coefficients, which are associated with the shear stresses: π_{44}, π_{45}, π_{66} and π_{16}.

The coefficient π_{16} can be measured using the experimental geometry $(M_x, k \| x)$ under the condition $y = 0$ (Fig. 3-4a). The induced birefringence increment is described by the relation [73]:

$$\delta(\Delta n)_{23} = \frac{n_o^3}{2}\pi_{16}\sigma_{12}(z) = n_o^3\pi_{16}\frac{M_x}{\pi R^4}z. \tag{3.40}$$

It follows from equation (3.40) that the piezooptic coefficient π_{16} can be determined by scanning the optical beam along the z axis and gathering the appropriate experimental data. The corresponding formula is as follows:

$$\pi_{16} = \frac{2\delta(\Delta n)_{23}}{n_o^3\sigma_{12}(z)} = \frac{\pi R^4\delta(\Delta n)_{23}}{n_o^3 M_x z}. \tag{3.41}$$

The coefficient π_{45} can be measured using the experimental geometry $(M_x, k \| x)$ under the condition $z = 0$ (Fig. 3-4a). In the approximations $n_o \approx n_e = \bar{n}$ and $n_o - n_e = \Delta n$ the induced birefringence increment is described as

$$\begin{aligned}\delta(\Delta n)_{23} &= \frac{1}{2}(n_o^3 + n_e^3)\frac{n_o^2 n_e^2 \pi_{45}^2 \sigma_{13}^2(y)}{n_o^2 - n_e^2} = \\ &= 2(n_o^3 + n_e^3)\frac{n_o^2 n_e^2 \pi_{45}^2 M_x^2 y^2}{(n_o^2 - n_e^2)\pi^2 R^8} \approx 2\frac{\bar{n}^6 \pi_{45}^2 M_x^2 y^2}{\pi^2 R^8 \Delta n}.\end{aligned} \tag{3.42}$$

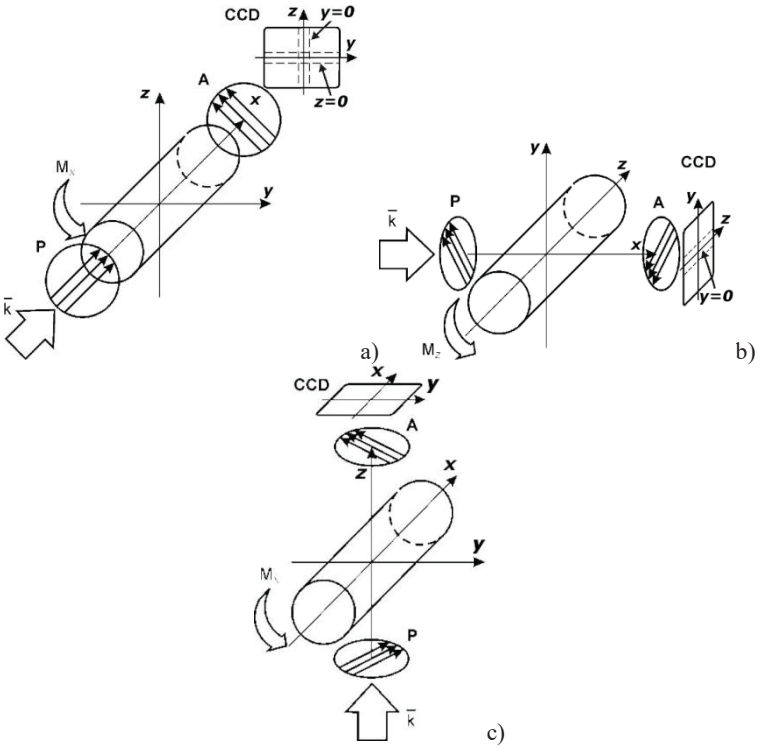

Fig. 3-4. Experimental geometries for measuring piezooptic coefficients π_{16}, π_{45} (a), π_{44} (b) and π_{66} (c) in the crystals belonging to the point groups of symmetry 4, $\bar{4}$ and $4/m$ [72].

Skab, I., Smaga, I., Savaryn, V., Vasylkiv, Yu., Vlokh, R.: Torsion method for measuring piezooptic coefficients. Cryst. Res. Technol. 2011. 46(1). 23–36. Copyright Wiley-VCH GmbH. Reproduced with permission.

The relation (3.42) makes it possible to determine the piezooptic coefficient π_{45}, when we scan the optical beam along the y axis:

$$\pi_{45} = \frac{\sqrt{2\Delta n\, \delta(\Delta n)_{23}}}{\bar{n}^3 \sigma_{13}(y)} = \frac{\pi R^4}{\bar{n}^3 M_x y} \sqrt{\frac{1}{2} \Delta n\, \delta(\Delta n)_{23}}. \qquad (3.43)$$

The coefficient π_{44} can be measured using the experimental geometry $(M_z, k \| x)$ and scanning the optical beam along the z axis under the

condition $y = 0$ (Fig. 3-4b). The induced birefringence increment is equal to

$$\delta(\Delta n)_{23} = \frac{1}{2}(n_o^3 + n_e^3)\frac{n_o^2 n_e^2 \pi_{44}^2 \sigma_{23}^2(x)}{n_o^2 - n_e^2} = 2(n_o^3 + n_e^3)\frac{n_o^2 n_e^2 \pi_{44}^2 M_z^2 x^2}{(n_o^2 - n_e^2)\pi^2 R^8}. \quad (3.44)$$

By averaging the function (3.44) over the optical path from $-x$ to x, one obtains

$$\delta(\Delta n)_{23} = \frac{1}{x}(n_o^3 + n_e^3)\frac{n_o^2 n_e^2 \pi_{44}^2 M_z^2}{(n_o^2 - n_e^2)\pi^2 R^8}\int_{-x}^{+x} x^2 dx = \\ = \frac{2}{3}(n_o^3 + n_e^3)\frac{n_o^2 n_e^2 \pi_{44}^2 M_z^2}{(n_o^2 - n_e^2)\pi^2 R^8} x^2. \quad (3.45)$$

In particular, under the conditions $x = R$, $n_o \approx n_e = \overline{n}$ and $n_o - n_e = \Delta n$, the relation (3.45) takes the form

$$\delta(\Delta n)_{23} = \frac{2}{3}\frac{n_o^2 n_e^2 (n_o^3 + n_e^3)}{n_o^2 - n_e^2}\pi_{44}^2 \frac{M_z^2}{\pi^2 R^6} \approx \frac{2}{3}\frac{\overline{n}^6}{\Delta n}\pi_{44}^2 \frac{M_z^2}{\pi^2 R^6}, \quad (3.46)$$

and the piezooptic coefficient π_{44} is determined by the relation

$$\pi_{44} = \frac{\pi R^3}{\overline{n}^3 M_z}\sqrt{\frac{3}{2}\Delta n\, \delta(\Delta n)_{23}}. \quad (3.47)$$

Finally, the piezooptic coefficient π_{66} can be determined by measuring the induced rotation angle of optical indicatrix ζ_z in the experimental geometry $(M_x, k \| z)$ or $(M_y, k \| z)$ (Fig. 3-4c), provided that the piezooptic coefficient π_{16} is already known. In this case we have $\pi_{66} = \pi_{16} \tan 2\zeta_z$.

Summarizing, one can determine all of the non-principal piezooptic coefficients associated with the shear stresses for the crystals of point symmetry groups 4, $\overline{4}$ and $4/m$, using the torsion-optical method.

3.1.5. Crystals of point symmetry groups 32, 3*m* and $\bar{3}m$

Let us consider the crystals belonging to the point symmetry groups 32, $3m$ and $\bar{3}m$. Their piezooptic tensor (1.10) contains four independent piezooptic coefficients associated with the shear mechanical stresses: π_{44}, π_{14}, π_{41} and π_{66}.

The coefficient π_{14} can be determined using the experimental geometry $(M_z, k \| z)$ (Fig. 3-5a) and the relation

$$\Delta n_{12} = n_o^3 \pi_{14} \sqrt{\sigma_{23}^2(x) + \sigma_{13}^2(y)} = 2 n_o^3 \pi_{14} \frac{M_z}{\pi R^4} \sqrt{x^2 + y^2}. \qquad (3.48)$$

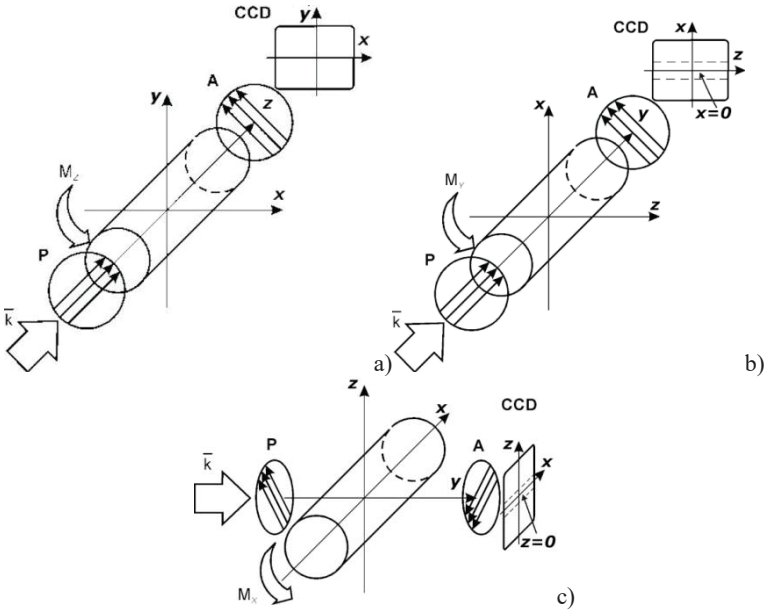

Fig. 3-5. Experimental geometries for measuring piezooptic coefficients π_{14} (a), π_{41} (b) and π_{44} (c) in the crystals belonging to the point symmetry groups 32, $3m$ and $\bar{3}m$ [72].

Skab, I., Smaga, I., Savaryn, V., Vasylkiv, Yu., Vlokh, R.: Torsion method for measuring piezooptic coefficients. Cryst. Res. Technol. 2011. 46(1). 23–36. Copyright Wiley-VCH GmbH. Reproduced with permission.

Then, the coefficient π_{14} can be determined from the xy-coordinate dependence of the induced birefringence on the torsion moment:

$$\pi_{14} = \frac{\Delta n_{12}}{n_o^3 \sqrt{\sigma_{23}^2(x) + \sigma_{13}^2(y)}} = \frac{\pi R^4 \Delta n_{12}}{2 n_o^3 M_z \sqrt{x^2 + y^2}}. \tag{3.49}$$

The coefficient π_{41} can be measured in the experimental geometry $(M_y, k \parallel y)$ (Fig. 3-5b) under the condition $x = 0$. Here the light beam is scanned along the z axis. The relation for the induced birefringence increment is given by the formula

$$\begin{aligned} \delta(\Delta n)_{13} &= 2\left(n_o^3 + n_e^3\right) \frac{n_o^2 n_e^2 \pi_{41}^2 \sigma_{12}^2(z)}{n_o^2 - n_e^2} = \\ &= 8\left(n_o^3 + n_e^3\right) \frac{n_o^2 n_e^2 \pi_{41}^2 M_y^2 z^2}{(n_o^2 - n_e^2)\pi^2 R^8}. \end{aligned} \tag{3.50}$$

Using the approximations $n_o \approx n_e = \bar{n}$ and $n_o - n_e = \Delta n$, one can rewrite formula (3.50) as

$$\delta(\Delta n)_{13} \approx \frac{8\bar{n}^6}{\Delta n} \pi_{41}^2 \frac{M_y^2}{\pi^2 R^8} z^2. \tag{3.51}$$

From equations (3.50) and (3.51), one can obtain the expression for determining the coefficient π_{41}:

$$\pi_{41} = \frac{\pi R^4}{2 n_o n_e M_y z} \sqrt{\frac{(n_o^2 - n_e^2)}{2\left(n_o^3 + n_e^3\right)} \delta(\Delta n)_{13}} \approx \frac{\pi R^4}{2\bar{n}^3 M_y z} \sqrt{\frac{1}{2} \Delta n \, \delta(\Delta n)_{13}}. \tag{3.52}$$

The piezooptic coefficient π_{44} can be determined in the experimental geometry $(M_x, k \parallel y)$, while scanning the light beam along the x axis under the condition $z = 0$ (Fig. 3-5c). Then the induced birefringence increment reads as

$$\delta(\Delta n)_{13} = \frac{1}{2}(n_o^3 + n_e^3)\frac{n_o^2 n_e^2 \pi_{44}^2 \sigma_{13}^2(y)}{n_o^2 - n_e^2} = 2(n_o^3 + n_e^3)\frac{n_o^2 n_e^2 \pi_{44}^2 M_x^2 y^2}{(n_o^2 - n_e^2)\pi^2 R^8}. \tag{3.53}$$

Averaging the function (3.53) over the optical path from $-y$ to y, one obtains

$$\begin{aligned}\delta(\Delta n)_{13} &= \frac{1}{y}(n_o^3 + n_e^3)\frac{n_o^2 n_e^2 \pi_{44}^2 M_x^2}{(n_o^2 - n_e^2)\pi^2 R^8}\int_{-y}^{+y} y^2 dy = \\ &= \frac{2}{3}(n_o^3 + n_e^3)\frac{n_o^2 n_e^2 \pi_{44}^2 M_x^2}{(n_o^2 - n_e^2)\pi^2 R^8}\, y^2.\end{aligned} \tag{3.54}$$

Under the condition $y = R$ and in the approximations $n_o \approx n_e = \overline{n}$ and $n_o - n_e = \Delta n$, the relation (3.54) takes the following form:

$$\delta(\Delta n)_{13} = \frac{2}{3}(n_o^3 + n_e^3)\frac{n_o^2 n_e^2}{n_o^2 - n_e^2}\pi_{44}^2 \frac{M_x^2}{\pi^2 R^6} \approx \frac{2}{3}\frac{\overline{n}^6}{\Delta n}\pi_{44}^2 \frac{M_x^2}{\pi^2 R^6}. \tag{3.55}$$

Now the relation (3.55) yields the following expression for determining the piezooptic coefficient π_{44}:

$$\pi_{44} = \frac{\pi R^3}{n_o n_e M_x}\sqrt{\frac{3(n_o^2 - n_e^2)}{2\left(n_o^3 + n_e^3\right)}\delta(\Delta n)_{13}} \approx \frac{\pi R^3}{\overline{n}^3 M_x}\sqrt{\frac{3}{2}\Delta n\, \delta(\Delta n)_{13}}. \tag{3.56}$$

Finally, we stress that the piezooptic coefficient π_{66} for the crystals belonging to the point symmetry groups 32, $3m$ and $\overline{3}m$ is given by the equality $\pi_{66} = \pi_{11} - \pi_{12}$. It can be measured using the four-point bending method.

3.1.6. Crystals of point symmetry groups 3 and $\overline{3}$

The piezooptic tensor (1.10) for the crystals belonging to the point symmetry groups 3 and $\overline{3}$ has eight independent piezooptic coefficients associated with the shear mechanical stresses: π_{25}, π_{62}, π_{45}, π_{52}, π_{44}, π_{41}, π_{14} and π_{66}.

The piezooptic coefficient π_{25} can be determined when applying the experimental geometry $(M_x, k \| x)$ under additional condition $z = 0$ (Fig. 3-6a). In this case, the relation that describes the induced birefringence increment is as follows:

$$\delta(\Delta n)_{23} \approx \frac{n_o^3}{2}\pi_{25}\sigma_{13}(y) = n_o^3 \frac{M_x}{\pi R^4}\pi_{25} y. \tag{3.57}$$

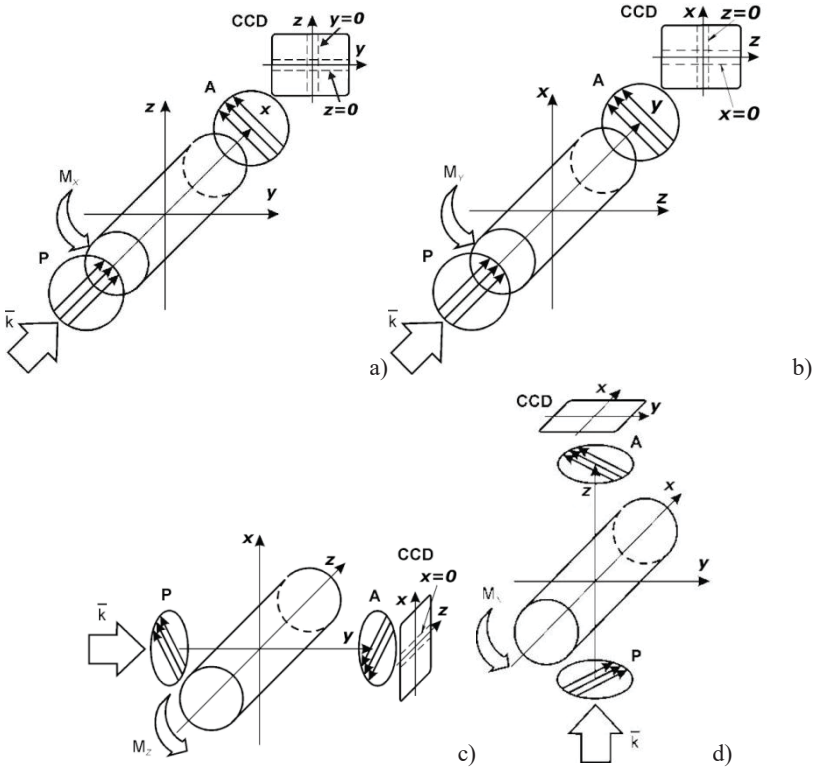

Fig. 3-6. Experimental geometries for measuring piezooptic coefficients π_{25}, π_{62}, π_{45}, π_{52} (a), π_{14}, π_{62}, π_{41} (b), π_{44} (c) and π_{66} (d) for the crystals belonging to the point symmetry groups 3 and $\bar{3}$ [72].

Skab, I., Smaga, I., Savaryn, V., Vasylkiv, Yu., Vlokh, R.: Torsion method for measuring piezooptic coefficients. Cryst. Res. Technol. 2011. 46(1). 23–36. Copyright Wiley-VCH GmbH. Reproduced with permission.

It follows from (3.57) that the piezooptic coefficient π_{25} can be determined by scanning the light beam along the y axis and taking the corresponding experimental data. The formula is as follows:

$$\pi_{25} \approx \frac{2\delta(\Delta n)_{23}}{n_o^3 \sigma_{13}(y)} = \frac{\pi R^4 \delta(\Delta n)_{23}}{n_o^3 M_x y}. \tag{3.58}$$

The piezooptic coefficient π_{62} can be determined when applying the experimental geometry $(M_x, k \| x)$ under the condition $y = 0$ (Fig. 3-6a). The relation describing the induced birefringence increment reads as

$$\delta(\Delta n)_{23} \approx -n_o^3 \pi_{62} \sigma_{12}(z) = -n_o^3 \frac{2M_x}{\pi R^4} \pi_{62} z. \tag{3.59}$$

Formula (3.59) makes it possible to determine the piezooptic coefficient π_{62}, provided that the light beam is scanned along the z axis:

$$\pi_{62} \approx -\frac{\delta(\Delta n)_{23}}{n_o^3 \sigma_{12}(z)} = -\frac{\pi R^4 \delta(\Delta n)_{23}}{2n_o^3 M_x z}. \tag{3.60}$$

The coefficients π_{45} and π_{52} can be determined using the experimental geometry $(M_x, k \| x)$ (Fig. 3-6a) and measuring the rotation angle of optical indicatrix under the action of torsion moment and under the additional conditions $z = 0$ and $y = 0$, respectively. Then the relation describing the optical-indicatrix rotation about the x axis is as follows:

$$\begin{aligned} \tan 2\zeta_x &= \frac{2n_o^2 n_e^2 (\pi_{45}\sigma_{13}(y) + 2\pi_{52}\sigma_{12}(z))}{n_o^2 - n_e^2 - n_o^2 n_e^2 (\pi_{25}\sigma_{13}(y) - 2\pi_{62}\sigma_{12}(z))} = \\ &= \frac{4n_o^2 n_e^2 \frac{M_x}{\pi R^4} (\pi_{45} y + 2\pi_{52} z)}{n_o^2 - n_e^2 - n_o^2 n_e^2 \frac{2M_x}{\pi R^4} (\pi_{25} y - 2\pi_{62} z)}. \end{aligned} \tag{3.61}$$

Since the inequality $n_o^2 - n_e^2 >> n_o^2 n_e^2 (\pi_{25}\sigma_{13}(y) - 2\pi_{62}\sigma_{12}(z))$ is usually valid in practice, equation (3.61) takes the form

$$\tan 2\zeta_x \approx \frac{2n_o^2 n_e^2(\pi_{45}\sigma_{13}(y)+2\pi_{52}\sigma_{12}(z))}{n_o^2-n_e^2} = \\ = \frac{4n_o^2 n_e^2 M_x(\pi_{45}y+2\pi_{52}z)}{(n_o^2-n_e^2)\pi R^4}. \tag{3.62}$$

Using the relation (3.62), the coefficient π_{45} (or π_{52}) can be determined if the light beam is scanned along the y axis ($z=0$) (or along the z axis ($y=0$)). In the case of light propagation along optically anisotropic directions, the rotation angle of optical indicatrix is very small, since we have $2n_o^2 n_e^2(\pi_{45}\sigma_{13}(y)+2\pi_{52}\sigma_{12}(z)) << n_o^2-n_e^2$.

The piezooptic coefficient π_{14} can be determined using the experimental geometry $(M_y, k \| y)$ and applying the additional condition $z=0$ (Fig. 3-6b). Then the relation for the induced birefringence increment is given by

$$\delta(\Delta n)_{13} \approx \frac{1}{2} n_o^3 \pi_{14}\sigma_{23}(x) = n_o^3 \frac{M_y}{\pi R^4}\pi_{14}x. \tag{3.63}$$

It follows from (3.63) that the piezooptic coefficient π_{14} can be determined by scanning the light beam along the x axis and taking the corresponding experimental data. The appropriate formula is as follows:

$$\pi_{14} \approx \frac{2\delta(\Delta n)_{13}}{n_o^3\sigma_{23}(x)} = \frac{\pi R^4 \delta(\Delta n)_{13}}{n_o^3 M_y x}. \tag{3.64}$$

In its turn, the piezooptic coefficient π_{62} can be determined when applying the experimental geometry $(M_y, k \| y)$ and the additional condition $x=0$ (Fig. 3-6b). In this case, the relation describing the induced birefringence increment takes the form

$$\delta(\Delta n)_{13} \approx n_o^3 \pi_{62}\sigma_{12}(z) = n_o^3 \frac{2M_y}{\pi R^4}\pi_{62}z. \tag{3.65}$$

It follows from (3.65) that the piezooptic coefficient π_{62} can be determined by scanning the light beam along the z axis and taking the corresponding experimental data. The formula is as follows:

$$\pi_{62} \approx \frac{\delta(\Delta n)_{13}}{n_o^3 \sigma_{12}(z)} = \frac{\pi R^4 \delta(\Delta n)_{13}}{2 n_o^3 M_y z}. \tag{3.66}$$

Instead, the coefficient π_{41} can be determined while using the experimental geometry $(M_y, k \| y)$ (Fig. 3-6b) and measuring the rotation angle of optical indicatrix at the torsion moment M_y under the additional condition $x = 0$. Then the optical-indicatrix rotation about the y axis is given by the formula

$$\tan 2\zeta_y \approx \frac{4 n_o^2 n_e^2 \pi_{41} \sigma_{12}(z)}{n_o^2 - n_e^2} = \frac{8 n_o^2 n_e^2 M_y \pi_{41} z}{(n_o^2 - n_e^2)\pi R^4}. \tag{3.67}$$

Using (3.67) and scanning the light beam along the z axis ($x = 0$), one can determine the coefficient π_{41}.

The coefficient π_{44} can be found, in some approximation, in the experimental geometries $(M_x, k \| y)$ at $z = 0$, $(M_y, k \| x)$ at $z = 0$, $(M_z, k \| x)$ at $y = 0$ or $(M_z, k \| y)$ at $x = 0$. In particular, when the condition $x = 0$ and the inequality $n_o^2 - n_e^2 >> n_o^2 n_e^2 (\pi_{14}\sigma_{23}(x) - \pi_{25}\sigma_{13}(y))$ are satisfied, the induced birefringence increment in the experimental geometry $(M_z, k \| y)$ (see Fig. 3-6c) is as follows:

$$\begin{aligned} \delta(\Delta n)_{13} &\approx -\frac{1}{2} n_o^3 \pi_{25} \sigma_{13}(y) - \frac{1}{2}(n_o^3 + n_e^3) \frac{n_o^2 n_e^2 \pi_{44}^2 \sigma_{13}^2(y)}{n_o^2 - n_e^2} = \\ &= -n_o^3 \frac{M_z}{\pi R^4} \pi_{25} y - 2(n_o^3 + n_e^3) \frac{n_o^2 n_e^2 M_z^2 \pi_{44}^2 y^2}{(n_o^2 - n_e^2)\pi^2 R^8}. \end{aligned} \tag{3.68}$$

By averaging the function given by (3.68) over the optical path from $-y$ to y, one can obtain

$$\delta(\Delta n)_{13} = -\frac{1}{2y} n_o^3 \frac{M_z}{\pi R^4} \pi_{25} \int_{-y}^{+y} y dy - \frac{1}{y} (n_o^3 + n_e^3) \frac{n_o^2 n_e^2 M_z^2 \pi_{44}^2}{(n_o^2 - n_e^2)\pi^2 R^8} \int_{-y}^{+y} y^2 dy = \\ = -\frac{2}{3} (n_o^3 + n_e^3) \frac{n_o^2 n_e^2 M_z^2 \pi_{44}^2}{(n_o^2 - n_e^2)\pi^2 R^8} y^2. \tag{3.69}$$

Under the condition $y = R$ and in the approximations $n_o \approx n_e = \overline{n}$ and $n_o - n_e = \Delta n$, the relation (3.69) takes the following form:

$$\left|\delta(\Delta n)_{13}\right| = \frac{2}{3} (n_o^3 + n_e^3) \frac{n_o^2 n_e^2}{n_o^2 - n_e^2} \pi_{44}^2 \frac{M_z^2}{\pi^2 R^6} \approx \frac{2}{3} \frac{\overline{n}^6}{|\Delta n|} \pi_{44}^2 \frac{M_z^2}{\pi^2 R^6}. \tag{3.70}$$

Using the relation (3.70), one can obtain the expression needed for determining the piezooptic coefficient π_{44}:

$$|\pi_{44}| = \frac{\pi R^3}{n_o n_e M_z} \sqrt{\frac{3(n_o^2 - n_e^2)}{2\left(n_o^3 + n_e^3\right)} \left|\delta(\Delta n)_{13}\right|} \approx \frac{\pi R^3}{\overline{n}^3 M_z} \sqrt{\frac{3}{2} |\Delta n| \left|\delta(\Delta n)_{13}\right|}. \tag{3.71}$$

The piezooptic coefficient π_{66} is determined by measuring the induced rotation of optical indicatrix ζ_z and using the experimental geometries $(M_x, k \| z)$ at $y = 0$ or $(M_y, k \| z)$ at $x = 0$ (Fig. 3-6d), if the coefficient π_{62} is already known. In this case we have $\pi_{66} = 2\pi_{62} \tan 2\zeta_z$. In addition, the piezooptic coefficient π_{66} can be determined by the relation $\pi_{66} = \pi_{11} - \pi_{12}$ or measured by the four-point bending method, in order to verify the validity of data obtained with the torsion-optic method.

3.1.7. Crystals of rhombic, monoclinic and triclinic systems

The crystals of rhombic system with the symmetries 222, *mmm* and *mm*2 are characterized by a presence of three independent piezooptic coefficients associated with the shear mechanical stresses: π_{44}, π_{55} and π_{66}.

These piezooptic coefficients can be measured when the light propagates along the directions perpendicular to the torsion axis ($M_i \perp k_j$). At the same time, the induced birefringence increment depends quadratically on the components of mechanical stress [73] and, therefore, on the squared

coordinates that correspond to the direction of beam propagation ($\delta(\Delta n)_i \sim x_j^2$). As shown above, in order to determine the effective value of the induced birefringence change, it is necessary to average the function $\delta(\Delta n)_i$ along the optical path from $-x_j$ to $+x_j$.

In particular, the coefficient π_{44} can be determined using the experimental geometries $(M_y, k \| x)$ and $(M_z, k \| x)$. At the same time, the functions of the induced birefringence increment averaged over the segment from $x = -R$ to $x = R$ are equal respectively to

$$\delta(\Delta n)_{23} = \frac{1}{R} \frac{n_2^2 n_3^2 (n_2^3 + n_3^3) \pi_{44}^2 M_y^2}{(n_2^2 - n_3^2) \pi^2 R^8} \int_{-R}^{R} x^2 dx = \frac{2}{3} \frac{n_2^2 n_3^2 (n_2^3 + n_3^3) \pi_{44}^2 M_y^2}{(n_2^2 - n_3^2) \pi^2 R^6} \tag{3.72}$$

and

$$\delta(\Delta n)_{23} = \frac{1}{R} \frac{n_2^2 n_3^2 (n_2^3 + n_3^3) \pi_{44}^2 M_z^2}{(n_2^2 - n_3^2) \pi^2 R^8} \int_{-R}^{R} x^2 dx = \frac{2}{3} \frac{n_2^2 n_3^2 (n_2^3 + n_3^3) \pi_{44}^2 M_z^2}{(n_2^2 - n_3^2) \pi^2 R^6}. \tag{3.73}$$

The following expressions can be obtained for determining the piezooptic coefficient π_{44} from the relations (3.72) and (3.73):

$$\begin{aligned} \pi_{44} &= \frac{\pi R^3}{n_2 n_3 M_y} \sqrt{\frac{3(n_2^2 - n_3^2)}{2(n_2^3 + n_3^3)} \delta(\Delta n)_{23}}, \\ \pi_{44} &= \frac{\pi R^3}{n_2 n_3 M_z} \sqrt{\frac{3(n_2^2 - n_3^2)}{2(n_2^3 + n_3^3)} \delta(\Delta n)_{23}}. \end{aligned} \tag{3.74}$$

Similarly, the expressions for determining the piezooptic coefficients π_{55} and π_{66} can be obtained respectively for the experimental geometries $(M_x, k \parallel y)$ and $(M_z, k \parallel y)$ (with averaging performed over the segment from $y = -R$ to $y = R$) and in the experimental geometries $(M_x, k \parallel z)$ and $(M_y, k \parallel z)$ (with averaging over the segment from $z = -R$ to $z = R$):

$$\pi_{55} = \frac{\pi R^3}{n_1 n_3 M_x}\sqrt{\frac{3(n_1^2 - n_3^2)}{2(n_1^3 + n_3^3)}\delta(\Delta n)_{13}}, \qquad \pi_{55} = \frac{\pi R^3}{n_1 n_3 M_z}\sqrt{\frac{3(n_1^2 - n_3^2)}{2(n_1^3 + n_3^3)}\delta(\Delta n)_{13}}, \tag{3.75}$$

$$\pi_{66} = \frac{\pi R^3}{n_1 n_2 M_x}\sqrt{\frac{3(n_1^2 - n_2^2)}{2(n_1^3 + n_2^3)}\delta(\Delta n)_{12}}, \qquad \pi_{66} = \frac{\pi R^3}{n_1 n_2 M_y}\sqrt{\frac{3(n_1^2 - n_2^2)}{2(n_1^3 + n_2^3)}\delta(\Delta n)_{12}}. \tag{3.76}$$

Thus, all of the non-principal piezooptic coefficients can be determined for the crystals of rhombic system, using the torsion-optic method.

The crystals belonging to the monoclinic system (with the point symmetry groups 2, m and $2/m$) are characterized by eight independent piezooptic coefficients associated with the shear mechanical stresses: π_{44}, π_{55}, π_{66}, π_{15}, π_{25}, π_{35}, π_{46} and π_{64}.

The piezooptic coefficient π_{64} can be measured in the experimental geometry $(M_z, k \parallel z)$ under the condition $y = 0$. Here the optical beam is scanned along the x axis (Fig. 3-7a). The induced birefringence increment has the following form:

$$\delta(\Delta n)_{12} = \frac{1}{2}(n_1^3 + n_2^3)\frac{n_1^2 n_2^2 \pi_{64}^2 \sigma_{23}^2(x)}{n_1^2 - n_2^2} = 2(n_1^3 + n_2^3)\frac{n_1^2 n_2^2 \pi_{64}^2 M_z^2 x^2}{(n_1^2 - n_2^2)\pi^2 R^8}. \tag{3.77}$$

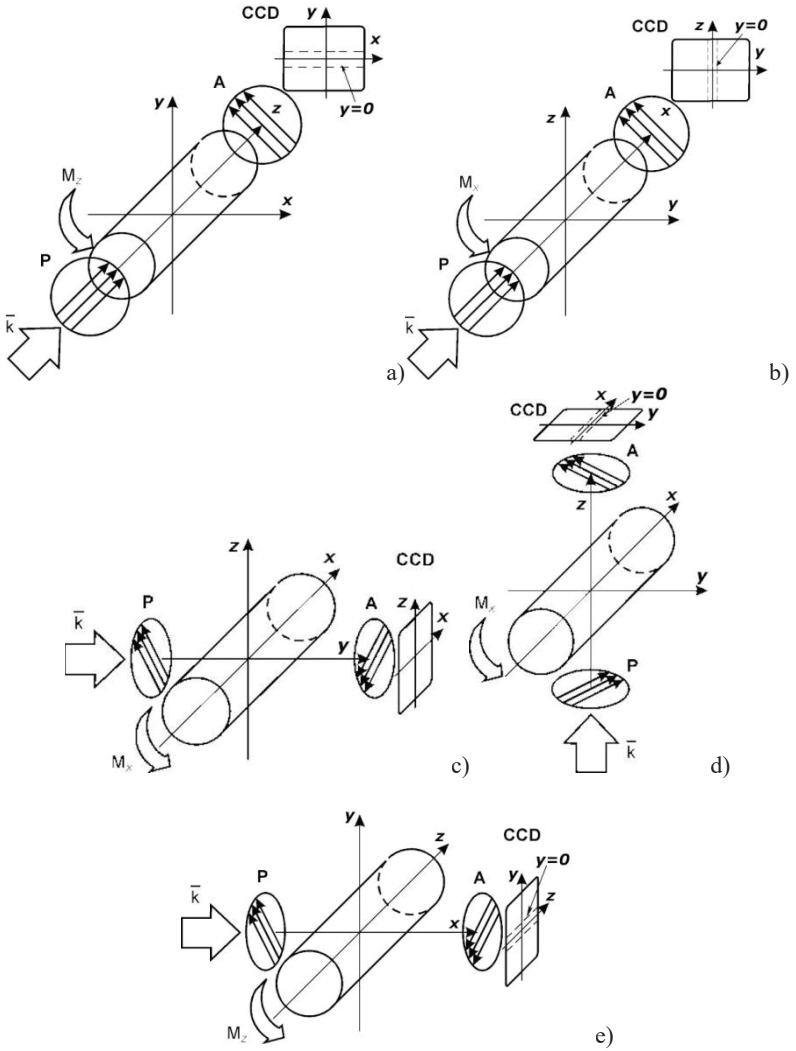

Fig. 3-7. Experimental geometries used for measuring piezooptic coefficients π_{64} (a), π_{46} (b), π_{55} (c), π_{66} (d) and π_{44} (e) in the crystals belonging to monoclinic system [72].

Skab, I., Smaga, I., Savaryn, V., Vasylkiv, Yu., Vlokh, R.: Torsion method for measuring piezooptic coefficients. Cryst. Res. Technol. 2011. 46(1). 23–36. Copyright Wiley-VCH GmbH. Reproduced with permission.

Another expression for determining the piezooptic coefficient π_{64} can be obtained from equation (3.77):

$$\pi_{64} = \frac{1}{n_1 n_2 \sigma_{23}(x)} \sqrt{\frac{2(n_1^2 - n_2^2)\delta(\Delta n)_{12}}{(n_1^3 + n_2^3)}} = \\ = \frac{\pi R^4}{n_1 n_2 M_z x} \sqrt{\frac{(n_1^2 - n_2^2)\delta(\Delta n)_{12}}{2(n_1^3 + n_2^3)}}. \tag{3.78}$$

The piezooptic coefficient π_{46} can be determined in a similar way. This requires the experimental geometry $(M_x, k \| x)$, the condition $y = 0$ and scanning of the light beam along the z axis (Fig. 3-7b). In this case we have

$$\delta(\Delta n)_{23} = \frac{1}{2}(n_2^3 + n_3^3)\frac{n_2^2 n_3^2 \pi_{46}^2 \sigma_{12}^2(z)}{n_2^2 - n_3^2} = \\ = 2(n_2^3 + n_3^3)\frac{n_2^2 n_3^2 \pi_{46}^2 M_x^2 z^2}{(n_2^2 - n_3^2)\pi^2 R^8}, \tag{3.79}$$

$$\pi_{46} = \frac{1}{n_2 n_3 \sigma_{12}(z)} \sqrt{\frac{2(n_2^2 - n_3^2)\delta(\Delta n)_{23}}{(n_2^3 + n_3^3)}} = \\ = \frac{\pi R^4}{n_2 n_3 M_x z} \sqrt{\frac{(n_2^2 - n_3^2)\delta(\Delta n)_{23}}{2(n_2^3 + n_3^3)}}. \tag{3.80}$$

To determine the piezooptic coefficient π_{55}, the experimental geometry $(M_x, k \| y)$ can be adopted under the condition $z = 0$. The birefringence increment must be averaged over the optical path section $-R \le y \le R$ (Fig. 3-7c). Then we obtain

$$\delta(\Delta n)_{13} \approx \frac{1}{R}(n_1^3 + n_3^3)\frac{n_1^2 n_3^2 \pi_{55}^2 M_x^2}{(n_1^2 - n_3^2)\pi^2 R^8} \int_{-R}^{R} y^2 dy = \\ = \frac{2}{3}(n_1^3 + n_3^3)\frac{n_1^2 n_3^2 \pi_{55}^2 M_x^2}{(n_1^2 - n_3^2)\pi^2 R^6}, \tag{3.81}$$

$$\pi_{55} = \frac{\pi R^3}{n_1 n_3 M_x} \sqrt{\frac{3(n_1^2 - n_3^2)}{2(n_1^3 + n_3^3)} \delta(\Delta n)_{13}}. \tag{3.82}$$

To determine the piezooptic coefficient π_{66}, the experimental geometry $(M_x, k \| z)$ is needed, under the condition $y = 0$ satisfied. Then the birefringence increment has to be averaged over the optical path section $-R \le z \le R$ (Fig. 3-7d). The corresponding phenomenological relation is as follows:

$$\begin{aligned} \delta(\Delta n)_{12} &= \frac{1}{R}(n_2^3 + n_1^3) \frac{n_1^2 n_2^2 \pi_{66}^2 M_x^2}{(n_2^2 - n_1^2)\pi^2 R^8} \int_{-R}^{+R} z^2 dz = \\ &= \frac{2}{3}(n_2^3 + n_1^3) \frac{n_1^2 n_2^2 \pi_{66}^2 M_x^2}{(n_2^2 - n_1^2)\pi^2 R^6}, \end{aligned} \tag{3.83}$$

$$\pi_{66} = \frac{\pi R^3}{n_1 n_2 M_x} \sqrt{\frac{3(n_2^2 - n_1^2)}{2(n_2^3 + n_1^3)} \delta(\Delta n)_{12}}. \tag{3.84}$$

Finally, in order to determine the piezooptic coefficient π_{44}, the experimental geometry $(M_z, k \| x)$ should be used under the condition $y = 0$, with averaging the birefringence increment over the optical path section $-R \le x \le R$ (see Fig. 3-7e). In this case we have

$$\begin{aligned} \delta(\Delta n)_{23} &= \frac{1}{R}(n_2^3 + n_3^3) \frac{n_2^2 n_3^2 \pi_{44}^2 M_z^2}{(n_2^2 - n_3^2)\pi^2 R^8} \int_{-R}^{+R} x^2 dx = \\ &= \frac{2}{3}(n_2^3 + n_3^3) \frac{n_2^2 n_3^2 \pi_{44}^2 M_z^2}{(n_2^2 - n_3^2)\pi^2 R^6}, \end{aligned} \tag{3.85}$$

$$\pi_{44} = \frac{\pi R^3}{n_2 n_3 M_z} \sqrt{\frac{3(n_2^2 - n_3^2)}{2(n_2^3 + n_3^3)} \delta(\Delta n)_{23}}. \tag{3.86}$$

Concerning the remaining three piezooptic coefficients of the monoclinic crystals (namely, π_{15}, π_{25} and π_{35}), the torsion-optic method enables one to determine only their differences. For example, the piezooptic difference $n_2^3 \pi_{25} - n_1^3 \pi_{15}$ can be determined by measuring the torsion-induced birefringence increment $\delta(\Delta n)_{12}$ with the experimental geometry

$(M_z, k \| z)$ under the condition $x = 0$. Similarly, the difference $n_3^3\pi_{35} - n_2^3\pi_{25}$ can be measured using the experimental geometry $(M_x, k \| x)$ under the condition $z = 0$.

The same analysis can be applied to the crystals that belong to triclinic system. However, the piezooptic effect can also be studied using the interferometric method. The latter allows for measuring the increments of refractive indices. As a consequence, individual piezooptic coefficients for the monoclinic and triclinic crystals can, in principle, be determined by combining the experimental data obtained using the torsion-optic and interferometric methods.

3.2. Determination of piezooptic coefficient π_{14} in lithium niobate crystals

As shown above, the application of torsion loads to crystals, in combination with appropriate polarization measurements, can be used to determine the non-principal piezooptic coefficients associated with the shear mechanical stresses. The advantage of the torsion-optic method over the conventional methods that rely upon compression or stretching loads is that the application of a torsion moment causes only the shear components of the mechanical stress tensor. Therefore, this allows for determining directly and separately some of the coefficients. Besides, the torsion-induced components of the mechanical stress tensor are characterized by specific spatial distributions in crystals, which can be determined in advance.

An experimental verification of the torsion-optic method for measuring the piezooptic coefficients has been carried out, using a particular example of $LiNbO_3$ crystals [72, 75]. They belong to the point symmetry group $3m$.

In our studies, crystalline samples have been made in the shape of octahedral prisms, the side faces of which are parallel to the z axis and the base of which is parallel to the xy plane (Fig. 3-8).

The sizes of the samples are $H \sim 13$ mm along the z axis and $h \sim 6$ mm between the side faces. The yz plane is taken to be parallel to one of the symmetry planes. A He-Ne laser radiation with the wavelength $\lambda = 632.8$ nm propagates along the z axis, which is parallel to the optic axis.

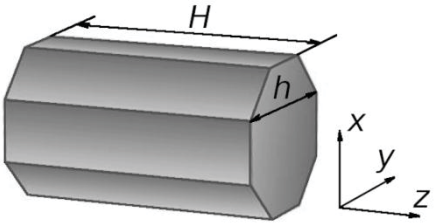

Fig. 3-8. Orientations of principal axes in crystal sample of $LiNbO_3$ [72].
Skab, I., Smaga, I., Savaryn, V., Vasylkiv, Yu., Vlokh, R.: Torsion method for measuring piezooptic coefficients. Cryst. Res. Technol. 2011. 46(1). 23–36. Copyright Wiley-VCH GmbH. Reproduced with permission.

To produce the torsion stresses, a mechanical torsion moment M_z is applied around the z axis to one of the prism bases, while its opposite side is not loaded (Fig. 3-9).

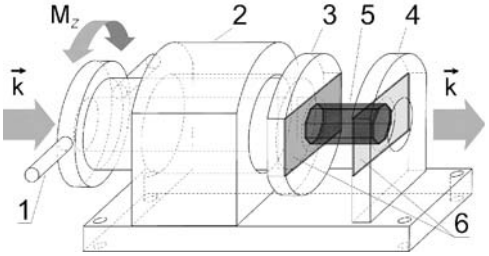

Fig. 3-9. A scheme of application of a torsion moment: (1) arms; (2) massive holder; (3) movable hollow cylinder; (4) massive immovable holder; (5) sample; (6) plates with octahedral holes for the sample set. The arrows show directions of light propagation and twist [72].
Skab, I., Smaga, I., Savaryn, V., Vasylkiv, Yu., Vlokh, R.: Torsion method for measuring piezooptic coefficients. Cryst. Res. Technol. 2011. 46(1). 23–36. Copyright Wiley-VCH GmbH. Reproduced with permission.

Studies of the optical birefringence have been carried out, using an imaging polarimeter [76] and a Senarmont method [77]. The torsion-induced birefringence is calculated with the formula $\Delta n = \beta\lambda / \pi d$, where $\beta = \Delta\Gamma / 2$ denotes the rotation angle of the light polarization plane with respect to its initial orientation (after the light has passed through a $\lambda / 4$-plate), $\Delta\Gamma$ is the phase difference, and d the thickness of sample along the direction of light propagation.

Fig. 3-10 presents spatial distributions of the birefringence, which are induced by the torsion moment $M_z = 63.77 \times 10^{-3}$ N×m along the x and y axes and along the bisector of x and y axes. All the data is derived with the Senarmont method.

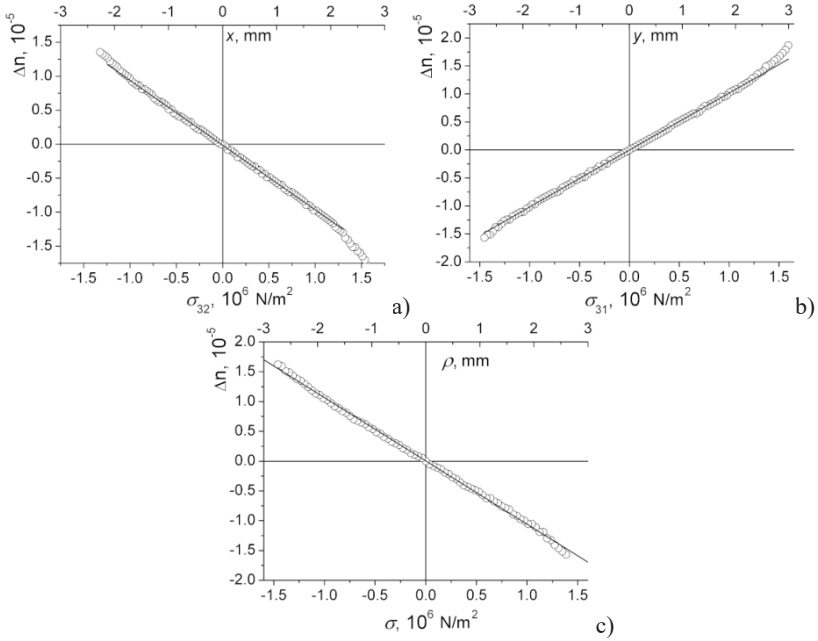

Fig. 3-10. Distributions of birefringence induced by the torsion moment $M_z = 63.77 \times 10^{-3}$ N×m in $LiNbO_3$ along the x axis (a), the y axis (b) and the bisector of x and y axes (c). Open circles correspond to experimental data and solid lines to linear fits. Scales of the corresponding components of shear stresses are also shown [75].

Adapted with permission from Vasylkiv, Yu., Savaryn, V., Smaga, I., Skab, I., Vlokh, R. (2010). Determination of piezooptic coefficient π_{14} of $LiNbO_3$ crystals under torsion loading. Ukr. J. Phys. Opt., 11(3), 156–164. © O. G. Vlokh Institute of Physical Optics.

The dependences mentioned above are linear at the distances less than ~ 2 mm from the torsion axis. For more distant points, some deviations from the linear dependences are observed. They can be explained by the effect of sample boundaries and deviations of sample shape from cylindrical one.

Now let us consider the birefringence induced by the torsion moment M_z. Let the light beam propagate along the z axis. Then we deal with the experimental geometry $(M_z, k \| z)$. The induced birefringence is a function of the shear stresses $\sigma_{32}(x)$ and $\sigma_{31}(y)$. Therefore, it depends on the x and y coordinates. For example, the principal refractive indices and the induced birefringence along the x axis for the case $\sigma_{31} = 0$ and in the plane $y = 0$ (Fig. 3-10a) are determined by the relations

$$\begin{aligned} n_1 &= n_o + \frac{1}{2} n_o^3 \pi_{14} \sigma_{32} = n_o + n_o^3 \pi_{14} \frac{M_z}{\pi R^4} x, \\ n_2 &= n_o - \frac{1}{2} n_o^3 \pi_{14} \sigma_{32} = n_o - n_0^3 \pi_{14} \frac{M_z}{\pi R^4} x, \\ \Delta n_{12} &= n_o^3 \pi_{14} \sigma_{32} = n_o^3 \pi_{14} \frac{2M_z}{\pi R^4} x, \end{aligned} \tag{3.87}$$

where n_o implies the initial refractive index of the ordinary optical wave.

The results presented in Fig. 3-10a agree perfectly with formulae (3.87). Hence, the piezooptic coefficient π_{14} can be determined using the relation

$$|\pi_{14}| = \frac{\Delta n_{12}}{n_o^3 \sigma_{23}(x)} = \frac{\pi R^4 \Delta n_{12}}{2 n_o^3 M_z x}, \tag{3.88}$$

where we have $n_o = 2.28647$ for the light wavelength $\lambda = 632.8$ nm [78].

Let us take $\sigma_{32} = 0$ and consider the plane $x = 0$ (Fig. 3-10b). Then the distribution of the induced birefringence and the piezooptic coefficient π_{14} along the y axis are as follows:

$$\begin{aligned} \Delta n_{12} &= n_o^3 \pi_{14} \sigma_{31} = 2 n_o^3 \pi_{14} M_z y / \pi R^4, \\ |\pi_{14}| &= \frac{\Delta n_{12}}{n_o^3 \sigma_{31}(y)} = \frac{\pi R^4 \Delta n_{12}}{2 n_o^3 M_z y}. \end{aligned} \tag{3.89}$$

Let the light propagate in the plane $x = y$ and the light beam is scanned along the bisector $\rho = \sqrt{x^2 + y^2}$ of x and y axes. Then we have $\sigma_{32} = \sigma_{31} = \sigma$ (Fig. 3-10c) and

$$\Delta n_{12} = \sqrt{2} n_o^3 \pi_{14} \sigma = 2\sqrt{2} n_o^3 \pi_{14} \frac{M_z}{\pi R^4} x = 2 n_o^3 \pi_{14} \frac{M_z}{\pi R^4} \rho,$$
$$|\pi_{14}| = \frac{\Delta n_{12}}{\sqrt{2} n_o^3 \sigma} = \frac{\pi R^4 \Delta n_{12}}{2\sqrt{2} n_o^3 M_z x} = \frac{\pi R^4 \Delta n_{12}}{2 n_o^3 M_z \rho}. \quad (3.90)$$

The piezooptic coefficients $|\pi_{14}|$ calculated using the formulae (3.88), (3.99), (3.90) and the experimental data are equal to $(0.836 \pm 0.020) \times 10^{-12}$, $(0.892 \pm 0.020) \times 10^{-12}$ and $(0.933 \pm 0.040) \times 10^{-12}$ m^2/N, respectively. These values are close to each other, with the average being equal to $(0.887 \pm 0.028) \times 10^{-12}$ m^2/N.

In other words, the above experimental results testify that the torsion-optical method represents an accurate method for measuring the non-principal piezooptic coefficients. In particular, the relative measurement error does not exceed 3.1%.

It should also be noted that the coefficient π_{14} determined for the $LiNbO_3$ crystals with the torsion-optic method agrees well with the data obtained in a number of works with the interferometric methods (e.g., $\pi_{14} = 0.7 \times 10^{-12}$ m^2/N [67, 79, 80] and $\pi_{14} = -0.81 \times 10^{-12}$ m^2/N [60]). However, the sign of this coefficient has not been determined unambiguously. In addition, the relative errors of these measurements are significantly greater ($\sim 15\%$, according to Ref. [60]). In other terms, the accuracy of the torsion-optic method is significantly higher than that of the technique [60].

Note also that the torsion-optic method enables determining the sign of piezooptic coefficients. The corresponding procedures will be described in Subsection 3.4.

3.3. Determination of piezooptic coefficient π_{14} in α-BaB_2O_4 crystals

The efficiency of torsion-optic method for measuring the piezooptic coefficients has been verified using the example of BaB_2O_4 crystals [78]. These crystals represent an efficient acoustooptic material for controlling powerful short-wavelength optical radiation [79]. This is why the knowledge of their piezooptic and elastooptic properties has a practical meaning.

It is known that BaB_2O_4 has two structural modifications, α-BaB_2O_4 and β-BaB_2O_4. β-BaB_2O_4 crystals are one of the best nonlinear optical materials [80−84]. The torsion-optic method has been used to study the α-BaB_2O_4 crystals, which belong to the point symmetry group $\bar{3}m$.

The piezooptic tensor for the point symmetry groups $3m$ and $\bar{3}m$ (i.e., the groups corresponding to $LiNbO_3$ and BaB_2O_4) is as follows:

$$\pi_{\lambda\mu} = \begin{bmatrix} \pi_{11} & \pi_{12} & \pi_{13} & \pi_{14} & 0 & 0 \\ \pi_{12} & \pi_{11} & \pi_{13} & -\pi_{14} & 0 & 0 \\ \pi_{31} & \pi_{31} & \pi_{33} & 0 & 0 & 0 \\ \pi_{41} & -\pi_{41} & 0 & \pi_{44} & 0 & 0 \\ 0 & 0 & 0 & 0 & \pi_{44} & 2\pi_{41} \\ 0 & 0 & 0 & 0 & \pi_{14} & \pi_{66} \end{bmatrix}. \tag{3.91}$$

When a torsion moment is applied to α-BaB_2O_4 and the light propagates along the z axis (i.e., the experimental geometry $(M_z, k \| z)$ is dealt with), the induced birefringence occurs in the xy-plane. The induced birefringence and the piezooptic coefficient π_{14} in the polar coordinate system $\{\rho\varphi\}$ ($x = \rho\cos\varphi$ and $y = \rho\sin\varphi$) are determined as

$$\Delta n_{12} = 2n_o^3 \pi_{14} \frac{M_z}{\pi R^4} \rho, \tag{3.92}$$

$$|\pi_{14}| = \frac{\Delta n_{12}}{2n_o^3 M_z \rho} \pi R^4. \tag{3.93}$$

A crystalline sample for torsion-optical studies has been made in the shape of octagonal prism, the side faces of which are parallel to the z axis

and the bases are parallel to the xy plane. The sample sizes are equal to 11.9 mm along the z axis and 6.6 mm between the side faces.

Fig. 3-11 shows spatial distributions of the rotation angle of optical indicatrix and the birefringence induced by the torsion moment in α-BaB_2O_4 crystals.

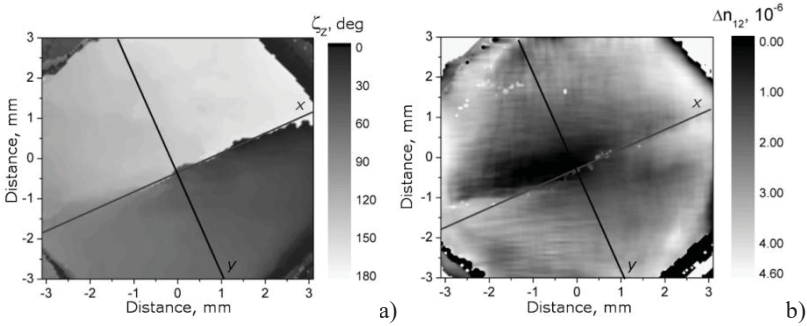

Fig. 3-11. Distributions of rotation angle of optical indicatrix (a) and birefringence (b) induced by the torsion moment $M_z = 0.058\ \mathrm{N \times m}$ ($\lambda = 632.8$ nm) in the cross-section xy of α-BaB_2O_4 crystals [81].

Adapted with permission from Vasylkiv, Yu., Savaryn, V., Smaga, I., Skab, I., Vlokh, R. (2011). On determination of sign of the piezooptic coefficients using torsion method. Appl. Opt., 50(17), 2512–2518. © The Optical Society.

As seen from Fig. 3-11a, the rotation of optical indicatrix by the 180 deg around the geometric centre of the cross-section xy occurs whenever the angle φ changes by 360 deg. In the polar coordinate system, the rotation angle of optical indicatrix can be written as

$$\tan 2\zeta_z = \frac{\sigma_{13}}{\sigma_{23}} = \frac{y}{x} = \frac{\sin\varphi}{\cos\varphi} = \tan\varphi \ \text{ or } \ \zeta_z = \varphi/2. \tag{3.94}$$

Under the condition $y = 0$, the optical indicatrix rotation ζ_z is equal to 0 or 90 deg along the directions $+x$ or $-x$, respectively. Under the condition $x = 0$ it is equal to +45 or –45 deg for the directions $+y$ or $-y$, respectively. This feature can help in determining the orientations of x and y axes [88].

Note that the x axis is perpendicular to one of the mirror symmetry planes ($x \perp m$) in our coordinate system. It is seen from Fig. 3-11b that the

shape of the surface describing the induced-birefringence distribution is close to conical one, which agrees well with the formula (3.92).

A system of lines can be obtained by plotting the dependences of induced birefringence on the distance ρ for different polar angles φ under constant torsion moment, $M_z = 0.058\ \mathrm{N}\times\mathrm{m}$ (see Fig. 3-12). These dependences enable one to determine the modulus of the coefficient π_{14} (Fig. 3-13).

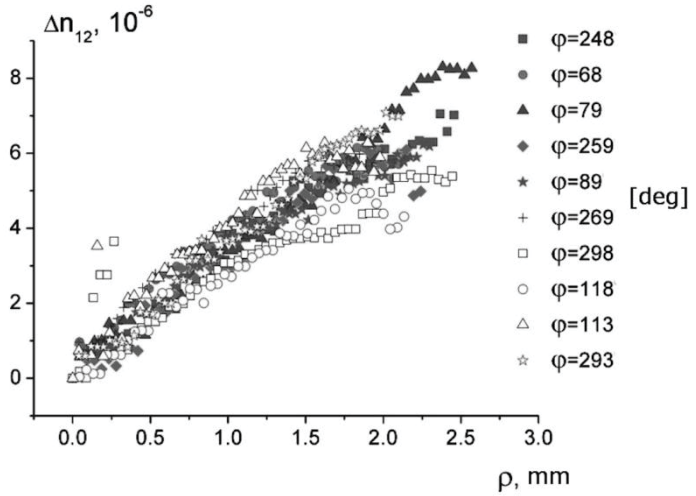

Fig. 3-12. Dependences of induced birefringence on the distance ρ from the center of cross-section xy in α-BaB_2O_4, as obtained at different polar angles φ and a constant torsion moment $M_z = 0.058\ \mathrm{N}\times\mathrm{m}$ [81].

Adapted with permission from Vasylkiv, Yu., Savaryn, V., Smaga, I., Skab, I., Vlokh, R. (2011). On determination of sign of the piezooptic coefficients using torsion method. Appl. Opt., 50(17), 2512–2518. © The Optical Society.

One can improve further the accuracy for the coefficient π_{14} by increasing the number of the above dependences. In practice, the number of experimental dependences can be large enough. For example, the coefficient π_{14} for α-BaB_2O_4 crystals has been determined basing on 40 dependences. Its value is equal to $|\pi_{14}| = (1.77 \pm 0.16)\times 10^{-12}\ \mathrm{m^2/N}$, with the relative error not exceeding 8.9%.

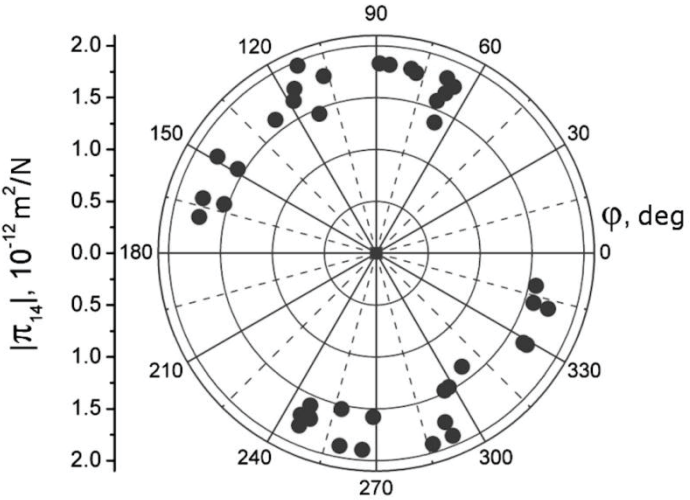

Fig. 3-13. Dependence of piezooptic coefficient π_{14} on the polar angle φ for α - BaB_2O_4 crystals ($\lambda = 632.8$ nm) [81].

Adapted with permission from Vasylkiv, Yu., Savaryn, V., Smaga, I., Skab, I., Vlokh, R. (2011). On determination of sign of the piezooptic coefficients using torsion method. Appl. Opt., 50(17), 2512–2518. © The Optical Society.

As noted above, the torsion-optic method applied to $LiNbO_3$ makes it possible to determine the piezooptic coefficients with the experimental error $\sim 3.1\%$ ($|\pi_{14}| = (0.887 \pm 0.028) \times 10^{-12}$ m^2/N [72, 75]). If compared to the case of $LiNbO_3$, the error for the piezooptic coefficient π_{14} obtained for the α - BaB_2O_4 crystals is higher. This is caused by extra inhomogeneities and internal stresses associated with crystal growth. The latter phenomena manifest themselves in deviations of the birefringence distribution from the conical shape (Fig. 3-11b).

Notice that the piezooptic coefficient π_{14} obtained for the α - BaB_2O_4 crystals is close to that found earlier for β - BaB_2O_4 ($\pi_{14} = -(2.0 \pm 0.8) \times 10^{-12}$ m^2/N [47]). A closeness of these piezooptic coefficients can be due to the fact that α - and β - modifications are nothing but different structural phases appearing in the course of phase transition in the same crystalline material, BaB_2O_4.

Finally, we would stress that the accuracy achieved for the piezooptic coefficients with our torsion-optic method is significantly higher than that reported in a typical work [47] where the errors are as high as 40%.

It is known that the total optical retardation, which is measured in most of the piezooptic experiments, consists of the two parts: (i) the optical retardation caused by the "pure" piezooptic effect, and (ii) the optical retardation associated with changing sample thickness along the direction of light propagation. The latter effect is due to the Poisson effect:

$$\delta\Delta_k = \delta\Delta n_k d_k - \Delta n_k \delta d_k \text{ or } \pi_{km}^0 = \pi_{km}^* + 2\Delta n_k S_{km}. \tag{3.95}$$

Here d_k denotes the initial sample thickness along the direction of light propagation (this direction is given by the index k), Δn_k the initial birefringence along this direction, δd_k and $\delta\Delta n_k$ are respectively the thickness and birefringence increments in the direction k (they are caused by axial mechanical loading of a sample along the direction specified by the index m), $\delta\Delta_k$ stands for the optical retardation change, S_{km} the elastic compliance components, π_{km}^0 the "pure" piezooptic coefficient directly related to the refractive-index change, and π_{km}^* the piezooptic coefficient determined directly in experiment [14].

According to formula (3.95), the extra factors S_{km} and Δn_k participating in the "elastic contribution" (i.e., the last term on the r. h. s. of this formula) are necessary to estimate the "pure" piezooptic coefficients. However, when the experimenter employs the torsion-optic method for measuring the piezooptic coefficients, the Poisson effect does not affect the resultant optical retardation. Indeed, since we have $\Delta n_3 = 0$ and $S_{34} = S_{35} = 0$ for the $LiNbO_3$ and α-BaB_2O_4 crystals, there is no "elastic contribution" at all.

When we apply torsion to α-BaB_2O_4 around the z axis, the following five components of the mechanical strain tensor remain nonzero:

$$\begin{aligned} &\varepsilon_{11} = \frac{2M_z}{\pi R^4} S_{14} x, \ \varepsilon_{22} = -\frac{2M_z}{\pi R^4} S_{14} x, \ \varepsilon_{33} = 0, \\ &\varepsilon_{32} = \frac{2M_z}{\pi R^4} S_{44} x, \ \varepsilon_{31} = \frac{2M_z}{\pi R^4} S_{55} y, \ \varepsilon_{12} = \frac{4M_z}{\pi R^4} S_{14} y. \end{aligned} \tag{3.96}$$

These components can lead to elastooptic coupling. This situation is similar to that occurring in the $LiNbO_3$ crystals. In addition, the elastooptic tensors of these crystals are also the same [68]. Therefore, the experimental geometry $(M_z, k \| z)$ enables one to determine the linear combination of

elastooptic coefficients $p_{14}S_{44} + 2p_{66}S_{14}$ for the α-BaB_2O_4 crystals. It is described by the relation

$$p_{14}S_{44} + 2p_{66}S_{14} = \frac{\pi R^4}{2n_o^3 M_z x}\Delta n_{12} = \frac{\pi R^4}{2n_o^3 M_z y}\Delta n_{12} = \pi_{14}. \qquad (3.97)$$

The above effective elastooptic coefficient can be obtained directly from a torsion-optic experiment or by calculating the coefficient π_{14} determined in advance. Since the corresponding elastic compliances for α-BaB_2O_4 are equal to $S_{44} = (21.6\pm0.4)\times10^{-11}$ m^2/N and $S_{14} = (1.8\pm0.2)\times10^{-11}$ m^2/N [82], we have the difference of elastooptic coefficients $6p_{14} - p_{66} = -(0.049 \pm 0.001)$. This value can be used for checking the elastooptic coefficients derived for the α-BaB_2O_4 crystals with the other methods.

3.4. Determination of signs of the piezooptic coefficients with torsion method (examples of $LiNbO_3$ and α-BaB_2O_4 crystals)

It has been shown above that the torsion-optic method is an efficient and accurate tool for determining the absolute values of non-principal piezooptic coefficients. However, the signs of piezooptic coefficients also represent an important issue in the studies of piezooptic properties. As a result, below we analyze whether the signs of piezooptic coefficients can be determined with the torsion-optical method. Particular examples of $LiNbO_3$ and α-BaB_2O_4 crystals have been chosen for this aim [81].

It is seen from relations (3.90) and (3.93) that the sign of the piezooptic coefficient $\pi_{14} = \Delta n_{12}\pi R^4/(2n_o^3 M_z \rho)$ depends on the sign of induced birefringence Δn_{12} and the sign of torsion moment M_z. Let us try to determine these signs, provided that the coordinate eigensystem of optical indicatrix, the coordinate system of torsion moment and the components of shear stresses are known.

In order to determine the sign of the induced birefringence, one has to carry out an additional experiment aimed at establishing orientation of the optical indicatrix in the laboratory coordinate system (Fig. 3-14), i.e. the orientations of ellipsoid semi-axes, which correspond to the smallest (N_p) and intermediate (N_m) refractive indices.

Note that, in optically biaxial crystals, the semi-axis N_m corresponds to the direction perpendicular to the plane of optic axes, while the semi-axis N_p belongs to this plane. The orientation of optical indicatrix can be determined by observing the changes occurring in the conoscopic pattern under torsion of a sample.

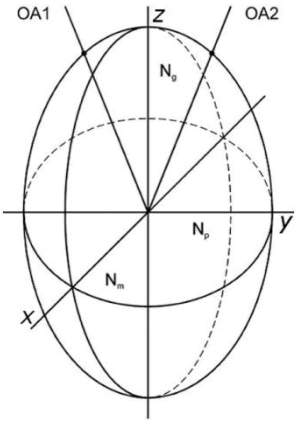

Fig. 3-14. Optical indicatrix for optically biaxial crystals and a right-handed Cartesian coordinate system: OA1 and OA2 correspond to optic axes [81].
Adapted with permission from Vasylkiv, Yu., Savaryn, V., Smaga, I., Skab, I., Vlokh, R. (2011). On determination of sign of the piezooptic coefficients using torsion method. Appl. Opt., 50(17), 2512–2518. © The Optical Society.

Let the laser beam propagate along the z direction through a number of points inside the cross-section xy, which differ by their coordinates (e.g., the points $(x_c;0)$ and $(-x_c;0)$ in Fig. 3-15).

Let us select a right-handed Cartesian coordinate system, in which the positive birefringence $+\Delta n_{xy}$ are associated with a counterclockwise rotation about the z axis (i.e., $+\Delta n_{xy} = n_x - n_y = N_m - N_p$). The signs of the other principal birefringence values can be found from the general equality $\Delta n_{xy} + \Delta n_{yz} + \Delta n_{zx} = 0$. Then the value $+\Delta n_{zx} = n_z - n_x = N_g - N_m$ is positive (since N_g is the largest refractive index that corresponds to the z direction), while the value $-\Delta n_{yz} = n_y - n_z = N_p - N_g$ is negative.

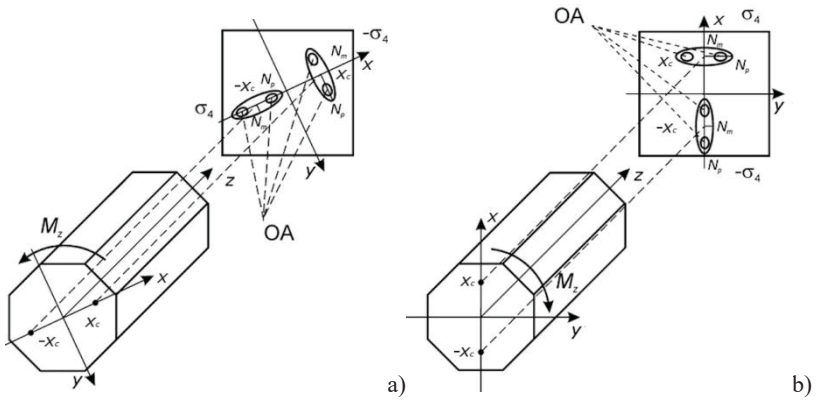

Fig. 3-15. Orientations of samples, torsion moments and changes in the conoscopic patterns observed in α-BaB_2O_4 (a) and $LiNbO_3$ (b): OA denote outlets of optic axes [81].

Adapted with permission from Vasylkiv, Yu., Savaryn, V., Smaga, I., Skab, I., Vlokh, R. (2011). On determination of sign of the piezooptic coefficients using torsion method. Appl. Opt., 50(17), 2512–2518. © The Optical Society.

In our experiments, the torsion moment has been applied to the front face of a crystalline prism, while the back face remains unaffected (see Fig. 3-15). During the action of torsion moment, we have observed the conoscopic patterns. As a result, the birefringence induced in α-BaB_2O_4 has been found to be positive at the coordinates $(x_c;0)$ and negative at the coordinates $(-x_c;0)$ (see Fig. 3-15a). The same is true for the $LiNbO_3$ crystals (see Fig. 3-15b). The next step is determining the sign of the shear stress caused by the torsion moment at the above coordinates (see Fig. 3-15). We obtain that the shear stress components are equal to $\sigma_5 = 0$ and $\sigma_4 \neq 0$ at these coordinates. The sign of the component σ_4 can be determined provided that the sign of the angle γ characterizing the shear deformation component $\varepsilon_4 = 2\tan\gamma$ is known. The signs of the components σ_4 and ε_4 are the same, since we have $\sigma_4 = S_{44}\varepsilon_4$.

Herewith, the positive angle γ must correspond to counterclockwise rotation from the y axis towards the z axis (see Fig. 3-16). When a torsion moment is applied to α-BaB_2O_4, the value σ_4 becomes negative at the coordinates $(x_c;0)$ and positive at the coordinates $(-x_c;0)$. For the $LiNbO_3$

crystals, the value σ_4 becomes positive at the coordinates $(x_c;0)$ and negative at the coordinates $(-x_c;0)$.

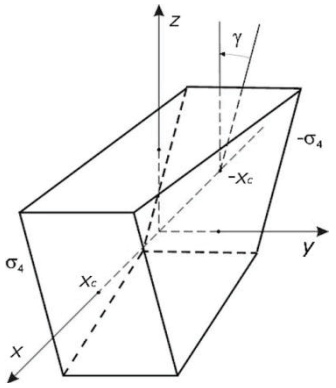

Fig. 3-16. Schematic representation of shear deformations occurring at the points $(x_c;0)$ and $(-x_c;0)$ in $LiNbO_3$ after a torsion moment is applied according to Fig. 3-15b [81].

Adapted with permission from Vasylkiv, Yu., Savaryn, V., Smaga, I., Skab, I., Vlokh, R. (2011). On determination of sign of the piezooptic coefficients using torsion method. Appl. Opt., 50(17), 2512–2518. © The Optical Society.

Basing on the results of our analysis, the signs of the piezooptic coefficients π_{14} for the both crystals can be determined. For example, we obtain the following relations for α-BaB_2O_4:

$$\pi_{14}=\frac{\pi R^4}{2n_o^3M_z}\frac{(+\Delta n)}{(-\sigma_4)}\ \text{at}\ (x_c;0),\ \pi_{14}=\frac{\pi R^4}{2n_o^3M_z}\frac{(-\Delta n)}{(+\sigma_4)}\ \text{at}\ (-x_c;0). \qquad (3.98)$$

Hence, we obtain $\pi_{14}=-(1.77\pm0.16)\times10^{-12}\ \mathrm{m^2/N}<0$.

For the case of $LiNbO_3$ crystals we have

$$\pi_{14}=\frac{\pi R^4}{2n_o^3M_z}\frac{(+\Delta n)}{(+\sigma_4)}\ \text{at}\ (x_c;0),\ \pi_{14}=\frac{\pi R^4}{2n_o^3M_z}\frac{(-\Delta n)}{(-\sigma_4)}\ \text{at}\ (-x_c;0), \qquad (3.99)$$

so that $\pi_{14}=(0.887\pm0.028)\times10^{-12}\ \mathrm{m^2/N}>0$. Note that the signs of the piezooptic coefficients π_{14} for the α-BaB_2O_4 and $LiNbO_3$ crystals obtained from the relations (3.98) and (3.99) agree with the data reported in the works [47] and [67], respectively.

SECTION 4

STUDY OF PIEZOOPTIC COEFFICIENTS USING DIGITAL LASER IMAGING INTERFEROMETRY AND FOUR-POINT BENDING

As we have already noted, when measuring piezooptic coefficients, one can load a sample such that a non-uniform, though a priori known, distribution of stresses is formed. This represents a possible alternative to simple axial compression of samples prepared in the shape of parallelepipeds. Particular examples of such an approach can be diametrical compression, mechanical torsion and four-point bending [55]. The first two methods applied for measuring the piezooptic constants of optical materials have been discussed in Section 2 and Section 3. Below we will discuss a method for determining piezooptic coefficients, which is based on the four-point bending combined with a digital laser imaging interferometry.

4.1. Method for determination of piezooptic coefficients based on four-point bending and imaging interferometry. Testing of the method on photoelastic characteristics of BK7 optical glass

4.1.1. Four-point bending

A canonical method of four-point bending induces a stressed-deformed state of "pure bending" in a bar made from some material [89]. In Fig. 4-1 we illustrate schematically application of a load to a sample according to this method.

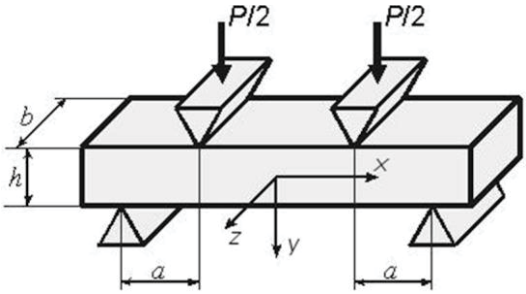

Fig. 4-1. Scheme of loading a sample according to the method of four-point bending, and selection of a laboratory Cartesian coordinate system: light propagates along the *z* direction.

Adapted with permission from Krupych, O., Savaryn, V., Krupych, A., Klymiv, I., & Vlokh, R. (2013). Determination of piezo-optic coefficients of crystals by means of four-point bending. Appl. Opt., 52(17), 4054–4061. © The Optical Society.

The mechanical stress tensor components σ_m in the central part of the sample, i.e., between the upper punches in Fig. 4-1, are determined as follows:

$$\sigma_1 \equiv \sigma_x = \frac{6Pa}{bh^3} y\,, \tag{4.1}$$

$$\sigma_2 \equiv \sigma_y = 0\,, \tag{4.2}$$

$$\sigma_3 \equiv \sigma_z = 0\,. \tag{4.3}$$

Here P is the loading force, h and b respectively the height and the thickness of sample, and a the distance between the planes where the forces act.

It follows from equations (4.1)–(4.3) that only one stress tensor component, σ_1, is nonzero in the central part of sample. According to formula (4.1), its value varies from $\sigma_1 = -3Pa/bh^2$ on the top face ($y = -h/2$), through the state with $\sigma_1 = 0$ in the neutral plane ($y = 0$), to $\sigma_1 = +3Pa/bh^2$ on the bottom face ($y = h/2$). Such geometry implies that the upper sample face is compressed whereas the bottom one expanded, with equal strength modules. It should be noted that, according to equation (4.1), the dependence of the stress component σ_1 on the y coordinate is linear. The appropriate slope is determined by geometrical parameters and a force being applied.

To test linearity of the spatial distribution of the stress tensor component σ_1 along the *y* coordinate, we have experimentally obtained a spatial map of the phase difference for a glass bar subjected to four-point bending (Fig. 4-2).

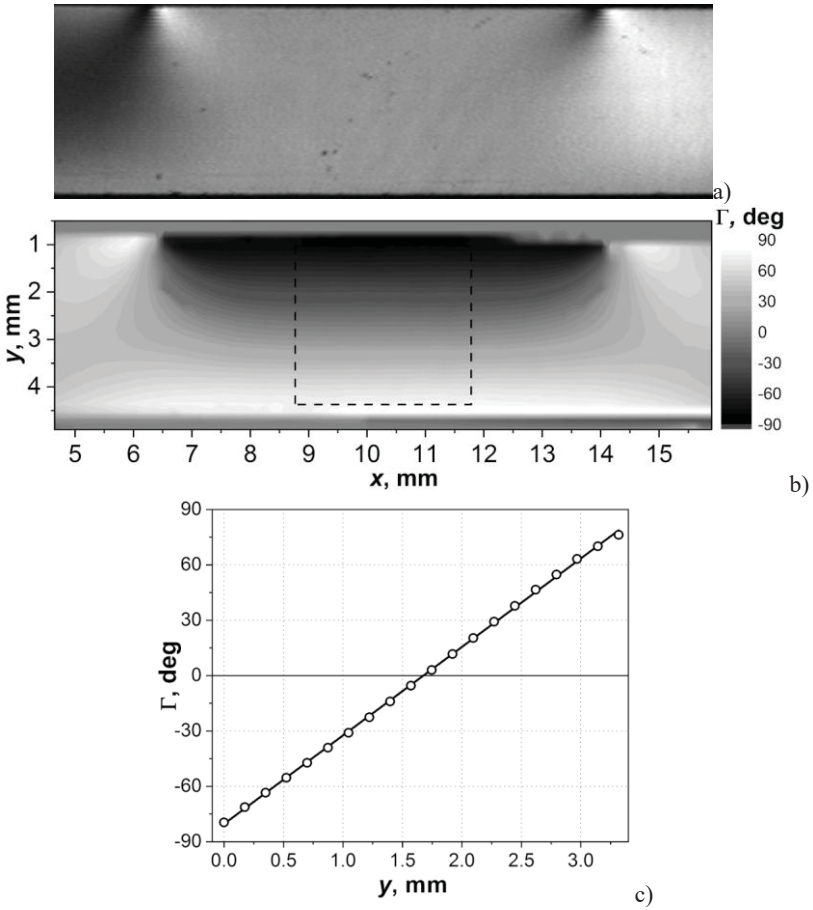

Fig. 4-2. Characterization of a glass bar subjected to four-point bending: (a) central part of sample in the field of view of 2D polarimeter, (b) map of optical phase difference Γ, and (c) dependence of averaged phase difference Γ on the *y* coordinate. Averaging is performed along rows inside the area highlighted in the map by a dashed line.

As see from Fig. 4-2, the dependence of the phase difference Γ on the *y* coordinate is linear inside at least a middle third of the gap between the top points where the force is applied, which is indicated in the both figures. The phase difference Γ is proportional to the birefringence, which, in its turn, is linearly associated with the mechanical stresses, in accordance with the relation (1.1). Therefore, the component of the mechanical stress tensor σ_1 depends linearly on the *y* coordinate at least in the interval $x \in [-l/6; +l/6]$, where *l* is the distance between the top punches. This means that, inside this region, the relation (4.1) is exactly valid and can be used to calculate the stresses in a sample subjected to four-point bending.

4.1.2. Experimental setup and measurement procedures

Our experimental setup [62] is based upon an interferometer built according to a Mach−Zender scheme and equipped with a CCD camera for recording interference patterns (Fig. 4-3).

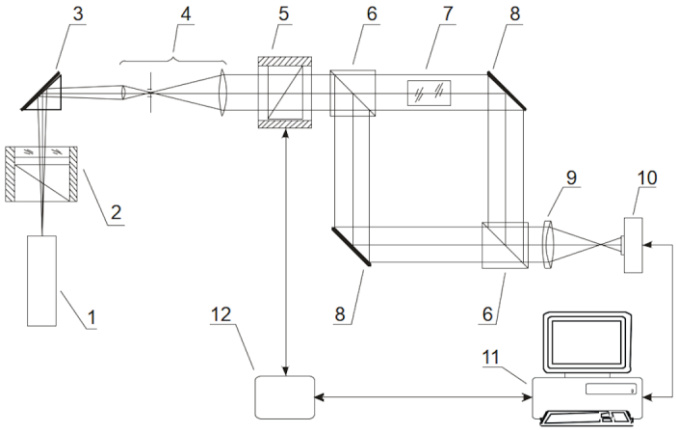

Fig. 4-3. 2D digital laser interferometer: (1) He-Ne laser; (2) circular polarizer; (3) right angle prism; (4) beam expander; (5) linear polarizer (Glan prism) in a motorized rotary stage; (6) beam-splitting prism; (7) sample under test; (8) mirror; (9) objective lens; (10) CCD camera; (11) computer; (12) stepper-motor controller. *Adapted with permission from Krupych, O., Savaryn, V., Skab, I., & Vlokh, R. (2011). Interferometric measurements of piezooptic coefficients by means of four-point bending method. Ukr. J. Phys. Opt., 12(3), 150–160. © O. G. Vlokh Institute of Physical Optics.*

A He-Ne laser (1) emits polarized light with the wavelength $\lambda = 632.8$ nm, which passes through a circular polarizer (2). Rotation of this

polarizer around the axis of laser beam allows a smooth reduction of light intensity. A beam expander (4) converts the laser beam into a collimated beam with the diameter ~ 20 mm. A linear polarizer (5) converts the circular polarization of laser beam into the linear polarization. The azimuth of linear polarization is controlled by means of a motorized rotary stage and a stepper-motor controller (12). A beam-splitting prism (6) splits the input beam into reference and object beams, which form two arms of the interferometer. Here the object beam propagates through a sample under test (7). After being reflected by mirrors (8), the reference and object beams are brought together by means of a second prism (6), thus giving rise to an interference pattern. A lens (9) builds the sample's image on a photosensitive matrix of a CCD camera (10). As a result, the image with a clear interference pattern is obtained in its plane. This image is digitized with the camera interface and transmitted to a computer (11). Special software allows one to control operation of the interferometer and saves a sequence of interference patterns for their further processing.

The phase difference between the arms of interferometer is written as follows:

$$\Delta\Phi = \frac{2\pi}{\lambda} b\left(n - n_m\right), \tag{4.4}$$

where b denotes the thickness of sample along the direction of light transmission, and n and n_m are the refractive indices of the sample and the surrounding medium, respectively.

For the interferometer in air ($n_m \approx 1$), the phase difference increment $\delta\Phi$ induced by loading of initially isotropic sample is given by the relation

$$\begin{aligned} \delta\Phi = \Delta\Phi_1 - \Delta\Phi_0 = \frac{2\pi}{\lambda}\left[b'\left(n'-1\right) - b\left(n_0 - 1\right)\right] = \\ = \frac{2\pi}{\lambda}\left[\delta n\left(b + \delta b\right) + \delta b\left(n_0 - 1\right)\right], \end{aligned} \tag{4.5}$$

where $b' = b + \delta b$ implies the thickness of sample in its loaded state, δb the Poisson's elongation (or contraction) along the z direction, $n' = n_0 + \delta n$ and n_0 are the refractive indices of the sample respectively in loaded and non-loaded states, and δn is the refractive-index increment induced by piezooptic effect.

Due to the action of single-axial mechanical stress, a birefringence appears in an optically isotropic sample. The principal axes of the optical

indicatrix are oriented parallel and perpendicular to the mechanical stress, i.e. horizontally and vertically. The following refractive-index increments can be obtained for these two directions of light polarization at the entrance of sample:

$$\delta n_1 = K_{\parallel}\sigma_1 = \left(-\frac{1}{2}n_0^3\pi_{11}\right)\sigma_1,\ \delta n_2 = K_{\perp}\sigma_1 = \left(-\frac{1}{2}n_0^3\pi_{12}\right)\sigma_1, \qquad (4.6)$$

with $K_{\parallel}$ and $K_{\perp}$ being the *photoelastic constants* (denoted sometimes as C_1 and C_2), and π_{11} and π_{12} denoting the piezooptic coefficients. The difference of the coefficients $K_{\parallel}$ and $K_{\perp}$ determines the *stress optical coefficient* $K = K_{\parallel} - K_{\perp}$, which is a standard characteristic of optical glasses. This parameter can be used to verify our technique.

As seen from equation (4.6), the coefficients π_{11} and $K_{\parallel}$ can be determined using the horizontal polarization of incoming radiation, while π_{12} and $K_{\perp}$ using the vertical polarization.

If the sample is made of an isotropic amorphous material such as glass or plastic, the change in its thickness can be expressed as:

$$\delta b = \varepsilon_3 b = \frac{1}{E}\left[\sigma_3 - \nu\left(\sigma_1 + \sigma_2\right)\right]b = -\frac{\nu}{E}\sigma_1 b\,, \qquad (4.7)$$

where ε_3 stands for the component of strain tensor, ν the Poisson's ratio, and E the Young's module.

Note that, for a general case of anisotropic materials, equation (4.7) should include an actual component of the strain tensor ε_λ, instead of the coefficient ε_3. This actual component depends on the orientation of crystallographic coordinate system. It is determined by the tensor form of the Hooke's law (1.5). Then the relation (4.7) can be rewritten to

$$\delta b = \varepsilon_\lambda b = S_{\lambda\mu}\sigma_\mu b\,. \qquad (4.8)$$

Comparing formulae (4.7) and (4.8), one can see that the effective compliance module S^{eff} for the isotropic media is expressed through the Young's module E and the Poisson's ratio ν:

$$S^{eff} = -\frac{\nu}{E}\,. \qquad (4.9)$$

For the optical glass BK7, we have $\nu = 0.206$ and $E = 82$ GPa [90]. Therefore, we arrive at $\delta b/b \approx 10^{-5}$ with the maximal experimental loading $\sim 10^7$ Pa, which has been applied in our experiments. Thus, we have the inequality $\delta b << b$ and, therefore, the equation (4.5) becomes simpler:

$$\delta\Phi = \frac{2\pi}{\lambda}\left[\delta n \times b + \delta b\left(n_0 - 1\right)\right], \tag{4.10}$$

which corresponds to the changes in the optical path length given in the work [66]. Substituting (4.6) and (4.7) into equation (4.10), we obtain for an amorphous isotropic sample

$$\begin{aligned}
\delta\Phi_1 &= \frac{2\pi}{\lambda} b\left[-\frac{1}{2} n_0^3 \pi_{11} - \frac{\nu}{E}\left(n_0 - 1\right)\right]\sigma_1 = \frac{2\pi}{\lambda} b\, Q_1\, \sigma_1, \\
\delta\Phi_2 &= \frac{2\pi}{\lambda} b\left[-\frac{1}{2} n_0^3 \pi_{12} - \frac{\nu}{E}\left(n_0 - 1\right)\right]\sigma_1 = \frac{2\pi}{\lambda} b\, Q_2\, \sigma_1,
\end{aligned} \tag{4.11}$$

where $Q_i = K_i + D = \left[-\frac{1}{2} n_0^3 \pi_{1i} - \frac{\nu}{E}\left(n_0 - 1\right)\right]$ denotes the effective (actual) photoelastic coefficient, $K_i = -n_0^3 \pi_{1i}/2$ the photoelastic coefficient, and $D = -\nu(n_0 - 1)/E$ the strain-related term.

In case of a crystalline sample the phase difference increment $\delta\Phi$ should be expressed with using elastic compliance tensor components $S_{\lambda\mu}$ instead of Young's module E and the Poisson's ratio ν. According to the relation (4.8), it is given by

$$\delta\Phi = \frac{2\pi}{\lambda} b\left[-\frac{1}{2} n_\theta^3 \pi_{\theta\mu} + S_{\lambda\mu}\left(n_\theta - 1\right)\right]\sigma_\mu = \frac{2\pi}{\lambda} b\, Q\, \sigma_\mu, \tag{4.12}$$

where $Q = K + D$, $K = -n_\theta^3 \pi_{\theta\mu}/2$ and $D = S_{\lambda\mu}(n_\theta - 1)$.

Substituting formula (4.1) for the stress component σ_1 into formulae (4.11) and (4.12), we obtain the dependences of the increments $\delta\Phi$ on the y coordinate

$$\delta\Phi_1\left(y\right) = \frac{12\pi Pa}{\lambda h^3} Q_1\, y, \qquad \delta\Phi_2\left(y\right) = \frac{12\pi Pa}{\lambda h^3} Q_2\, y\,, \tag{4.13}$$

$$\delta\Phi(y) = \frac{12\pi Pa}{\lambda h^3} Q_{ef}\, y\,, \tag{4.14}$$

which are valid respectively for both isotropic and anisotropic materials. Equations (4.13) or (4.14) can be used to determine experimentally the effective photoelastic coefficient.

Notice that an irregularity of sample thickness is typically very small, so that the thickness errors are about 0.1%. In addition, 2D interferometry allows for controlling slight displacements of sample as a whole, which can occur under loading, by comparing the sample images obtained before and after a load is applied. Due to this feature, the experimental errors caused by a wedge-like shape of sample can be avoided. Still, such errors are inevitably inherent in the method of axial compression [91], which is based on interferometry and uses an unexpanded laser beam and a single-element photodetector.

As a part of our measurement procedures, the linear input polarization is set along the vertical direction. After that five interferograms for a free sample are recorded. Then the loading force is applied, after which five relevant interferograms are taken. A similar measurement cycle is performed for the horizontal input polarization.

To process experimental data, special software in the C# programming language at the .NET platform has been developed [63]. As an example, our program reads a package of five graphic files containing interferograms for a free sample in the case of vertical input polarization. The first image of the series is rendered in the program window (see Fig. 4-4).

Then a user selects a rectangular region inside the sample image, the data from which will be used in further calculations. To reduce the influence of noise on the final results, a smoothing filter can be applied. Next, a user clicks the button “Calculate current” to start the data processing for an active image or the button “Calculate all” for all of the files opened.

At the beginning of data processing, the first row of the selected region is used to fit the dependence of the intensity I on the x coordinate by a harmonic function, with the amplitude A, the period w and the extrema’s offset x_m:

$$I = C + A\cos\left[\frac{2\pi}{w}\left(x - x_m\right)\right], \tag{4.15}$$

where C is the average intensity level.

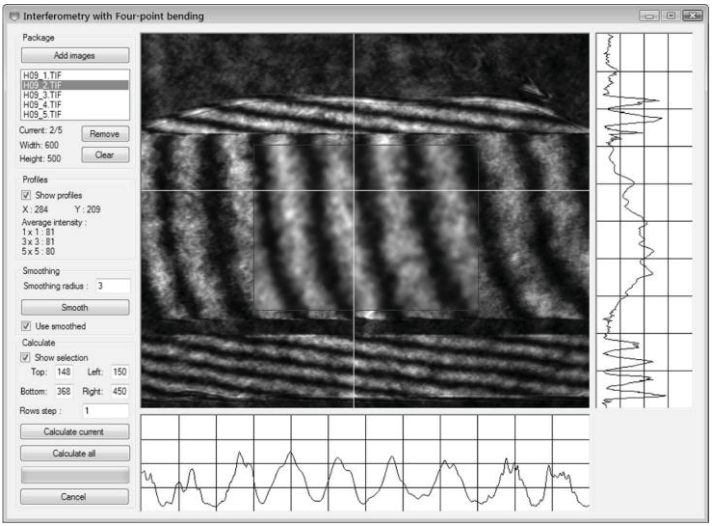

Fig. 4-4. Program window with a typical interferogram: the field of view is 5.71×6.30 mm and the image size 500×600 pixels. A selected rectangular area in the sample image contains smoothed data corresponding to the area under test.
Adapted with permission from Krupych, O., Savaryn, V., Krupych, A., Klymiv, I., & Vlokh, R. (2013). Determination of piezo-optic coefficients of crystals by means of four-point bending. Appl. Opt., 52(17), 4054–4061. © The Optical Society.

The results of fitting are displayed in the window shown in Fig. 4-5. A lower right corner of the window contains a plot corresponding to experimental intensities (indicated by circles) for a selected row and a solid line, constructed according to formula (4.15) with the parameters C, A, w and x_m obtained due to the fitting procedure. An analysis of this plot allows a user to ensure correctness of the fitting procedure.

Then the period w and the horizontal offset x_m obtained for a single line are used to calculate the phase difference for a certain coordinate x_c, (usually, the center of the selected region) using the formula

$$\Delta\Phi = \frac{2\pi}{w}\left(x_c - x_m\right). \tag{4.16}$$

The procedure described above is repeated for each next row, resulting in some resultant $\Delta\Phi(y)$ dependence. The plots of the $\Delta\Phi(y)$ dependences for each of the five interferograms, as well as the plots of the dependences of averaged phase difference, are given in the upper right part of the fitting-result window (see Fig. 4-5).

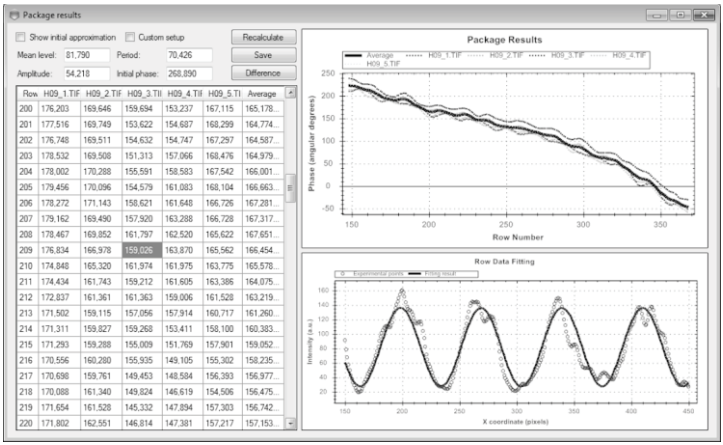

Fig. 4-5. Example of calculations of $\Delta\Phi(y)$ dependences: a lower plot shows experimental data for a selected table cell (a line 209 of the file "H09_3.TIF") and a fit with sinusoidal function.
Adapted with permission from Krupych, O., Savaryn, V., Krupych, A., Klymiv, I., & Vlokh, R. (2013). Determination of piezo-optic coefficients of crystals by means of four-point bending. Appl. Opt., 52(17), 4054–4061. © The Optical Society.

After acquiring the dependences $\Delta\Phi_0(y)$ for free sample and $\Delta\Phi'(y)$ for loaded sample, one can calculate their difference and obtain the dependence of the phase difference increment $\delta\Phi(y) = \Delta\Phi'(y) - \Delta\Phi_0(y)$ (see Fig. 4-6).

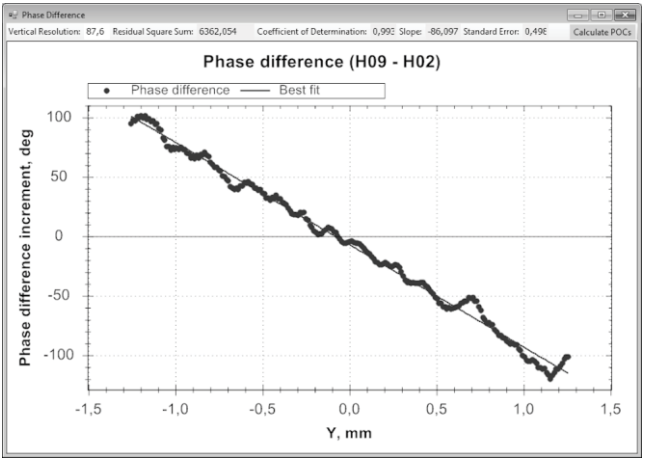

Fig. 4-6. Dependence of phase-difference increment $\delta\Phi(y)$: circles correspond to experimental data and straight line to the best linear fit.

The analysis of formulae (4.13) and (4.14) suggests that, by fitting the experimental dependence $\delta\Phi(y)$ with the linear function $\delta\Phi(y) = Ay + B$, the angular coefficient A can be obtained. On this basis, the coefficient Q can be calculated using the formula

$$Q = \frac{\lambda h^3}{12\pi Pa} A \,. \tag{4.17}$$

Then the photoelastic coefficient K is given by

$$K = Q - D = Q - S_{\lambda\mu}\left(n_v - 1\right), \tag{4.18}$$

where $S_{\lambda\mu}$ stands for the actual component of the elastic compliance tensor and n_v the initial refractive index for the vertical polarization of light.

Using the photoelastic coefficient K, one can calculate the piezooptic coefficient $\pi_{v\mu}$ (with the index v denoting the vertical light polarization):

$$\pi_{v\mu} = -\frac{2K}{n_v^3} \,. \tag{4.19}$$

As a next step, the input light polarization is changed from vertical to horizontal and the measurement procedure described above is repeated to obtain the piezooptic coefficient $\pi_{h\mu}$ (with the index h denoting the horizontal polarization of light). In this way, the effective piezooptic coefficients $\pi_{v\mu}$ and $\pi_{h\mu}$ can be determined for a given direction of light propagation through a sample.

4.1.3. Determination of the piezooptic coefficients for isotropic media with four-point bending: an example of BK7 optical glass

We have checked our method for measuring the piezooptic coefficients, using a model isotropic material, a BK7 optical glass [92]. Fig. 4-7 presents typical interferograms obtained for the piezooptic effect in this glass.

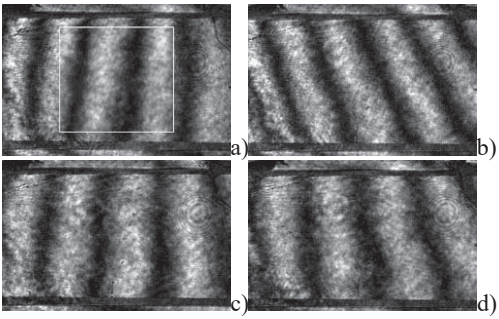

Fig. 4-7. Typical interferograms obtained for a sample of BK7 optical glass: (a) free sample (vertical polarization), (b) loaded sample (vertical polarization), (c) free sample (horizontal polarization), and (d) loaded sample (horizontal polarization). The field of view is 3.65×5.58 mm^2, the image size 361×600 pixels, the loading force 80.9 N. We analyze the area selected in image (a), which contains smoothed data.

Adapted with permission from Krupych, O., Savaryn, V., Skab, I., & Vlokh, R. (2011). Interferometric measurements of piezooptic coefficients by means of four-point bending method. Ukr. J. Phys. Opt., 12(3), 150–160. © O. G. Vlokh Institute of Physical Optics.

As noted above, two different piezooptic coefficients can be determined for a given propagation direction, depending on the polarization of light. For isotropic materials, the piezooptic tensor contains only two independent components, π_{11} and π_{12}. To determine them, it is enough to test a single sample along a single propagation direction.

According to the above procedure, we have obtained dependences of the phase difference increments $\delta\Phi_1(y)$ and $\delta\Phi_2(y)$ for the horizontal and vertical polarizations (Fig. 4-8). Subsequently, these dependences have been fitted with the linear functions, from where the slopes can be calculated. Then the Q_1 and Q_2 coefficients have been found.

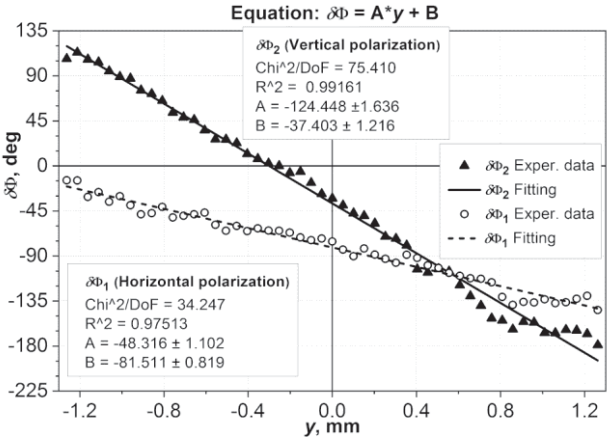

Fig. 4-8. Dependences of phase difference increments $\delta\Phi_1(y)$ and $\delta\Phi_2(y)$ fitted with linear functions. The fitting results and the corresponding statistics are given in the legends.

Adapted with permission from Krupych, O., Savaryn, V., Skab, I., & Vlokh, R. (2011). Interferometric measurements of piezooptic coefficients by means of four-point bending method. Ukr. J. Phys. Opt., 12(3), 150–160. © O. G. Vlokh Institute of Physical Optics.

Next, the coefficients $K_{\|}$, $K_{\perp}$ and K have been calculated for the two alternative interferometer configurations. In the first configuration, the interferometer has been adjusted so that about five interference fringes are observed in the field of view, and about eight bands observed in the second configuration.

The coefficients $K_{\|}$, $K_{\perp}$ and K thus obtained are shown in Table 4-1, where the corresponding literature data are also provided for comparison. It is the data given by the manufacturers of optical glasses.

Table 4-1. Photoelastic coefficients of the BK7 optical glass obtained experimentally, and the corresponding literature data

Coefficient	Configuration 1	Configuration 2	Literature data (λ = 589 nm)
$K_{\|}$, B	–0.490 ± 0.045	–0.548 ± 0.050	–0.5 [92]
$K_{\perp}$, B	–3.302 ± 0.063	–3.269 ± 0.050	–3.3 [92]
K, B	2.811 ± 0.077	2.722 ± 0.071	2.77 [93]

One can see that, for all of experimentally measured coefficients, the literature data coincides with our results within the confidence intervals. In other words, the experimental results obtained by us are well consistent with

the available data, which indicates a high accuracy of our method. The relative error for the K coefficient does not exceed 3%, thus confirming a high precision of our experimental setup and the computing procedures.

Basing on the coefficients $K_{\|}$ and $K_{\perp}$ given above, the following piezooptic coefficients have been derived: $\pi_{11} = (0.282 \pm 0.026)$ B and $\pi_{12} = (1.899 \pm 0.036)$ B for the first interferometer configuration, and $\pi_{11} = (0.315 \pm 0.029)$ B and $\pi_{12} = (1.880 \pm 0.029)$ B for the second configuration. The average piezooptic coefficients are equal to $\langle \pi_{11} \rangle = 0.299$ B and $\langle \pi_{12} \rangle = 1.890$ B. The absolute error that reflects reproducibility of our piezooptic coefficients does not exceed ± 0.036 B. This corresponds to the best accuracy known from the literature (see [81, 94]).

Unfortunately, the reference book of optical materials [92] contains only the elastooptic coefficients $p_{11} = 0.12$ and $p_{12} = 0.22$ for the BK7 optical glass. They are associated with the piezooptic coefficients via the Young's module E and the Poisson's ratio ν:

$$p_{11} = \frac{E\left[(1-\nu)\pi_{11} + 2\nu\pi_{12}\right]}{(1+\nu)(1-2\nu)}, \qquad p_{12} = \frac{E(\pi_{12} + \nu\pi_{11})}{(1+\nu)(1-2\nu)}. \tag{4.20}$$

The coefficients $p_{11} = 0.118 \pm 0.004$ and $p_{12} = 0.226 \pm 0.005$ have been calculated following from the experimental values π_{11} and π_{12} and the formulae (4.20). It is seen that they also agree well with the literature data. In other words, our error levels are quite sufficient in terms of the typical requirements known from the reference literature.

A simple comparison testifies that the accuracy of our method is not worse than that of the Dixon-Cohen method, which provides the best performance when determining the elastooptic coefficients [70, 71]. However, unlike the Dixon-Cohen method, our method reveals another significant advantage: it allows for determining the signs of piezooptic and photoelastic coefficients. This can be done when the signs of the mechanical stresses are known and the interferometer is calibrated properly.

Finally, we stress that our technique can also be promising when determining the piezooptic coefficients of crystalline materials.

4.1.4. Studies for the photoelastic characteristics of borate glasses

Using the above procedures for determining piezooptic coefficients in isotropic media, which are based on the four-point bending, we have also examined a number of samples of borate glasses $LiKB_4O_7$, $Li_2B_6O_{10}$ (LiB_3O_5) and $LiCsB_6O_{10}$ [95, 96]. The interferograms obtained during our studies for the piezooptic effect in these glasses are illustrated in Fig. 4-9–4-11.

The coefficients $K_{\|}$, $K_{\perp}$ and K have been calculated for these borate glasses (see Table 4-2). Note that the stress optical coefficient K for the borate glasses exceeds almost twice the corresponding coefficient for the BK7 glass. This means that the birefringence induced by the same mechanical stress is almost twice as large in the borate glass, when compared with the BK7 glass. High enough elastooptic coefficients of the borate glasses are also worth noting. This fact makes these materials promising for acoustooptics.

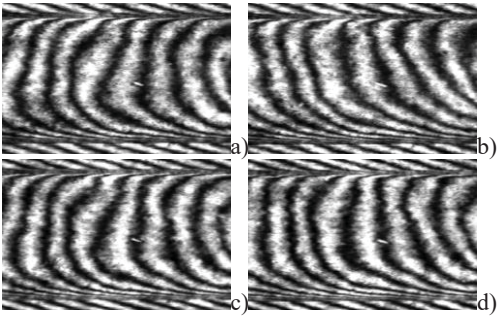

Fig. 4-9. Interferograms obtained for a sample of $LiKB_4O_7$ borate glass: (a) free sample (vertical polarization), (b) loaded sample (vertical polarization), (c) free sample (horizontal polarization), and (d) loaded sample (horizontal polarization). The field of view is 3.05×3.12 mm^2, the image size 270×300 pixels, and the loading force 57.1 N.

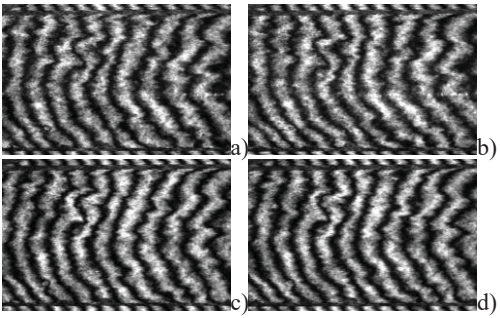

Fig. 4-10. Interferograms obtained for a sample of $Li_2B_6O_{10}$ borate glass: (a) free sample (vertical polarization), (b) loaded sample (vertical polarization), (c) free sample (horizontal polarization), and (d) loaded sample (horizontal polarization). The field of view is 4.52×6.16 mm^2, the image size 400×500 pixels, and the loading force 57.1 N.

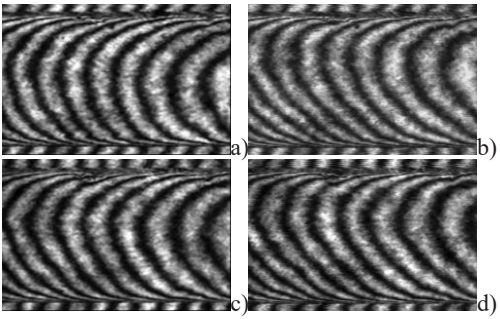

Fig. 4-11. Interferograms obtained for a sample of $LiCsB_6O_{10}$ borate glass: (a) free sample (vertical polarization), (b) loaded sample (vertical polarization), (c) free sample (horizontal polarization), and (d) loaded sample (horizontal polarization). The field of view is 3.55×4.94 mm^2, the image size 313×400 pixels, and the loading force 57.1 N.

As seen from Table 4-2, the absolute and relative errors for determining the coefficient K are respectively equal to 0.33 B and 4% for the $LiKB_4O_7$ borate glass, 0.39 B and 8% for the $Li_2B_6O_{10}$ borate glass, and 0.34 B and 6% for the $LiCsB_6O_{10}$ borate glass.

Table 4-2. Experimental values of effective coefficients

No.	Coefficient, B	Borate glass		
		$LiKB_4O_7$	$Li_2B_6O_{10}$	$LiCsB_6O_{10}$
1	$Q_{\parallel}$	–3.80 ± 0.09	–3.29 ± 0.09	–6.25 ± 0.14
2	$Q_{\perp}$	–8.78 ± 0.19	–8.15 ± 0.17	–11.69 ± 0.24
3	$D = S(n-1)$	–2.31 ± 0.18	–2.68 ± 0.24	–3.57 ± 0.14
4	$K_{\parallel}$	–1.49 ± 0.20	–0.61 ± 0.26	–2.68 ± 0.19
5	$K_{\perp}$	–6.47 ± 0.26	–5.47 ± 0.30	–8.12 ± 0.28
6	$K = K_{\parallel} - K_{\perp}$	4.98 ± 0.33	4.86 ± 0.39	5.44 ± 0.34
7	π_{11}	0.85 ± 0.12	0.35 ± 0.15	1.50 ± 0.11
8	π_{12}	3.69 ± 0.15	3.14 ± 0.17	4.56 ± 0.16
9	$\pi_{44} = \pi_{11} - \pi_{12}$	–2.84 ± 0.19	–2.79 ± 0.23	–3.06 ± 0.19
10	p_{11}	0.250 ± 0.013	0.184 ± 0.016	0.286 ± 0.010
11	p_{12}	0.382 ± 0.014	0.300 ± 0.018	0.386 ± 0.013

4.2. Studies for the photoelastic characteristics of trigonal crystals using four-point bending: an example of lithium niobate

Unlike isotropic glasses, crystals reveal anisotropy, i.e. their matrices of piezooptic coefficients contain generally more than two independent components. This means that, in order to determine the complete piezooptic matrix for a certain crystal, it is necessary to make measurements for many samples oriented in different ways with respect to the principal coordinate system which is sometimes called a "crystallo-physical" system. It was shown above that only two acting coefficients can be determined for a given direction of light propagation However, using crystalline samples prepared in the shape of a bar with a cross-section close to square ($b \approx h$, see Fig. 4-1) allows that each sample can be illuminated along two mutually perpendicular directions. This technique increases the number of the coefficients which can be measured for a single sample. Thus, it reduces the total number of samples required.

We have tested the above method for measuring the piezooptic coefficients of anisotropic media, using a trigonal crystal of lithium niobate ($LiNbO_3$). It belongs to the point symmetry group $3m$, the piezooptic matrix of which contains eight independent components:

$$\pi_{ij} = \left[\begin{array}{ccc:ccc} \pi_{11} & \pi_{12} & \pi_{13} & \pi_{14} & 0 & 0 \\ \pi_{12} & \pi_{11} & \pi_{13} & -\pi_{14} & 0 & 0 \\ \pi_{31} & \pi_{31} & \pi_{33} & 0 & 0 & 0 \\ \hdashline \pi_{41} & -\pi_{41} & 0 & \pi_{44} & 0 & 0 \\ 0 & 0 & 0 & 0 & \pi_{44} & 2\pi_{41} \\ 0 & 0 & 0 & 0 & \pi_{14} & (\pi_{11}-\pi_{12}) \end{array}\right]. \tag{4.21}$$

The analysis of this matrix shows that, in order to determine all the coefficients with the four-point bending technique, it is necessary to examine at least four different crystalline samples. To determine the five principal coefficients (π_{11}, π_{12}, π_{13}, π_{31} and π_{33}), it is enough to examine only two samples [63]. In total, seven samples of $LiNbO_3$ crystals have been made [64]. Their dimensions and orientations of the faces relative to the principal coordinate system are presented in Table 4-3.

Table 4-3. Dimensions of crystalline $LiNbO_3$ samples (in mm) and orientations of their faces (Miller indices)

Sample No.	Long axis		Side axis 1		Side axis 2	
	Direction	Dimension, mm	Direction	Dimension, mm	Direction	Dimension, mm
1	[100]	18.1	[010]	3.16	[001]	3.03
2	[001]	18.1	[100]	3.03	[010]	2.84
3.1, 3.2, 3.3	[100]	18.1	[011]	2.63	$[0\bar{1}1]$	3.13
4	$[0\bar{1}1]$	18.1	[100]	3.03	[011]	2.84
5	[010]	18.1	[100]	3.03	[001]	3.14
6	[101]	18.1	[010]	3.15	$[\bar{1}01]$	3.02
7	[010]	18.1	[101]	3.03	$[\bar{1}01]$	2.84

The effective piezooptic coefficients and the parameters for all of the samples under test, which correspond to different experimental geometries, are collected in Table 4-4, where n_o and n_e are respectively the ordinary and extraordinary refractive indices.

In general, to calculate the effective coefficient $\pi_{\theta\mu}$ with the relations (4.18) and (4.19), it is necessary to determine experimentally the Q parameter, know the effective component of the elastic compliance tensor $S_{\lambda\mu}$ (or a combination of its components) and have the refractive index n_θ.

Table 4-4. Effective piezooptic coefficients of $LiNbO_3$ crystals and experimental conditions under which they are determined

Sample No.	Piezooptic coefficient	Nonzero stress components	Direction of light propagation	Compliance component	Direction of light polarization	Refractive index
1	π_{11}	σ_1	[001]	$S_{31}=S_{13}$	[100]	n_o
	$\pi_{21}=\pi_{12}$	σ_1	[001]	$S_{31}=S_{13}$	[010]	n_o
	π_{11}	σ_1	[010]	$S_{21}=S_{12}$	[100]	n_o
	π_{31}	σ_1	[010]	$S_{21}=S_{12}$	[001]	n_e
2	π_{33}	σ_3	[010]	$S_{23}=S_{13}$	[001]	n_e
	π_{13}	σ_3	[010]	$S_{23}=S_{13}$	[100]	n_o
	π_{33}	σ_3	[100]	S_{13}	[001]	n_e
	$\pi_{23}=\pi_{13}$	σ_3	[100]	S_{13}	[010]	n_o
3	π_{11}	σ_1	$[0\bar{1}1]$	$(S_{12}+S_{13}-S_{14})/2$	[100]	n_o
	$(\pi_{12}+\pi_{31}+2\pi_{41})/2$	σ_1	$[0\bar{1}1]$	$(S_{12}+S_{13}-S_{14})/2$	[011]	n_{45}*
	π_{11}	σ_1	[011]	$(S_{12}+S_{13}+S_{14})/2$	[100]	n_o
	$(\pi_{12}+\pi_{31}-2\pi_{41})/2$	σ_1	[011]	$(S_{12}+S_{13}+S_{14})/2$	$[0\bar{1}1]$	n_{45}
4	$(\pi_{11}+\pi_{13}+\pi_{31}+\pi_{33}-$ $-\pi_{14}-2\pi_{41}+2\pi_{44})/4$	σ_2, σ_3, σ_4	$[0\bar{1}1]$	$(S_{11}+2S_{13}+S_{33}-S_{44})/4$	[011]	n_{45}
	$(\pi_{12}+\pi_{13}+\pi_{14})/2$	σ_2, σ_3, σ_4	$[0\bar{1}1]$	$(S_{11}+2S_{13}+S_{33}-S_{44})/4$	[100]	n_o
	$(\pi_{11}+\pi_{13}-\pi_{14})/2$	σ_2, σ_3, σ_4	[100]	$(S_{12}+S_{13}+S_{14})/2$	[010]	n_o
	$(\pi_{31}+\pi_{33})/2$	σ_2, σ_3, σ_4	[100]	$(S_{12}+S_{13}+S_{14})/2$	[001]	n_e
5	$\pi_{22}=\pi_{11}$	σ_2	[001]	$S_{32}=S_{13}$	[010]	n_o
	π_{12}	σ_2	[001]	$S_{32}=S_{13}$	[100]	n_o
	$\pi_{22}=\pi_{11}$	σ_2	[100]	S_{12}	[010]	n_o
	$\pi_{32}=\pi_{31}$	σ_2	[100]	S_{12}	[001]	n_e
6	$(\pi_{11}+\pi_{13}+\pi_{31}+\pi_{33}+2\pi_{44})/4$	σ_1, σ_3, σ_5	$[\bar{1}01]$	$(S_{11}+2S_{13}+S_{33}-S_{44})/4$	[101]	n_{45}
	$(\pi_{12}+\pi_{13})/2$	σ_1, σ_3, σ_5	$[\bar{1}01]$	$(S_{11}+2S_{13}+S_{33}-S_{44})/4$	[010]	n_o
	$(\pi_{11}+\pi_{13})/2$	σ_1, σ_3, σ_5	[010]	$(S_{12}+S_{13})/2$	[100]	n_o
	$(\pi_{31}+\pi_{33})/2$	σ_1, σ_3, σ_5	[010]	$(S_{12}+S_{13})/2$	[001]	n_e
7	$\pi_{22}=\pi_{11}$	σ_2	$[\bar{1}01]$	$(S_{12}+S_{13})/2$	[010]	n_o
	$(\pi_{12}+\pi_{31})/2$	σ_2	$[\bar{1}01]$	$(S_{12}+S_{13})/2$	[101]	n_{45}
	$\pi_{22}=\pi_{11}$	σ_2	[101]	$(S_{12}+S_{13})/2$	[010]	n_o
	$(\pi_{12}+\pi_{31})/2$	σ_2	[101]	$(S_{12}+S_{13})/2$	$[\bar{1}01]$	n_{45}

*$n_{45}=[2/(n_o^2+n_e^2)]^{1/2}=2.243$; $n_o=2.286$; $n_e=2.203$.

As seen from Table 4-4, some piezooptic coefficients can be determined from different independent measurements. For example, the coefficient π_{11} can be obtained with eight different experimental geometries, while the coefficients π_{12}, π_{13}, π_{31} and π_{33} can be found only in two different geometries. This provides higher reliability of the piezooptic coefficients, which is achieved by averaging the results of independent measurements.

Unlike the principal piezooptic coefficients which can be obtained directly, non-principal piezooptic coefficients enter in complex relationships for the effective piezooptic coefficients, which contain combinations of many different coefficients. Therefore, their determination must rely upon oblique (non-principal) crystal sections. Moreover, it needs calculating the effective elastic compliances, which are expressed by complex combinations of individual compliance modules. Such circumstances increase the calculation errors for the non-principal piezooptic coefficients.

When calculating the piezooptic coefficients basing on the coefficients Q, we have used the compliance modules for the $LiNbO_3$ crystals reported in the work [97]. The only exception is the coefficient S_{14}, which has been taken with the positive sign, according to the IRE standards [98, 99].

As a result of our measurements and calculations, the complete matrix of piezooptic coefficients for the $LiNbO_3$ crystals has been obtained. It includes eight independent coefficients, the averages of which are given in the second column of Table 4-5. These results are compared with the principal piezooptic coefficients reported previously in Refs. [63, 81] and the results given in the work [60].

Table 4-5. Piezooptic coefficients for $LiNbO_3$ crystals (our experiments and literature data)

Piezooptic coefficient (B)	Experiment [64]	Experiment [63]	Experiment [81]	Literature [60]
π_{11}	–0.376±0.069	–0.40±0.07	–	–0.38
π_{12}	0.197±0.039	0.224±0.009	–	0.09
π_{13}	0.662±0.065	0.66±0.02	–	0.80
π_{31}	0.529±0.025	0.51±0.02	–	0.50
π_{33}	0.253±0.024	0.251±0.008	–	0.20
π_{14}	0.875±0.071	–	0.887±0.028	–0.81
π_{41}	–0.228±0.051	–	–	–0.88
π_{44}	2.060±0.071	–	–	2.25

As seen from Table 4-5, increasing numbers of the samples under analysis and the independent measurements have somewhat changed the data for the principal piezooptic coefficients, if compared with the data [63]. On the other hand, the experimental errors have even increased in some cases. This fact is easily understood given inevitable orientation errors that occur when one manufactures a larger quantity of crystalline samples. In spite of somewhat reduced accuracy, the use of a larger quantity of samples leads to higher reliability of the final results.

In most cases, our results agree fairly well with the data taken from the work [60]. Only the coefficients π_{12} and π_{41} differ markedly from these results. Besides, the coefficient π_{14} differs in its sign from the data [60]. At the same time, the sign and the absolute value of the coefficient π_{14} are the same as obtained using a crystal-rod twisting method [81]. Considering that the signs of the coefficients π_{14} and π_{41} depend on the sign of Cartesian coordinate system and the positive direction of z axis in the right-handed coordinate system, this result is evident. After all, the right-handed coordinate system has been used both in this experiment and in the work [81], whereas the direction of the z axis has been determined according to the IRE standard, i.e. with a positive piezoelectric coefficient d_{33} and a positive elastic compliance S_{14}.

To explain deviations of our piezooptic coefficients from the experimental data of the other authors, it is necessary to take into account the effect of joint action of piezoelectric and electrooptic effects on the measured piezooptic coefficients. In general, the coefficient measured for a piezo-electric material can be written as

$$\pi_{\lambda\mu} = \pi^{E}_{\lambda\mu} + \pi^{*}_{\lambda\mu} = \pi^{E}_{\lambda\mu} + \frac{r_{\lambda i} d_{i\mu}}{\varepsilon_0 \chi_{ii}} \quad (i = 1\ldots3,\ \ \lambda, \mu = 1\ldots6)\,, \tag{4.22}$$

where $\pi^{E}_{\lambda\mu}$ is the piezooptic coefficient under a constant electric field (a "primary" coefficient), $\pi^{*}_{\lambda\mu}$ the contribution due to a joint action of piezoelectric and electrooptic effects (a "secondary" coefficient); $r_{\lambda i}$ the coefficient of linear electrooptic effect, $d_{i\mu}$ the piezoelectric coefficient, χ_{ii} the component of dielectric-susceptibility tensor, and $\varepsilon_0 = 8.85\times10^{-12}$ F/m the electric constant.

All of the secondary coefficients have been calculated using the literature data for the electrooptic, piezoelectric and dielectric-susceptibility tensors [61]. When evaluating the secondary coefficients, we have found that they can have the same order of magnitude as the primary coefficients.

To eliminate the contribution of the secondary effect, the samples are usually short-circuited electrically. Then the electric field is zero, i.e. the piezooptic coefficients measured in practice are just the primary coefficients.

One has to stress that the configuration of electric field induced by the piezoelectric effect in the samples to which the four-point bending is applied can differ significantly from the configuration occurring in the traditional scheme of uniaxial compression of parallelepiped-shaped samples. Then the corresponding contributions of the secondary coefficient to the total coefficient would also be different.

After calculating the spatial distribution of electric field, which appears in the samples under four-point bending, two characteristic configurations of the induced electric field have been found: in the first configuration, the electric field is perpendicular to the acting component of the mechanical stress tensor, while in the second configuration it is parallel to it (Fig. 4-12).

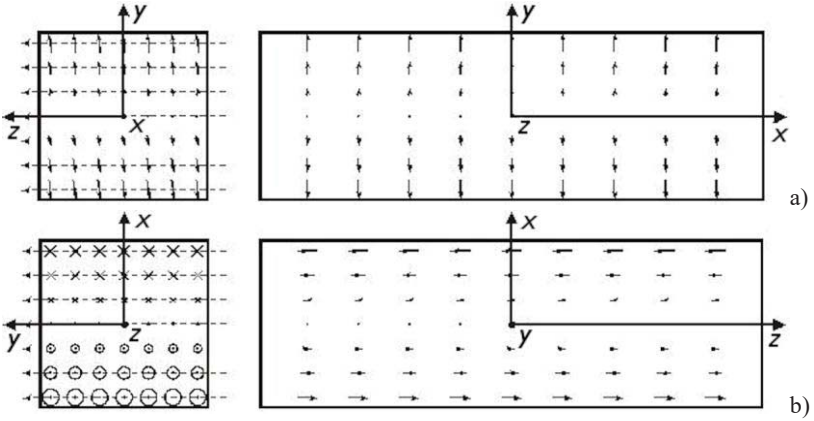

Fig. 4-12. Spatial distribution of the electric field induced by piezoelectric effect in the central part of $LiNbO_3$ sample under four-point bending: (a) sample No. 1 (*z*-cut corresponds to light propagation direction) and (b) sample No. 2 (*y*-cut corresponds to light propagation direction). The length of arrows and the size of circles and crosses are proportional to the electric field module $|\mathbf{E}|$.
Adapted with permission from Krupych, O., Savaryn, V., & Vlokh, R. (2014). Precise determination of full matrix of piezo-optic coefficients with a four-point bending technique: the example of lithium niobate crystals. Appl. Opt., 53(10), B1–B7. © The Optical Society.

In the first case (see Fig. 4-12a), only the stress component σ_1 differs from zero in the central part of sample where there is "pure bending", while the induced components of the electric field are as follows:

$$E_1 = 0, \quad E_2 = \frac{-d_{22}\sigma_1}{\varepsilon_0 \chi_{11}} = -2.84\times10^{-2}\sigma_1, \quad E_3 = \frac{d_{31}\sigma_1}{\varepsilon_0 \chi_{33}} = -0.38\times10^{-2}\sigma_1. \tag{4.23}$$

Thus, the induced electric field vector **E** lies in the *yz* plane. Note that the angle between the positive direction of the *y* axis and the vector **E** equals to 187.6 deg at $\sigma_1 > 0$ (i.e., at the bottom of sample) and 7.6 deg at $\sigma_1 < 0$ (i.e., at the top of sample). This means that the vector **E** is almost perpendicular to the upper and lower faces of our sample, with the opposite signs of the electric field on these faces.

In the second case (Fig. 4-12b), only the stress component σ_3 differs from zero and, according to the form of piezoelectric tensor, there is a single nonzero component of the electric field E_3:

$$E_1 = 0, \quad E_2 = 0, \quad E_3 = \frac{d_{33}\sigma_3}{\varepsilon_0 \chi_{33}} = 4.67\times10^{-2}\sigma_3. \tag{4.24}$$

Thus, the induced electric field vector **E** is parallel to the *z* axis at $\sigma_3 > 0$ (i.e., at the bottom of sample) and anti-parallel to the *z* axis at $\sigma_3 < 0$ (i.e., at the top of sample). In other words, the vector **E** is strictly parallel to the upper and lower faces of our sample. As a result, these faces are electrically neutral and the piezoelectric contribution to the piezooptic effect should not be observed.

When analyzing the above two cases, it would be natural to assume that compensation of electrical charges induced by the piezoelectric effect should occur differently. Hence, the influences of the secondary effect on the total coefficients should also differ from each other. To test this assumption, the piezooptic coefficients for short-circuited and non-shorted samples have been measured for these two alternative cases. As a result, we have revealed that the difference between the measured parameters does not exceed the experimental error. This implies that the four-point bending technique enables determining the primary (i.e., initial) coefficients, at least in the case of $LiNbO_3$ crystals. Unfortunately, the electrical conditions of samples examined by the other authors have not been reported (see, e.g., Ref. [60]).

The principal sources of the errors arising when determining the piezooptic coefficients in crystalline materials include the following: shortcomings of the optical techniques applied; errors of experimental setup related to misalignments of the optical scheme, fluctuation of signals, and

electronic noises; the drawbacks of single-crystal growth (deviation from stoichiometry, a presence of uncontrolled impurities, residual stresses, etc.); shortcomings of sample preparation (misorientations of crystallographic axes with respect to sample faces and imperfect processing of the faces); the measurement errors of the elastic-compliance coefficients used when calculating the piezooptic coefficients; errors associated with a secondary piezooptic effect in piezoelectric materials; nonproper definition of coordinate systems for different material tensors, which are used when calculating the piezooptic and elastooptic coefficients.

Unfortunately, the researchers rarely describe the above details in their works, which hinders more or less accurate comparison of the data. However, such a comparison can be made in some cases. For example, the error for the piezooptic coefficients averaged over all the coefficients of $LiNbO_3$ is about 15%, according to the work [60]. In its turn, according to the data [100], the averaged error for the piezooptic coefficients exceeds 33%, when the interference method is used for orthorhombic SrB_4O_7 crystals and uniaxial compression is applied. Unfortunately, a non-uniformity of mechanical stresses inside samples has been taken into account only intuitively in these works. At the same time, one can see that the average error for the piezooptic coefficients determined with the four-point bending method does not exceed 12%.

In order to assess the prospects of optical materials for acousto-optic applications, elastooptic coefficients $p_{\lambda\mu}$ are commonly used, instead of piezooptic ones. When the total matrix of piezooptic coefficients is known, the corresponding elastooptic coefficients can be calculated from the relation (1.7), provided that the complete matrix of elastic stiffnesses $C_{\theta\mu}$ is also known.

Therefore we have calculated the matrix of elastooptic coefficients, basing on the piezooptic coefficients measured with the method of four-point bending. The elastic-stiffness coefficients have been taken from the work [97]. The experimental elastooptic coefficients obtained by us are shown in the Table 4-6, where they are compared with the results published by the other authors [101, 102].

Table 4-6. Elastooptic coefficients in $LiNbO_3$ crystals

Elastooptic coefficient	Experiment [64]	Data of Ref. [101]	Data of Ref. [102]
p_{11}	–0.023± 0.017	–0.021± 0.018	–0.026
p_{12}	0.076± 0.014	0.060± 0.019	0.090
p_{13}	0.147± 0.019	0.172± 0.029	0.133
p_{31}	0.157± 0.007	0.141± 0.017	0.179
p_{33}	0.141± 0.013	0.118± 0.020	0.071
p_{14}	–0.057± 0.004	–0.052± 0.007	–0.075
p_{41}	–0.051± 0.011	–0.109± 0.017	–0.151
p_{44}	0.126± 0.004	0.121± 0.019	0.146

As seen from Table 4-6, the confidence intervals overlap for all of the elastooptic coefficients, except for p_{33} and p_{41}. This confirms that our coefficients are consistent with the literature data. It should be noted that the errors for all of the eight coefficients obtained with the four-point bending technique are smaller than those obtained in the work [101]. This fact points to high accuracy of the method and our experimental setup.

4.3. Studies for the photoelastic characteristics of tetragonal crystals (tetrahedral and pyramidal symmetry groups)

The procedures described above have been used to measure the matrix of piezooptic coefficients for $NaBi(MoO_4)_2$ and $Li_2B_4O_7$ crystals.

4.3.1. Example of $NaBi(MoO_4)_2$ crystals

The piezooptic tensor for the bismuth sodium molybdate $NaBi(MoO_4)_2$ crystals (the point symmetry group $4/m$) consists of ten independent coefficients and has the following form:

$$\pi_{ij} = \begin{bmatrix} \pi_{11} & \pi_{12} & \pi_{13} & 0 & 0 & \pi_{16} \\ \pi_{12} & \pi_{11} & \pi_{13} & 0 & 0 & -\pi_{16} \\ \pi_{31} & \pi_{31} & \pi_{33} & 0 & 0 & 0 \\ 0 & 0 & 0 & \pi_{44} & \pi_{45} & 0 \\ 0 & 0 & 0 & -\pi_{45} & \pi_{44} & 0 \\ \pi_{61} & -\pi_{61} & 0 & 0 & 0 & \pi_{66} \end{bmatrix}. \quad (4.25)$$

After conducting a complex analysis similar to that presented in the work [67], we have found all the experimental geometries necessary for determining the complete matrix of piezooptic coefficients for the $NaBi(MoO_4)_2$ crystal [103]. Basing on these results, six parallelepiped-shaped samples have been produced. The dimensions and the orientations of their faces with respect to the principal coordinate system are shown in Table 4-7.

Table 4-7. Dimensions of $NaBi(MoO_4)_2$ crystalline samples (mm) and orientations of their faces (Miller indices)

Sample No.	Long axis		Side axis 1		Side axis 2	
	Direction	Dimension, mm	Direction	Dimension, mm	Direction	Dimension, mm
1	[100]	19.4	[010]	3.28	[001]	3.33
2	[001]	16.4	[100]	3.24	[010]	3.18
3	[011]	19.3	[100]	3.33	$[0\bar{1}1]$	3.17
4	[110]	19.8	[001]	3.28	$[1\bar{1}0]$	3.20
5	[210]	19.7	[001]	3.32	$[1\bar{2}0]$	3.29
6	$\left(\frac{1}{\sqrt{2}};\frac{1}{2};\frac{1}{2}\right)$*	19.3	$[0\bar{1}1]$	3.18	$\left(-\frac{1}{\sqrt{2}};\frac{1}{2};\frac{1}{2}\right)$*	3.33

* direction cosines

When the four-point bending is applied, in the middle part of the bar a single stress component appears, which is parallel to the long axis of the specimen. The examples of interferograms obtained for the $NaBi(MoO_4)_2$ samples in their free and loaded states are shown in Fig. 4-13.

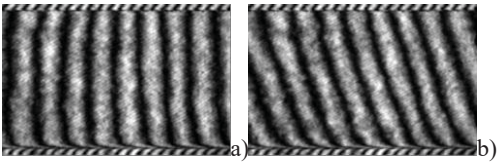

a) b)

Fig. 4-13. Interferograms obtained for the central part of $NaBi(MoO_4)_2$ sample No. 2: (a) free sample and (b) sample loaded using the four-point bending method. Light propagates along the principal direction [100] and the field of view is 5.9×3.5 mm^2.

Adapted with permission from Krupych, O., Kushnirevych, M., Mys, O., & Vlokh, R. (2015). Photoelastic properties of $NaBi(MoO_4)_2$ crystals. App. Opt., 54(16), 5016–5023. © The Optical Society.

Table 4-8 shows the expressions for the effective (operating) piezooptic coefficients Π and the elastic compliances Σ, as well as the corresponding parameters for all the samples and experimental geometries. The interferograms recorded during our experiments have been analyzed with original software, which makes it possible to obtain the coefficients Q (see Table 4-9).

The elastic-compliance coefficients required for the further calculations have been obtained from the complete matrix of elastic stiffnesses according to the formula $\mathbf{S} = \mathbf{C}^{-1}$. Then the effective elastic compliances Σ and the strain terms D have been calculated for all the experiments. The Σ and D values, as well as the experimental values of the effective coefficients K and Π are given in Table 4-9.

As seen from Table 4-9, the errors for the coefficients Q are small enough: the absolute errors do not exceed $\Delta Q_{max} = 0.213$ B and the relative errors are less than $\delta Q_{max} = 1.77\%$. These error values confirm a correctness of operation and a high accuracy of our experimental and calculation methods.

The errors of the strain terms D are determined mainly by the errors of the effective elastic compliances Σ, as follows from the relation $D = \Sigma(n - 1)$. Hence, the relative errors of the strain terms are given by the expression

$$\delta D = \sqrt{(\delta\Sigma)^2 + \left[\Delta n/(n-1)\right]^2} \,. \tag{4.26}$$

Usually the absolute errors of the refractive indices do not exceed the value $\Delta n = 0.001$. In a particular case of $NaBi(MoO_4)_2$, the relative errors of the refractive indices are given by $\delta n \le 0.046\%$. In its turn, the relative errors of the effective elastic compliances can be much larger (see Ref. [104]) and reach the values in the range of $0.21\% \le \delta\Sigma \le 1.29\%$. Then the second term under square root in the r. h. s. of formula (4.26) can be neglected, thus resulting in the approximate equality $\delta D \approx \delta\Sigma$. Hence, the maximal absolute and relative errors for the strain terms are equal to $\Delta D_{max} = 0.055$ B and $\delta D_{max} = 0.81\%$, respectively.

Table 4-8. Effective piezooptic (Π) and elastic compliance (Σ) coefficients and the corresponding experimental geometries used for $NaBi(MoO_4)_2$ crystals

Sample No.	Experimental geometry	Π	Σ	Nonzero stress components	Direction of light propagation	Direction of light polarization	Refractive index
1	*A*	π_{11}	$S_{21} = S_{12}$	σ_1	[010]	[100]	n_o
	B	π_{31}				[001]	n_e
2	*A*	π_{33}	$S_{23} = S_{13}$	σ_3	[010]	[001]	n_e
	B	π_{13}				[100]	n_o
	C	π_{33}	S_{13}	σ_3	[100]	[001]	n_e
	D	$\pi_{23} = \pi_{13}$				[010]	n_o
3	*A*	$(\pi_{11} + \pi_{13} + \pi_{31} + \pi_{33} + 2\pi_{44})/4$	$(S_{11} + 2S_{13} + S_{33} - S_{44})/4$	$\sigma_2, \sigma_3, \sigma_4$	$[0\bar{1}1]$	[011]	n_{45}*
	B	$(\pi_{12} + \pi_{13})/2$				[100]	n_o
	C	$(\pi_{11} + \pi_{13})/2$	$(S_{12} + S_{13})/2$	$\sigma_2, \sigma_3, \sigma_4$	[100]	[010]	n_o
	D	$(\pi_{31} + \pi_{33})/2$				[001]	n_e
4	*A*	$(\pi_{11} + \pi_{12} + \pi_{66})/2$	$(2S_{11} + 2S_{12} - S_{66})/4$	$\sigma_1, \sigma_2, \sigma_6$	[110]	[110]	n_o
	B	π_{31}			$[1\bar{1}0]$	[001]	n_e
5	*A*	$(17\pi_{11} + 8\pi_{12} + 8\pi_{66} - 6\pi_{16} - 12\pi_{61})/25$	$(8S_{11} + 17S_{12} + 12S_{16} - 4S_{66})/25$	$\sigma_1, \sigma_2, \sigma_6$	$[\bar{1}20]$	[210]	n_o
	B	π_{31}	$(S_{11} + 2S_{13} + S_{33} - S_{44})/4$			[001]	n_e
6	*A*	$(2\pi_{11} + \pi_{12} + \pi_{13} + \sqrt{2}\,\pi_{16})/4$	$(S_{11} + 2S_{12} + 4S_{13} + S_{33} - S_{44} - \sqrt{2}\,S_{16})/8$	$\sigma_1, \sigma_2, \sigma_3, \sigma_4, \sigma_5, \sigma_6$	$[0\bar{1}1]$	[100]	n_o
	B	$[\pi_{11} + \pi_{13} + \pi_{33} + 3\pi_{31} + 2(\pi_{12} + \pi_{44}) + \sqrt{2}\,(2\pi_{45} - \pi_{16})]/8$				[011]	n_{45}*

* $n_{45} = n_o n_e [2/(n_o^2 + n_e^2)]^{1/2} = 2.256$, $n_o = 2.308$, and $n_e = 2.199$.

Table 4-9. Experimental values of the effective coefficients obtained for $NaBi(MoO_4)_2$ crystals

Sample No.	Direction			Effective coefficient, B			
	Stress	Light propagation	Light polarization	Q	D	K	Π
1	[100]	[010]	[100]	–14.487 ±0.201	–8.191 ±0.055	–6.296 ±0.209	1.024 ±0.034
			[001]	–11.615 ±0.169	–7.508 ±0.051	–4.106 ±0.177	0.772 ±0.033
2	[001]	[010]	[001]	–15.083 ±0.209	–3.394 ±0.022	–11.689 ±0.211	2.199 ±0.040
			[100]	–13.445 ±0.189	–3.703 ±0.024	–9.742 ±0.191	1.585 ±0.031
	[001]	[100]	[001]	–15.199 ±0.213	–3.394 ±0.022	–11.805 ±0.214	2.220 ±0.040
			[010]	–13.012 ±0.198	–3.703 ±0.024	–9.310 ±0.199	1.514 ±0.032
3	[011]	$[0\bar{1}1]$	[011]	–15.242 ±0.212	–5.592 ±0.043	–9.650 ±0.217	1.691 ±0.038
			[100]	–12.313 ±0.173	–5.845 ±0.045	–6.468 ±0.179	1.052 ±0.029
	[011]	[100]	[010]	–13.374 ±0.192	–5.947 ±0.030	–7.427 ±0.194	1.208 ±0.032
			[001]	–12.824 ±0.190	–5.451 ±0.028	–7.373 ±0.192	1.387 ±0.036
4	[110]	$[1\bar{1}0]$	[110]	–7.478 ±0.112	–5.738 ±0.047	–1.740 ±0.121	0.283 ±0.020
			[001]	–7.098 ±0.117	–5.260 ±0.043	–1.838 ±0.124	0.346 ±0.023
5	[210]	$[\bar{1}20]$	[210]	–5.800 ±0.094	–2.934 ±0.021	–2.866 ±0.097	0.466 ±0.016
			[001]	–4.726 ±0.084	–2.690 ±0.020	–2.036 ±0.086	0.383 ±0.016
6	$\left(\frac{1}{\sqrt{2}};\frac{1}{2};\frac{1}{2}\right)$*	$[0\bar{1}1]$	[100]	–12.480 ±0.175	–7.254 ±0.029	–5.227 ±0.177	0.850 ±0.029
			[011]	–15.183 ±0.206	–6.940 ±0.028	–8.243 ±0.208	1.444 ±0.037

* direction cosines

Since the effective photoelastic coefficients K represent the differences between the aggregate photoelastic coefficients Q and the strain terms D (i.e., $K = Q - D$), the absolute errors ΔK can be calculated with the formula $\Delta K = \sqrt{(\Delta Q)^2 + (\Delta D)^2}$. Since the terms ΔQ is several times larger than ΔD, the ΔK errors are only slightly larger than the corresponding values ΔQ. Then the maximal absolute and relative errors for the effective photoelastic coefficients amount to $\Delta K_{max} = 0.217$ B and $\delta K_{max} = 6.98\%$, respectively.

The effective piezooptic coefficients Π are calculated on the basis of the effective photoelastic coefficients K, using the relation $\Pi = -2K/n^3$. Given this fact, the relative errors $\delta\Pi$ are almost equal to the relative errors δK, since we have $\delta K >> \delta n$. Therefore, we have $\Delta\Pi_{max} = 0.040$ B and $\delta\Pi_{max} = 6.98\%$.

To calculate the ten independent piezooptic coefficients $\pi_{\theta\mu}$, we have used the effective piezooptic coefficients Π_{ij} obtained experimentally (see Table 4-9) and the formulae

$$\left.\begin{aligned}
&\pi_{11} = \Pi_{1A},\\
&\pi_{13} = (\Pi_{2B} + \Pi_{2D})/2,\\
&\pi_{33} = (\Pi_{2A} + \Pi_{2C})/2,\\
&\pi_{31} = (\Pi_{1B} + \Pi_{4B} + \Pi_{5B})/3,\\
&\pi_{12} = 2\Pi_{3B} - \pi_{13},\\
&\pi_{66} = 2\Pi_{4A} - \pi_{11} - \pi_{12},\\
&\pi_{44} = (4\Pi_{3A} - \pi_{11} - \pi_{13} - \pi_{31} - \pi_{33})/2,\\
&\pi_{16} = (4\Pi_{6A} - 2\pi_{11} - \pi_{12} - \pi_{13})/\sqrt{2},\\
&\pi_{61} = [17\pi_{11} + 8(\pi_{12} + \pi_{66}) - 6\pi_{16} - 25\Pi_{5A}]/12,\\
&\pi_{45} = [8\Pi_{6B} - (\pi_{11} + \pi_{13} + \pi_{33}) - 2(\pi_{12} + \pi_{44}) - 3\pi_{31} + \sqrt{2}\pi_{16}]/\sqrt{8}.
\end{aligned}\right\} \quad (4.27)$$

As a result, all the piezooptic coefficients and the corresponding errors have been calculated (see Table 4-10). According to the relations (4.27), the piezooptic coefficients $\pi_{\theta\mu}$ are linear combinations of the effective piezooptic coefficients Π, so that the absolute errors $\Delta\pi$ are slightly larger than the errors $\Delta\Pi$. The maximal absolute error for the piezooptic coefficients is equal to $\Delta\pi_{max} = 0.139$ B, while the corresponding maximal relative error can reach the value $\delta\pi_{max} = 23.6\%$.

Table 4-10. Piezooptic coefficients obtained for $NaBi(MoO_4)_2$ crystals

π_{11}	π_{12}	π_{13}	π_{31}	π_{33}	π_{44}	π_{66}	π_{45}	π_{16}	π_{61}
1.024 ±0.034	0.555 ±0.063	1.550 ±0.022	0.500 ±0.015	2.209 ±0.028	0.740 ±0.080	–1.013 ±0.081	0.682 ±0.139	–0.532 ±0.106	0.440 ±0.104

Having obtained the complete matrix of piezooptic coefficients $\boldsymbol{\pi}$, one can calculate the complete matrix of elastooptic coefficients **p**, using formula (1.7) and assuming that the complete matrix of elastic stiffnesses **C** is known in advance. For the crystals of point symmetry group 4/*m*, the matrix **C** consists of seven independent coefficients. For the $NaBi(MoO_4)_2$ crystals, they have been measured by different researchers, using a number of experimental methods [104, 105]. Unfortunately, the differences among the coefficients presented by different authors are quite large (up to 15% for the coefficients C_{12}, C_{13} and C_{33}, and up to 94% for the coefficient C_{16}). The errors of calculations of the elastooptic coefficients from the piezooptic coefficients depend significantly on the accuracy of the elastic stiffnesses. Although in our experiments we have determined the elastic stiffness coefficients from the acoustic-wave velocity measurements performed in the work [106], the calculations mentioned above should be based on the elastic stiffnesses determined with higher accuracy in the work [104], where a method of resonance-antiresonance in thick plates has been employed.

As a result, the complete matrix of elastooptic coefficients has been calculated from the piezooptic coefficients measured with the four-point bending and the elastic-stiffness coefficients [104]. These elastooptic coefficients are shown in Table 4-11. The results obtained in the work [107] are also displayed for comparison.

Table 4-11. Elastooptic coefficients obtained for $NaBi(MoO_4)_2$ crystals

Elastooptic coefficient	p_{11}	p_{12}	p_{13}	p_{31}	p_{33}	p_{44}	p_{66}	p_{45}	p_{16}	p_{61}
Four-point bending method	0.196 ±0.005	0.159 ±0.007	0.189 ±0.003	0.154 ±0.002	0.228 ±0.003	0.019 ±0.002	–0.044 ±0.004	0.017 ±0.004	–0.023 ±0.004	0.035 ±0.012
Data [107]	0.243	0.205	0.25	0.21	0.29	–	–	–	–	–

4.3.2. Studies for the photoelastic characteristics of tetragonal $Li_2B_4O_7$ crystals

Optically uniaxial and optically negative lithium tetraborate $Li_2B_4O_7$ crystals belong to the point symmetry group 4*mm* of tetragonal syngony. The space symmetry group of these crystals is $I4_1cd$, and their elementary cell parameters are equal to $a = b = 9.479$ Å and $c = 10.286$ Å [108, 109].

For the point symmetry group 4*mm*, the elastic compliance tensor includes six independent components, the piezoelectric tensor includes three components, and the dielectric susceptibility tensor includes two components. On the other hand, the piezooptic tensor of $Li_2B_4O_7$ contains seven independent components. It has the following form in the principal coordinate system:

$$\pi_{ij} = \begin{bmatrix} \pi_{11} & \pi_{12} & \pi_{13} & 0 & 0 & 0 \\ \pi_{12} & \pi_{11} & \pi_{13} & 0 & 0 & 0 \\ \pi_{31} & \pi_{31} & \pi_{33} & 0 & 0 & 0 \\ 0 & 0 & 0 & \pi_{44} & 0 & 0 \\ 0 & 0 & 0 & 0 & \pi_{44} & 0 \\ 0 & 0 & 0 & 0 & 0 & \pi_{66} \end{bmatrix}. \quad (4.28)$$

To measure the piezooptic coefficients for the $Li_2B_4O_7$ crystals, the technique tested earlier for the cases of optical glasses and optically uniaxial crystals has been used. It represents a combination of the laser imaging digital interferometry and the classical four-point bending method.

By implementing a complex analysis similar to that reported in the work [66], we have obtained the parameters describing all the experimental configurations required to determine the complete matrix of piezooptic coefficients [110]. Basing on these results, four parallelepiped-shaped samples have been prepared. Their dimensions and the orientations of faces in the principal coordinate system are shown in Table 4-12.

Table 4-12. Dimensions of $Li_2B_4O_7$ samples (in mm) and orientation of their faces (Miller indices)

Sample No.	Long axis		Side axis 1		Side axis 2	
	Direction	Dimension, mm	Direction	Dimension, mm	Direction	Dimension, mm
1	[001]	12.5	[100]	2.385	[010]	2.382
2	[100]	12.6	[010]	2.387	[001]	2.389
3	[101]	12.5	$[10\bar{1}]$	2.389	[010]	2.392
4	[110]	12.5	[001]	2.390	$[1\bar{1}0]$	2.390

When the four-point bending is applied to each sample of $Li_2B_4O_7$, a single normal component of the mechanical stress tensor appears. It is parallel to the longer axis of sample.

According to the 2D digital interferometry technique, a piezooptic experiment for given light propagation and polarization directions allows one to determine a corresponding coefficient Q. Table 4-13 contains the expressions for the effective piezooptic and elastic-compliance coefficients, together with the other relevant parameters for all the samples and experimental geometries.

During the experiment, interferograms have been obtained for all the crystalline samples in their free and loaded states. The appropriate examples are displayed in Fig. 4-14. These interferograms have been analyzed with special software [63]. Owing to interferogram processing, the effective aggregate photoelastic coefficients Q have been obtained (see Table 4-14).

Table 4-13. Effective piezooptic (Π) and elastic-compliance (Σ) coefficients and the corresponding parameters describing $Li_2B_4O_7$ samples

Sample No.	Experimental geometry	Π	Σ	Nonzero stress components	Direction of light propagation	Direction of light polarization	Refractive index
1	*A*	$\pi_{23} = \pi_{13}$	S_{13}	σ_3	$x \equiv [100]$	$y \equiv [010]$	n_o
	B	π_{33}				$z \equiv [001]$	n_e
	C	π_{13}	$S_{23} = S_{13}$		$y \equiv [010]$	$x \equiv [100]$	n_o
	D	π_{33}				$z \equiv [001]$	n_e
2	*A*	π_{31}	$S_{21} = S_{12}$	σ_1	$y \equiv [010]$	$z \equiv [001]$	n_e
	B	π_{11}				$x \equiv [100]$	n_o
	C	$\pi_{21} = \pi_{12}$	$S_{31} = S_{13}$		$z \equiv [001]$	$y \equiv [010]$	n_o
	D	π_{11}				$x \equiv [100]$	n_o
3	*A*	$(\pi_{31}+\pi_{33})/2$	$(S_{12}+S_{13})/2$	σ_1, σ_3, σ_5	$y \equiv [010]$	$z \equiv [001]$	n_e
	B	$(\pi_{11}+\pi_{13})/2$				$x \equiv [100]$	n_o
	C	$(\pi_{12}+\pi_{13})/2$	$(S_{11}+2S_{13}+ +S_{33}-S_{44})/4$		$\bar{5} \equiv [\bar{1}01]$	$y \equiv [010]$	n_o
	D	$(\pi_{11}+\pi_{13}+\pi_{31}+ +\pi_{33}+2\pi_{44})/4$				$5 \equiv [101]$	n_{45} *
4	*A*	$(\pi_{11}+\pi_{12}-\pi_{66})/2$	$(S_{31}+S_{32})/2 = S_{13}$	σ_1, σ_2, σ_6	$z \equiv [001]$	$6 \equiv [\bar{1}10]$	n_o
	B	$(\pi_{11}+\pi_{12}+\pi_{66})/2$				$6 \equiv [110]$	n_o
	C	$(\pi_{31}+\pi_{32})/2 = \pi_{31}$	$(2S_{11} + 2S_{12} - - S_{66})/4$		$\bar{6} \equiv [\bar{1}10]$	$z \equiv [001]$	n_e
	D	$(\pi_{11}+\pi_{12}+\pi_{66})/2$				$6 \equiv [110]$	n_o
	D	$(\pi_{11}+\pi_{12}+\pi_{66})/2$				$6 \equiv [110]$	n_o

* $n_{45} = n_o n_e [2/(n_o^2 + n_e^2)]^{1/2} = 1.57954$, $n_o = 1.6088$, and $n_e = 1.5520$ [111]

Table 4-14. Experimental values of the effective coefficients for $Li_2B_4O_7$ crystals

Sample No.	Direction			Effective coefficient, B			
	Stress	Light propagation	Light polarization	*Q*	*D*	*K*	*Π*
1	[001]	[100]	[010]	–11.867 ±0.178	–3.602 ±0.014	–8.264 ±0.179	3.969 ±0.086
			[001]	–6.549 ±0.103	–3.266 ±0.013	–3.283 ±0.104	1.756 ±0.056
	[001]	[010]	[100]	–11.510 ±0.170	–3.602 ±0.014	–7.908 ±0.170	3.797 ±0.082
			[001]	–6.097 ±0.112	–3.266 ±0.013	–2.830 ±0.112	1.513 ±0.060
2	[100]	[010]	[001]	–1.616 ±0.034	0.679 ±0.022	–2.295 ±0.041	1.228 ±0.022
			[100]	1.259 ±0.029	0.748 ±0.024	0.511 ±0.038	–0.245 ±0.018
	[100]	[001]	[010]	–5.457 ±0.085	–3.602 ±0.014	–1.855 ±0.086	0.891 ±0.042
			[100]	–2.875 ±0.062	–3.602 ±0.014	0.728 ±0.064	–0.350 ±0.031
3	[101]	[010]	[001]	–3.889 ±0.064	–1.294 ±0.012	–2.596 ±0.066	1.389 ±0.035
			[100]	–5.506 ±0.086	–1.427 ±0.014	–4.079 ±0.088	1.959 ±0.042
	[101]	[$\bar{1}$01]	[010]	–3.552 ±0.059	0.680 ±0.008	–4.232 ±0.060	2.032 ±0.029
			[101]	–2.417 ±0.063	0.647 ±0.008	–3.065 ±0.063	1.555 ±0.032
4	[110]	[001]	[$\bar{1}$10]	–5.151 ±0.083	–3.602 ±0.014	–1.548 ±0.084	0.744 ±0.040
			[110]	–2.921 ±0.049	–3.602 ±0.014	0.682 ±0.051	–0.327 ±0.024
	[110]	[$\bar{1}$10]	[001]	–1.867 ±0.044	–0.182 ±0.012	–1.684 ±0.046	0.901 ±0.025
			[110]	1.658 ±0.044	–0.201 ±0.013	1.859 ±0.046	–0.893 ±0.022

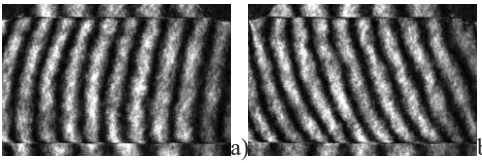

Fig. 4-14. Interferograms obtained for the central part of sample No. 1 of $Li_2B_4O_7$ crystals: (a) free sample and (b) sample loaded using the four-point bending method. Light propagates along the principal direction [100] and the field of view is 6.1×2.9 mm^2.

Adapted with permission from Krupych, O., Mys, O., Kryvyy, T., Adamiv, V., Burak, Ya., & Vlokh, R. (2016). Photoelastic properties of lithium tetraborate crystals. App. Opt., 55(36), 10457–10462. © The Optical Society.

The elastic-compliance components required for the further calculations have been taken from the work [108]. Following from the experimental data, the effective elastic compliances Σ, the strain terms D and the effective coefficients K and Π have been calculated for all the experimental geometries (see Table 4-14).

The absolute errors for the effective photoelastic coefficients Q do not exceed $\Delta Q_{max} = 0.178$ B and the relative errors are less than $\delta Q_{max} = 2.65\%$. This confirms reliability and high accuracy of our experimental and calculation procedures.

The errors associated with the strain terms D are caused mainly by the errors in the effective elastic compliances. This follows from the relation $D = \Sigma(n-1)$. Accordingly, the relative errors of the strain terms D are determined by the formula $\delta D = \sqrt{(\delta\Sigma)^2 + \left[\Delta n/(n-1)\right]^2}$. Since the absolute errors for the refractive indices Δn usually do not exceed 0.001, the relative error δn for the $Li_2B_4O_7$ crystals remains less than 0.064%.

Unfortunately, the authors of the work [108] have not indicated the error for the elastic compliances S_{ij}. This is why we have estimated the maximal absolute errors following from data-point scattering observed in their temperature dependences of the elastic compliances [108]. As a result, the following absolute errors are obtained: $\Delta S_{11} \le 0.01$ B, $\Delta S_{12} \le 0.04$ B, $\Delta S_{13} \le 0.02$ B, $\Delta S_{33} \le 0.03$ B, $\Delta S_{44} \le 0.01$ B and $\Delta S_{66} \le 0.03$ B. Basing on this data, we have concluded that the relative errors δS for all the effective elastic compliances used in our calculations are ranged from 0.34% to 6.67%.

It is obvious that the relative errors for the elastic-compliance coefficients are much larger than those for the refractive indices. Therefore the second term under the square root in the relation for δD can be

neglected, thus yielding in $\delta D \approx \delta S$. Under this condition, the maximal absolute and relative errors for the strain terms are equal to $\Delta D_{\max} = 0.024$ B and $\delta D_{\max} = 6.69\%$, respectively.

Since the coefficient K is a difference of the corresponding aggregate coefficient and the strain term ($K = Q - D$), the absolute error ΔK can be calculated with the formula $\Delta K = \sqrt{(\Delta Q)^2 + (\Delta D)^2}$. As seen from Table 4-14, the absolute errors ΔQ are in the most cases much larger than ΔD, given that the values ΔK only slightly exceed the corresponding ΔQ values. Therefore, the maximal absolute and relative errors for the effective coefficients K are equal to $\Delta K_{\max} = 0.179$ B and $\delta K_{\max} = 8.73\%$, respectively. The effective piezooptic coefficients can be calculated using the formula $\Pi = -2K/n^3$. Then the relative errors $\delta\Pi$ are almost equal to the relative errors δK, i.e. we have $\Delta\Pi_{\max} = 0.086$ B and $\delta\Pi_{\max} = 8.74\%$ again.

Finally, all of the independent piezooptic coefficients π_{qm} have been calculated from the effective coefficients Π_{ij} given in Table 4-14. The following relations have been used for this aim:

$$\left.\begin{aligned}
\pi_{11} &= (\Pi_{2B} + \Pi_{2D})/2,\\
\pi_{12} &= \Pi_{2C},\\
\pi_{13} &= (\Pi_{1A} + \Pi_{1C})/2,\\
\pi_{31} &= \Pi_{2A},\\
\pi_{33} &= (\Pi_{1B} + \Pi_{1D})/2,\\
\pi_{44} &= 2\Pi_{3D} - (\Pi_{3A} + \Pi_{3B}),\\
\pi_{66} &= (\Pi_{4B} + \Pi_{4D})/2 - \Pi_{4A}.
\end{aligned}\right\} \qquad (4.29)$$

It is seen from formulae (4.29) that each coefficient π_{qm} is calculated using the experimental Π_{ij} values obtained for a single sample. An alternative approach is to use sixteen effective coefficients Π_{ij} obtained experimentally, in order to calculate seven independent piezooptic coefficients π_{qm}. As a result, an over-determined system of linear equations is obtained, which has been solved using a standard least-squares technique.

Table 4-15 displays the sets of independent piezooptic coefficients calculated by the two methods mentioned above. The average coefficients and the corresponding errors are also given in Table 4-15.

Table 4-15. Piezooptic coefficients determined experimentally for the $Li_2B_4O_7$ crystals

Piezooptic coefficient	π_{11}	π_{12}	π_{13}	π_{31}	π_{33}	π_{44}	π_{66}
Set 1 (one coefficient derived from one sample)	–0.297 ±0.018	0.891 ±0.042	3.884 ±0.060	1.228 ±0.022	1.635 ±0.041	–0.237 ±0.085	–1.354 ±0.044
Set 2 (all samples, least-squares method)	–0.317 ±0.018	0.647 ±0.029	3.872 ±0.049	1.072 ±0.017	1.643 ±0.038	–0.024 ±0.071	–1.419 ±0.039
Average value	–0.307 ±0.018	0.769 ±0.122	3.878 ±0.055	1.150 ±0.078	1.639 ±0.040	–0.131 ±0.107	–1.387 ±0.042

Since the piezooptic coefficients π_{qm} are linear combinations of the effective coefficients Π_{ij}, the absolute errors $\Delta\pi$ are slightly larger than $\Delta\Pi$. Namely, they reach the value $\Delta\pi_{max} = 0.085$ B for the set 1 and $\Delta\pi_{max} = 0.071$ B for the set 2. The relative errors for the piezooptic coefficients can be at the most $\delta\pi_{max} = 6.1\%$ for the set 1 and $\delta\pi_{max} = 5.7\%$ for the set 2. The only exceptions are the $\delta\pi_{44}$ values, which increase up to 37% and 296%, due to a smallness of piezooptic coefficient π_{44}.

The average coefficients π_{12}, π_{31} and π_{44} found for the sets 1 and 2 do not fall into the confidence intervals. In this respect we remind that the error equal to the standard deviation corresponds to the probability level of only 68.3%. Higher probabilities correspond to still larger errors. For example, in order to provide the probability level 99.75%, the absolute error must be equal to three times the standard deviation. For the piezooptic coefficients mentioned above, the errors of the average coefficients have been calculated as a half difference between the appropriate coefficients taken from the two sets.

The piezooptic coefficients obtained with the four-point bending technique differ significantly from the data obtained using a classical method relying on uniaxial compression of parallelepiped-shaped samples [82, 112]. Here we are to remind that the four-point bending method manifests a higher accuracy, since it employs a previously known non-uniform distribution of mechanical stresses inside a sample and digital processing of experimental interferograms.

After the complete matrix of piezooptic coefficients has become known, one can calculate the corresponding elastooptic coefficients. Using the piezooptic data obtained experimentally and the elastic stiffness coefficients taken from the works [112, 113], the complete matrix of elastooptic coefficients have been calculated from the relations (1.7) (see Table 4-16).

Table 4-16. Elastooptic coefficients obtained for the $Li_2B_4O_7$ crystals

Elastooptic coefficient	p_{11}	p_{12}	p_{13}	p_{31}	p_{33}	p_{44}	p_{66}
Set 1 (one coefficient derived from one sample)	0.085 ±0.003	0.244 ±0.006	0.232 ±0.004	0.220 ±0.004	0.168 ±0.003	–0.0140 ±0.0049	–0.064 ±0.003
Set 2 (all samples, least-squares method)	0.081 ±0.003	0.211 ±0.005	0.223 ±0.003	0.199 ±0.003	0.158 ±0.003	–0.0014 ±0.0041	–0.067 ±0.002
Average value	0.083 ±0.003	0.227 ±0.017	0.227 ±0.005	0.209 ±0.011	0.163 ±0.006	–0.0075 ±0.0061	–0.066 ±0.002

APPENDIX A

CHANGES IN OPTICAL ANISOTROPY PARAMETERS IN CRYSTALLINE DISCS COMPRESSED ALONG DIAMETER

Point symmetry group	Disk cut	Loading force and mechanical stress tensor components	Induced birefringence and optical indicatrix rotation angle (equation number)
Cubic crystals			
432, $\bar{4}3m$, $m3m$	x	P_3, σ_2, σ_3, σ_4	$\Delta n_{23} = -\frac{1}{2} n^3 \left[\left(\pi_{11} - \pi_{12}\right)^2 \left(\sigma_2 - \sigma_3\right)^2 + 4\pi_{44}^2 \sigma_4^2 \right]^{\frac{1}{2}}$ (A1) $\tan 2\zeta_1 = \frac{2\pi_{44}\sigma_4}{\left(\pi_{11} - \pi_{12}\right)\left(\sigma_2 - \sigma_3\right)}$ (A2)
	y	P_3, σ_1, σ_3, σ_5	$\Delta n_{13} = -\frac{1}{2} n^3 \left[\left(\pi_{11} - \pi_{12}\right)^2 \left(\sigma_1 - \sigma_3\right)^2 + 4\pi_{44}^2 \sigma_5^2 \right]^{\frac{1}{2}}$ (A3) $\tan 2\zeta_2 = \frac{2\pi_{44}\sigma_5}{\left(\pi_{11} - \pi_{12}\right)\left(\sigma_1 - \sigma_3\right)}$ (A4)
	z	P_2, σ_1, σ_2, σ_6	$\Delta n_{12} = -\frac{1}{2} n^3 \left[\left(\pi_{11} - \pi_{12}\right)^2 \left(\sigma_1 - \sigma_2\right)^2 + 4\pi_{44}^2 \sigma_6^2 \right]^{\frac{1}{2}}$ (A5) $\tan 2\zeta_3 = \frac{2\pi_{44}\sigma_6}{\left(\pi_{11} - \pi_{12}\right)\left(\sigma_1 - \sigma_2\right)}$ (A6)
23, $m3$	x	P_3, σ_2, σ_3, σ_4	$\Delta n_{23} = -\frac{1}{2} n^3 \left[\begin{bmatrix} \left(\pi_{11} - \pi_{21}\right)\sigma_2 - \\ -\left(\pi_{11} - \pi_{12}\right)\sigma_3 \end{bmatrix}^2 + 4\pi_{44}^2 \sigma_4^2 \right]^{\frac{1}{2}}$ (A7) $\tan 2\zeta_1 = \frac{2\pi_{44}\sigma_4}{\left(\pi_{11} - \pi_{21}\right)\sigma_2 - \left(\pi_{11} - \pi_{12}\right)\sigma_3}$ (A8)
	y	P_3, σ_1, σ_3, σ_5	$\Delta n_{13} = -\frac{1}{2} n^3 \left[\begin{bmatrix} \left(\pi_{11} - \pi_{21}\right)\sigma_1 - \\ -\left(\pi_{11} - \pi_{12}\right)\sigma_3 \end{bmatrix}^2 + 4\pi_{44}^2 \sigma_5^2 \right]^{\frac{1}{2}}$ (A9)

Point symmetry group	Disk cut	Loading force and mechanical stress tensor components	Induced birefringence and optical indicatrix rotation angle (equation number)
			$\tan 2\zeta_2 = \dfrac{2\pi_{44}\sigma_5}{(\pi_{11}-\pi_{21})\sigma_1-(\pi_{11}-\pi_{12})\sigma_3}$ (A10)
	z	P_2, σ_1, σ_2, σ_6	$\Delta n_{12} = -\dfrac{1}{2}n^3\left[\begin{matrix}\left[(\pi_{11}-\pi_{21})\sigma_1-\right.\\ \left.-(\pi_{11}-\pi_{12})\sigma_2\right]^2\end{matrix}+4\pi_{44}^2\sigma_6^2\right]^{\frac{1}{2}}$ (A11)
			$\tan 2\zeta_3 = \dfrac{2\pi_{44}\sigma_6}{(\pi_{11}-\pi_{21})\sigma_1-(\pi_{11}-\pi_{12})\sigma_2}$ (A12)
Hexagonal and tetragonal crystals			
622, 6*mm*, $\bar{6}m2$, 6/*mmm*, 6, $\bar{6}$, 6/*m*, 422, 4*mm*, $\bar{4}2m$, 4/*mmm*, 4, $\bar{4}$, 4/*m*	x	P_3, σ_2, σ_3, σ_4	$\delta(\Delta n_{23}) = -\dfrac{1}{2}\left[\begin{matrix}n_o^3(\pi_{11}\sigma_2+\pi_{13}\sigma_3)-\\ -n_e^3(\pi_{31}\sigma_2+\pi_{33}\sigma_3)\end{matrix}\right]$ (A13)
			$\tan 2\zeta_1 = \dfrac{2n_o^2n_e^2\pi_{44}\sigma_4}{n_e^2-n_o^2+n_o^2n_e^2\left[\begin{matrix}(\pi_{11}-\pi_{31})\sigma_2+\\ +(\pi_{13}-\pi_{33})\sigma_3\end{matrix}\right]}$ (A14)
	y	P_3, σ_1, σ_3, σ_4	$\delta(\Delta n_{13}) = -\dfrac{1}{2}\left[\begin{matrix}n_o^3(\pi_{11}\sigma_1+\pi_{13}\sigma_3)-\\ -n_e^3(\pi_{31}\sigma_1+\pi_{33}\sigma_3)\end{matrix}\right]$ (A15)
			$\tan 2\zeta_2 = \dfrac{2n_o^2n_e^2\pi_{44}\sigma_5}{n_e^2-n_o^2+n_o^2n_e^2\left[\begin{matrix}(\pi_{11}-\pi_{31})\sigma_1+\\ +(\pi_{13}-\pi_{33})\sigma_3\end{matrix}\right]}$ (A16)
622, 6*mm*, $\bar{6}m2$, 6/*mmm*	z	P_2, σ_1, σ_2, σ_6	$\Delta n_{12} = -\dfrac{1}{2}n_o^3\pi_{66}\left[(\sigma_1-\sigma_2)^2+4\sigma_6^2\right]^{\frac{1}{2}}$ (A17)
			$\tan 2\zeta_3 = \dfrac{2\sigma_6}{(\sigma_1-\sigma_2)}$ (A18)
6, $\bar{6}$, 6/*m*			$\Delta n_{12} = -\dfrac{1}{2}n_o^3\left[\begin{matrix}\left[\pi_{66}(\sigma_1-\sigma_2)+4\pi_{62}\sigma_6\right]^2+\\ +4\left[\pi_{62}(\sigma_2-\sigma_1)+\pi_{66}\sigma_6\right]^2\end{matrix}\right]^{\frac{1}{2}}$ (A19)

Point symmetry group	Disk cut	Loading force and mechanical stress tensor components	Induced birefringence and optical indicatrix rotation angle (equation number)
			$\tan 2\zeta_3 = \dfrac{2\left[\pi_{62}(\sigma_2-\sigma_1)+\pi_{66}\sigma_6\right]}{\pi_{66}(\sigma_1-\sigma_2)+4\pi_{62}\sigma_6}$ (A20)
422, 4*mm*, $\bar{4}2m$, 4/*mmm*			$\Delta n_{12} = -\dfrac{1}{2}n_o^3\left[\left[(\pi_{11}-\pi_{12})\times\right]^2 + 4\pi_{66}^2\sigma_6^2\right]^{\frac{1}{2}}$ (A21) $\tan 2\zeta_3 = \dfrac{2\pi_{66}\sigma_6}{(\pi_{11}-\pi_{12})(\sigma_1-\sigma_2)}$ (A22)
4, $\bar{4}$, 4/*m*			$\Delta n_{12} = -\dfrac{1}{2}n_o^3\left[\begin{array}{l}\left[(\pi_{11}-\pi_{12})\times\right.\\ \left.\times(\sigma_1-\sigma_2)+2\pi_{16}\sigma_6\right]^2 + \\ +4\left[\pi_{61}(\sigma_1-\sigma_2)+\pi_{66}\sigma_6\right]^2\end{array}\right]^{\frac{1}{2}}$ (A23) $\tan 2\zeta_3 = \dfrac{2\left[\pi_{61}(\sigma_1-\sigma_2)+\pi_{66}\sigma_6\right]}{(\pi_{11}-\pi_{12})(\sigma_1-\sigma_2)+2\pi_{16}\sigma_6}$ (A24)
Trigonal crystals			
32, 3*m*, $\bar{3}m$	*x*	P_3, σ_2, σ_3, σ_4	$\delta(\Delta n_{23}) = -\dfrac{1}{2}\left[\begin{array}{l}n_o^3(\pi_{11}\sigma_2+\pi_{13}\sigma_3-\pi_{14}\sigma_4)- \\ -n_e^3(\pi_{31}\sigma_2+\pi_{33}\sigma_3)\end{array}\right]$ (A25) $\tan 2\zeta_1 =$ $= \dfrac{2n_o^2n_e^2(\pi_{44}\sigma_4-\pi_{41}\sigma_2)}{n_e^2-n_o^2+n_o^2n_e^2\left[\begin{array}{l}(\pi_{11}-\pi_{31})\sigma_2+ \\ +(\pi_{13}-\pi_{33})\sigma_3-\pi_{14}\sigma_4\end{array}\right]}$ (A26)
	y	P_3, σ_1, σ_3, σ_5	$\delta(\Delta n_{13}) = -\dfrac{1}{2}\left[\begin{array}{l}n_o^3(\pi_{11}\sigma_1+\pi_{13}\sigma_3)- \\ -n_e^3(\pi_{31}\sigma_1+\pi_{33}\sigma_3)\end{array}\right]$ (A27) $\tan 2\zeta_2 = \dfrac{2n_o^2n_e^2\pi_{44}\sigma_5}{n_e^2-n_o^2+n_o^2n_e^2\left[\begin{array}{l}(\pi_{11}-\pi_{31})\sigma_1+ \\ +(\pi_{13}-\pi_{33})\sigma_3\end{array}\right]}$ (A28)
	z	P_2, σ_1, σ_2, σ_6	$\Delta n_{12} = -\dfrac{1}{2}n_o^3\pi_{66}\left[(\sigma_1-\sigma_2)^2+4\sigma_6^2\right]^{\frac{1}{2}}$ (A29)

Point symmetry group	Disk cut	Loading force and mechanical stress tensor components	Induced birefringence and optical indicatrix rotation angle (equation number)
			$\tan 2\zeta_3 = \dfrac{2\sigma_6}{(\sigma_1 - \sigma_2)}$ (A30)
3, $\bar{3}$	*x*	P_3, σ_2, σ_3, σ_4	$\delta(\Delta n_{23}) = -\dfrac{1}{2}\left[\begin{matrix} n_o^3(\pi_{11}\sigma_2 + \pi_{13}\sigma_3 - \pi_{14}\sigma_4) - \\ -n_e^3(\pi_{31}\sigma_2 + \pi_{33}\sigma_3) \end{matrix}\right]$ (A31)
			$\tan 2\zeta_1 = \dfrac{2n_o^2 n_e^2(\pi_{44}\sigma_4 - \pi_{41}\sigma_2)}{n_e^2 - n_o^2 + n_o^2 n_e^2\left[\begin{matrix}(\pi_{11} - \pi_{31})\sigma_2 + \\ +(\pi_{13} - \pi_{33})\sigma_3 - \pi_{14}\sigma_4\end{matrix}\right]}$ (A32)
	y	P_3, σ_1, σ_3, σ_5	$\delta(\Delta n_{13}) = -\dfrac{1}{2}\left[\begin{matrix} n_o^3(\pi_{11}\sigma_1 + \pi_{13}\sigma_3 - \pi_{25}\sigma_5) - \\ -n_e^3(\pi_{31}\sigma_1 + \pi_{33}\sigma_3) \end{matrix}\right]$ (A33)
			$\tan 2\zeta_2 = \dfrac{2n_o^2 n_e^2(\pi_{44}\sigma_5 - \pi_{52}\sigma_1)}{n_e^2 - n_o^2 + n_o^2 n_e^2\left[\begin{matrix}(\pi_{11} - \pi_{31})\sigma_1 + \\ +(\pi_{13} - \pi_{33})\sigma_3 - \pi_{25}\sigma_5\end{matrix}\right]}$ (A34)
	z	P_2, σ_1, σ_2, σ_6	$\Delta n_{12} = -\dfrac{1}{2}n_o^3\left[\begin{matrix}\left[\pi_{66}(\sigma_1 - \sigma_2) + 4\pi_{62}\sigma_6\right]^2 + \\ +4\left[\pi_{62}(\sigma_2 - \sigma_1) + \pi_{66}\sigma_6\right]^2\end{matrix}\right]^{\frac{1}{2}}$ (A35)
			$\tan 2\zeta_3 = \dfrac{2(\pi_{62}(\sigma_2 - \sigma_1) + \pi_{66}\sigma_6)}{\pi_{66}(\sigma_1 - \sigma_2) + 4\pi_{62}\sigma_6}$ (A36)
Orthorhombic and monoclinic crystals*			
222, *mm*2, *mmm*, 2, *m*, 2/*m*	*x*	P_3, σ_2, σ_3, σ_4	$\delta(\Delta n_{23}) = -\dfrac{1}{2}\left[\begin{matrix} n_2^3(\pi_{22}\sigma_2 + \pi_{23}\sigma_3) - \\ -n_3^3(\pi_{32}\sigma_2 + \pi_{33}\sigma_3) \end{matrix}\right]$ (A37)
			$\tan 2\zeta_1 = \dfrac{2n_2^2 n_3^2 \pi_{44}\sigma_4}{n_3^2 - n_2^2 + n_2^2 n_3^2\left[\begin{matrix}(\pi_{22} - \pi_{32})\sigma_2 + \\ +(\pi_{23} - \pi_{33})\sigma_3\end{matrix}\right]}$ (A38)
	y	P_3, σ_1, σ_3, σ_5	$\delta(\Delta n_{13}) = -\dfrac{1}{2}\left[\begin{matrix} n_1^3(\pi_{11}\sigma_1 + \pi_{13}\sigma_3) - \\ -n_3^3(\pi_{31}\sigma_1 + \pi_{33}\sigma_3) \end{matrix}\right]$ (A39)

Point symmetry group	Disk cut	Loading force and mechanical stress tensor components	Induced birefringence and optical indicatrix rotation angle (equation number)
			$\tan 2\zeta_2 = \dfrac{2n_1^2 n_3^2 \pi_{55}\sigma_5}{n_3^2 - n_1^2 + n_1^2 n_3^2 \begin{bmatrix} (\pi_{11}-\pi_{31})\sigma_1 + \\ +(\pi_{13}-\pi_{33})\sigma_3 \end{bmatrix}}$ (A40)
222, *mm*2, *mmm*	*z*	P_2, σ_1, σ_2, σ_6	$\delta(\Delta n_{12}) = -\dfrac{1}{2}\begin{bmatrix} n_1^3(\pi_{11}\sigma_1 + \pi_{12}\sigma_2) - \\ -n_2^3(\pi_{21}\sigma_1 + \pi_{22}\sigma_2) \end{bmatrix}$ (A41)
			$\tan 2\zeta_3 = \dfrac{2n_1^2 n_2^2 \pi_{66}\sigma_6}{n_2^2 - n_1^2 + n_1^2 n_2^2 \begin{bmatrix} (\pi_{11}-\pi_{21})\sigma_1 + \\ +(\pi_{12}-\pi_{22})\sigma_2 \end{bmatrix}}$ (A42)
2, *m*, 2/*m*			$\delta(\Delta n_{12}) = -\dfrac{1}{2}\begin{bmatrix} n_1^3(\pi_{11}\sigma_1 + \pi_{12}\sigma_2 + \pi_{16}\sigma_6) - \\ -n_2^3(\pi_{21}\sigma_1 + \pi_{22}\sigma_2 + \pi_{26}\sigma_6) \end{bmatrix}$ (A43)
			$\tan 2\zeta_3 = \dfrac{2n_1^2 n_2^2(\pi_{61}\sigma_1 + \pi_{62}\sigma_2 + \pi_{66}\sigma_6)}{n_2^2 - n_1^2 + n_1^2 n_2^2 \begin{bmatrix} (\pi_{11}-\pi_{21})\sigma_1 + \\ +(\pi_{12}-\pi_{22})\sigma_2 + \\ +(\pi_{16}-\pi_{26})\sigma_6 \end{bmatrix}}$ (A44)
Triclinic crystals			
1, $\bar{1}$	*x*	P_3, σ_2, σ_3, σ_4	$\delta(\Delta n_{23}) = -\dfrac{1}{2}\begin{bmatrix} n_2^3(\pi_{22}\sigma_2 + \pi_{23}\sigma_3 + \pi_{24}\sigma_4) - \\ -n_3^3(\pi_{32}\sigma_2 + \pi_{33}\sigma_3 + \pi_{34}\sigma_4) \end{bmatrix}$ (A45)
			$\tan 2\zeta_1 = \dfrac{2(\pi_{42}\sigma_2 + \pi_{43}\sigma_3 + \pi_{44}\sigma_4)}{\left(\dfrac{1}{n_2^2} - \dfrac{1}{n_3^2}\right) + \begin{bmatrix} (\pi_{22}-\pi_{32})\sigma_2 + \\ +(\pi_{23}-\pi_{33})\sigma_3 + \\ +(\pi_{24}-\pi_{34})\sigma_4 \end{bmatrix}}$ (A46)
	y	P_3, σ_1, σ_3, σ_5	$\delta(\Delta n_{13}) = -\dfrac{1}{2}\begin{bmatrix} n_1^3(\pi_{11}\sigma_1 + \pi_{13}\sigma_3 + \pi_{15}\sigma_5) - \\ -n_3^3(\pi_{31}\sigma_1 + \pi_{33}\sigma_3 + \pi_{35}\sigma_5) \end{bmatrix}$ (A47)
			$\tan 2\zeta_2 = \dfrac{2(\pi_{51}\sigma_1 + \pi_{53}\sigma_3 + \pi_{55}\sigma_5)}{\left(\dfrac{1}{n_1^2} - \dfrac{1}{n_3^2}\right) + \begin{bmatrix} (\pi_{11}-\pi_{31})\sigma_1 + \\ +(\pi_{13}-\pi_{33})\sigma_3 + \\ +(\pi_{15}-\pi_{35})\sigma_5 \end{bmatrix}}$ (A48)

Point symmetry group	Disk cut	Loading force and mechanical stress tensor components	Induced birefringence and optical indicatrix rotation angle (equation number)
	z	P_2, σ_1, σ_2, σ_6	$\delta(\Delta n_{12}) = -\frac{1}{2}\begin{bmatrix} n_1^3(\pi_{11}\sigma_1 + \pi_{12}\sigma_2 + \pi_{16}\sigma_6) - \\ -n_2^3(\pi_{21}\sigma_1 + \pi_{22}\sigma_2 + \pi_{26}\sigma_6) \end{bmatrix}$ (A49) $\tan 2\zeta_3 = \frac{2(\pi_{61}\sigma_1 + \pi_{62}\sigma_2 + \pi_{66}\sigma_6)}{\left(\frac{1}{n_1^2} - \frac{1}{n_2^2}\right) + \begin{bmatrix} (\pi_{11} - \pi_{21})\sigma_1 + \\ +(\pi_{12} - \pi_{22})\sigma_2 + \\ +(\pi_{16} - \pi_{26})\sigma_6 \end{bmatrix}}$ (A50)

* These ratios are valid only for crystals belonging to the monoclinic system $2 \| z$ and $m \perp z$.

BIBLIOGRAPHY

1. Brewster, D. (1815). Experiments on the depolarization of light as exhibited by various mineral, animal, and vegetable bodies, with a reference to the general principles of polarization. Phil. Trans. R. Soc. Lond. B, 104, 187–211.
2. Brewster, D. (1816). On the communication of the structure of doubly refracting crystals to glass, muriate of soda, fluor spar, and other substances, by mechanical compression and dilatation. Phil. Trans. R. Soc. Lond., 106, 156–178.
3. Faraday, M. (1933). Faraday's Diary. Volume IV, Nov. 12, 1839-June 26, 1847. (Thomas Martin ed.). London: George Bell and Sons, paragraphs #7504, 13 Sept. 1845–#7718, 30 Sept. 1845.
4. Kerr, J. (1875). XL. A new relation between electricity and light: Dielectrified media birefringent. The London, Edinburgh, and Dublin Phil. Mag. Journ. Sc., 50(332), 337–348.
5. Pockels, F. (1894). Ueber den Einfluss des elektrostatischen Feldes auf das optische Verhalten piëzoelektrischer Krystalle (Vol. 39). Dieterichsche Verlags-Buchhandlung.
6. Pockels, F. C. A. (1906). Lehrbuch der kristalloptik (Vol. 19). BG Teubner, Leipzig.
7. Vlokh, O. G. (1970). Elektrooptychna aktyvnist krystaliv kvartsu [Electro-optical activity of quartz crystals]. Ukrainskyi Fizychnyi Zhurnal [Ukrainian Journal of Physics], 15(5), 758–762.
8. Vlokh, O. G., Zheludev, I. S. (1960). Izmenenie opticheskih svoystv kristallov pri nalozhenii elektricheskih poley (Lineynyiy elektrooptycheskiy effekt) [Changes in the optical properties of crystals upon application of electric fields (Linear electro-optical effect)]. Kristallografiya [Crystallography], 5(3), 390–402.
9. Vlokh, O. G. (1965). Deformatsiia optychnykh indykatrys pry kvadratychnomu ta spontannomu elektrooptychnykh efektakh u krystalakh [Deformation of optical indicatrixes under quadratic and spontaneous electro-optical effects in crystals]. Ukrainskyi Fizychnyi Zhurnal [Ukrainian Journal of Physics], X(10), 1101–1117.
10. Tang, Y., Burdick, N. Q., Baumann, K., & Lev, B. L. (2015). Bose–Einstein condensation of ^{162}Dy and ^{160}Dy. New Journ. Phys., 17(4), 045006.

11. Grakh, I. I., & Mozhanskaya, A. F. (1971). A type of mechanically anisotropic, optically sensitive material. Polym. Mech., 7(5), 747–751.
12. Weber, H. J. (1995). Determination of internal strain by optical measurements. Phys. Rev. B, 51(18), 12209.
13. Aben, H. K. (1975). Integralnaya fotouprugost [Integral Photoelasticity]. Tallinn: Valgus.
14. Narasimhamurty, T. S. (1981). Photoelastic and electro-optic properties of crystals. Plenum Press, New York.
15. Slezinger, I. I., Alievskaya, A. N., & Mironov, Y. V. (1985). Piezooptic devices. Meas. Techn., 28(12), 1059–1062.
16. Spillman, W. B. (1982). Multimode fiber-optic accelerometer based on the photoelastic effect. Appl. Opt., 21(15), 2653–2655.
17. Su, W., Gilbert, J. A., Morrissey, M. D., & Song, Y. (1997). General-purpose photoelastic fiber optic accelerometer. Opt. Engin., 36(1), 22–29.
18. Aben, H., & Errapart, A. (2012). Photoelastic Tomography with Linear and Non-linear Algorithms. Exp. Mech., 52(8), 1179–1193.
19. Ainola, L., & Aben, H. (2004). On the optical theory of photoelastic tomography. Journ. Opt. Soc. Am. A, 21(6), 1093–1101.
20. Andirenko, Y. A., & Dubovikov, M. S. (1994). Optical tomography of tensor fields. Journ. Opt. Soc. Am, 1628–1631.
21. Schupp, D. (1997, September). Determination of 3D stress by optical sensor field tomography. In Optical Inspection and Micromeasurements II (Vol. 3098, pp. 431-442). International Society for Optics and Photonics.
22. Schupp, D. (1999, October). Determination of the 3D stress tensor in photoelastic materials by optical tensor field tomography. In Optical Diagnostics for Fluids/Heat/Combustion and Photomechanics for Solids (Vol. 3783, pp. 56–68). International Society for Optics and Photonics.
23. Billardon, M., & Badoz, J. (1966). Birefringence modulator. CR Acad. Sci. Ser. B, 262, 1672–1675.
24. Kemp, J. C. (1969). Piezo-optical birefringence modulators: new use for a long-known effect. Journ. Opt. Soc. Am., 59(8), 950–954.
25. Auld, B. A. (1990). Acoustic fields and waves in solids: RE Krieger. Malabar, Florida.
26. Balakshiy, V. I., Paryigin, V. N., & Chirkov, L. E. (1985). Fizicheskie osnovyi akustooptiki [Physical foundations of acousto-optics]. Moscow: Radio i svyaz.

27. Xu, J., & Stroud, R. (1992). Acousto-optic devices: principles, design, and applications (Vol. 12). Wiley-Interscience.
28. Shaskolskaya, M. P. (1982). Akusticheskie kristallyi [Acoustic crystals]. Moscow: Nauka.
29. Optical Glass–Collection Datasheets. (Jan 2017). SCHOTT Advanced Optics. http://www.schott.com/d/advanced_optics/ac85c64c-60a0-4113-a9df-23ee1be20428/1.3/schott-optical-glass-collection-datasheets-english-17012017.pdf. Accessed 25 Jan 2018.
30. Opticheskoye steklo TF8. Tekhnicheskaya informatsiya [Optical glass TF8. Technical information]. (May 2021). Joint-Stock Company "Lytkarino Optical Glass Factory". http://lzos.ru/upload/iblock/818/818322c0e82195aba7b3c9b1441649b9.pdf. Accessed 26 May 2021.
31. Frocht, M. M. Photoelasticity. Volume 1 (1948). New York: J. Wiley & Sons.
32. TIE-27: Stress in optical glass. (July 2004). SCHOTT Technical Information. http://www.schott.com/d/advanced_optics/1275dc1e-ef01-45d1-a88a-79deec322443/1.1/schott_tie-27_stress_in_optical_glass_us.pdf. Accessed 25 Jan 2018.
33. McKenzie, H. W., & Hand, R. J. (1999). Basic optical stress measurement in glass (Vol. 900682272). Sheffield: Society of Glass Technology.
34. International Organization for Standardization. (1995). Raw optical glass–Determination of birefringence (ISO Standard No. 11455:1995).
35. Kasatkin, B. S., Kudrin, A. B., Lobanov, L. M., Pivtorak, V. A., Poluhin, P. I., & Chichenev, N. I. (1981). Eksperimentalnyie metodyi issledovaniya deformatsiy i napryazheniy [Experimental Methods for Studying Deformations and Stresses]. Kiev: Naukova dumka.
36. Aleksandrov, A. Ya., & Ahmetzyanov, M. H. (1973). Polyarizatsionno-opticheskiye metody mekhaniki deformiruyemogo tela [Polarization-optical methods of deformable body mechanics]. Moscow: Nauka.
37. Kihara, T. (1990). Automatic whole-field measurement of photoelasticity using linear polarized incident light. In Proc. of IX Int. Conf. Exp. Mech., Copenhagen (Vol. 2, pp. 821–827).
38. Kihara, T. (1989). Automatic whole-field measurement of relative retardation and principal axes using circular-polarized incident light. In Proc. Jap. Soc. Photoel. (Vol. 9, pp. 1–8).

39. Kihara, T. (1994). Automatic whole-field measurement of principal stress directions using three wavelengths. In Proc. of the 10th Int. Conf. Exp. Mech., Lisbon (pp. 95–99).
40. Voloshin, A. S., & Burger, C. P. (1983). Half-fringe photoelasticity: a new approach to whole-field stress analysis. Exp. Mech., 23(3), 304–313.
41. Ramji, M., & Ramesh, K. (2008). Whole field evaluation of stress components in digital photoelasticity – Issues, implementation and application. Opt. Las. Engin., 46(3), 257–271.
42. Patterson, E. A. (2002). Digital photoelasticity: principles, practice and potential. Strain, 38(1), 27–39.
43. Dora, P. T., & Ramesh, K. (2014, June). Measurement of residual birefringence in thin glass plates using digital photoelasticity. In Int. Conf. Exp. Mech. 2013 and Twelfth Asian Conf. Exp. Mech. (Vol. 9234, p. 92340J). International Society for Optics and Photonics.
44. Krupych, O. M, Berezhnyy I. V., Vlokh, O. G. (1998). Avtomatychnyy polyarymetr matrytsi Dzhonsa tsiloho polya zobrazhennya [Automatic polarimeter of the Jones matrix of the whole image field]. Visnyk Natsional′noho universytetu “L′vivs′ka politekhnika” [Journal of Lviv Polytechnic National University], 348, 3–11.
45. Krupych, O. M, Berezhnyy I. V., Vlokh, O. G., Vlokh, R. O. (2003) Polyarymetr zobrazhennya. Deklaratsiynyy patent na vynakhid [Image polarimeter. Declaratory patent for an invention] № 58696 A. 10.07.2002–15.08.2003, Bull. №8.
46. Ajmera, P. K., Huner, B., Dutta, A. K., & Hartley, C. S. (1988). Simulation and observation of infrared piezobirefringent images in diametrically compressed semiconductor disks. Appl. Opt., 27(4), 752–757.
47. Andrushchak, A. S., Bobitski, Y. V., Kaidan, M. V., Mytsyk, B. G., Kityk, A. V., & Schranz, W. (2005). Two-fold interferometric measurements of piezo-optic constants: application to β-BaB_2O_4 crystals. Opt. Las. Techn., 37(4), 319–328.
48. Mys, O., Adamiv, V., Martynyuk-Lototska, I., Burak, Y., & Vlokh, R. (2007). Piezooptic and acoustic properties of $KLiB_4O_7$ crystals. Ukr. J. Phys. Opt., 8(3), 138–142.
49. Mytsyk, B. G. (2012). Fotopruzhnist′ anizotropnykh materialiv [Photoelasticity of anisotropic materials]. Lviv: Liga-Press.
50. Vasylkiv, Y., Kvasnyuk, O., Krupych, O., Mys, O., Maksymuk, O., & Vlokh, R. (2009). Reconstruction of 3D stress fields basing on piezooptic experiment. Ukr. J. Phys. Opt., 10(1), 22–37.

51. Opticheskoye steklo K8. Tekhnicheskaya informatsiya [Optical glass K8. Technical information]. (May 2021). Joint-Stock Company "Lytkarino Optical Glass Factory". http://lzos.ru/upload/iblock/818/818322c0e82195aba7b3c9b1441649b9.pdf. Accessed 26 May 2021.
52. Coefficients of Friction for Glass. (2005) The Physics Factbook. Ed. Glenn Elert. http://hypertextbook.com/facts/2005/glass.shtml. Accessed 25 Jan 2018.
53. Bayda, E. N. (1983) Nekotoryye prostranstvennyye zadachi teorii uprugosti [Some spatial problems of the theory of elasticity]. Leningrad: LGU.
54. Kvasnyuk, O., Vasylkiv, Y., Krupych, O., & Vlokh, R. (2014). Preferable geometrical parameters of samples for piezooptic experiments. Ukr. J. Phys. Opt., 15(4), 195–206.
55. Frocht, M. M. Photoelasticity. Volume 2 (1948). New York: J. Wiley & Sons.
56. Savaryn, V., Skab, I., Krupych, O., & Vlokh, R. (2012). The method for measuring piezooptic coefficients of crystals using a crystalline disk loaded along its diameter. Ukr. J. Phys. Opt., 13(2), 82–124.
57. Savaryn, V., Krupych, O., Skab, I., & Vlokh, R. (2014). Reinvestigation of piezooptic anisotropy appearing in a crystalline disk loaded along its diameter. Ukr. J. Phys. Opt., 15(2), 84–95.
58. Vasylkiv, Y., Savaryn, V., Smaga, I., Krupych, O., Skab, I., & Vlokh, R. (2011). Studies of piezooptic coefficients in $LiNbO_3$ crystals using a crystalline disk compressed along its diameter. Ukr. J. Phys. Opt., 12(4), 180–190.
59. Savaryn, V., Krupych, O., & Vlokh, R. (2014). Refined measurements of piezooptic coefficient π_{66} for the lithium niobate crystals, using a crystalline disk compressed along its diameter. Ukr. J. Phys. Opt., 15(1), 30–37.
60. Mytsyk, B. G., Andrushchak, A. S., Demyanyshyn, N. M., Kost, Y. P., Kityk, A. V., Mandracci, P., & Schranz, W. (2009). Piezo-optic coefficients of MgO-doped $LiNbO_3$ crystals. Applied Optics, 48(10), 1904–1911.
61. Weis, R. S., & Gaylord, T. K. (1985). Lithium niobate: summary of physical properties and crystal structure. Appl. Phys. A, 37(4), 191–203.
62. Krupych, O., Savaryn, V., Skab, I., & Vlokh, R. (2011). Interferometric measurements of piezooptic coefficients by means of four-point bending method. Ukr. J. Phys. Opt., 12(3), 150–160.

63. Krupych, O., Savaryn, V., Krupych, A., Klymiv, I., & Vlokh, R. (2013). Determination of piezo-optic coefficients of crystals by means of four-point bending. Appl. Opt., 52(17), 4054–4061.
64. Krupych, O., Savaryn, V., & Vlokh, R. (2014). Precise determination of full matrix of piezo-optic coefficients with a four-point bending technique: the example of lithium niobate crystals. Appl. Opt., 53(10), B1–B7.
65. Peng, H. J., Wong, S. P., Ho, H. P., Zhao S. (2004). Measurement of orientation dependent stress-optic coefficient of GaAs single crystal. Appl. Phys. Lett., 84, 1829–1831.
66. Mytsyk, B. (2003). Methods for the studies of the piezo-optical effect in crystals and the analysis of experimental data. I. Methodology for the studies of piezo-optical effect. Ukr. J. Phys. Opt., 4(1), 1–26.
67. Mytsyk, B. (2003). Methods for the studies of the piezo-optical effect in crystals and the analysis of experimental data. II. Analysis of experimental data. Ukr. J. Phys. Opt., 4(3), 105–118.
68. Sirotin, Yu. I., Shaskolskaya, M. P. (1979). Osnovy kristallofiziki [Fundamentals of crystal physics]. Moscow: Nauka.
69. ASTM C770-98(2008) Standard test method for measurement of glass stress-optical coefficient.: ASTM International. 2012, 15.02. 622 p. http://www.astm.org/Standards/C770.htm.
70. Dixon, R. W., Cohen, M. G. (1966). A new technique for measuring magnitudes of photoelastic tensors and its application to lithium niobate. Appl. Phys. Lett., 8, 205–207.
71. Dixon, R. W. (1967). Photoelastic properties of selected materials and their relevance for application to acoustic light modulators and scanners. Appl. Phys., 38, 5149–5153.
72. Skab, I., Smaga, I., Savaryn, V., Vasylkiv, Yu., Vlokh, R. (2011). Torsion method for measuring piezooptic coefficients. Cryst. Res. Technol., 46(1), 23–36.
73. Skab, I., Vasylkiv, Yu., Savaryn, V., Vlokh, R. (2010). Relations for optical indicatrix parameters in the conditions of crystal torsion. Ukr. J. Phys. Opt., 11(4), 193–240.
74. Alexeyev, C. N., Borshak, E. V., Volyar, A. V., Yavorsky, M. A. (2009). Angular momentum conservation and coupled vortex modes in twisted optical fibres with torsional stress. J. Opt. A: Pure Appl. Opt., 11(9), 094011–094018.
75. Vasylkiv, Yu., Savaryn, V., Smaga, I., Skab, I., Vlokh, R. (2010). Determination of piezooptic coefficient π_{14} of $LiNbO_3$ crystals under torsion loading. Ukr. J. Phys. Opt., 11(3), 156–164.

76. Vlokh, R., Krupych, O., Kostyrko, M., Netolya, V., Trach, I. (2001). Gradient thermooptical effect in $LiNbO_3$ crystals. Ukr. J. Phys. Opt., 2(3), 154–158.
77. Kaufmann, S., Zeitner, U. (2002). Unambigous measuring of great retardations with a modified Senarmont method. Optik–Int. Journ. Light El. Opt., 113(11), 476–480.
78. Lithium niobate, $LiNbO_3$. Almaz Optics, Inc. 2011. http://www.almazoptics.com/LiNbO3.htm.
79. Mytsyk, B. G., Andrushchak, A. S. (1990). Neodnoznachnost' vybora kristallofizicheskoy sistemy koordinat pri izuchenii p'yezoopticheskogo effekta na primere kristallov $LiNbO_3$ [Ambiguity in the choice of the crystallophysic coordinate system in the study of the piezo-optical effect on the example of $LiNbO_3$ crystals]. Kristallografiya [Crystallography], 35(6), 1574–1575.
80. Mytsyk, B. G., Demyanyshyn, N. M. (2006). P'yezoopticheskiye poverkhnosti kristallov niobata litiya [Piezo-optical surfaces of lithium niobate crystals]. Kristallografiya [Crystallography], 51(4), 693–700.
81. Vasylkiv, Yu., Savaryn, V., Smaga, I., Skab, I., Vlokh, R. (2011). On determination of sign of the piezooptic coefficients using torsion method. Appl. Opt., 50(17), 2512–2518.
82. Martynyuk-Lototska, I., Mys, O., Dudok, T., Adamiv, V., Smirnov, Ye., Vlokh, R. (2008). Acousto-optic interaction in α-BaB_2O_4 and $Li_2B_4O_7$ crystals. Appl. Opt., 47, 3446–3454.
83. Kato, K. Second-harmonic generation to 2048 Å in BaB_2O_4. (1986). IEEE J. Quant. Electron., 22, 1013–1014.
84. Ishida, Y., Yajima, T. (1987). Characteristics of a new-type SHG crystal β-BaB_2O_4 in the femtosecond region. Opt. Comm., 62, 197–200.
85. Cheng, L. K., Bosenberg, W., Tang, C. L. (1988). Broadly tunable optical parametric oscillation in β-BaB_2O_4. Appl. Phys. Lett., 53, 175–177.
86. Chen, C. T., Wu, B. C., Jiang, A. D., You, G. M. (1985). A new ultraviolet SHG crystal β-BaB_2O_4. Sci. Sin. (Ser. B)., 28, 235–243.
87. Yoshida, H., Fujita, H., Nakatsuka, M., Yoshimura, M., Sasaki, T., Kamimura, T., Yoshida, K. (2006). Dependences of laser-induced bulk damage threshold and crack patterns in several nonlinear crystals on irradiation direction. Japan. J. Appl. Phys., 45, 766–769.
88. Vlokh, R. O., Pyatak, Y. A., Skab, I. P. (1992). Pro oriyentuvannya krystaliv serednikh synhoniy [On the orientation of crystals of

middle syngonies]. Ukrainskyi Fizychnyi Zhurnal [Ukrainian Journal of Physics], 37(2), 207–210.

89. Timoshenko, S. P. (1965). Soprotivleniye materialov [Strength of materials]. Moscow: Nauka.
90. Steklo K8. List dannykh [Glass K8. Data sheet]. (May 2021). State enterprise “Izyum Instrument-Making Plant”. http://ipz.com.ua/datasheet/K8_rus.pdf. Accessed 26 May 2021.
91. Mytsyk, B. G., Andrushchak, A. S., Has′kevych H. I. (2007). Povne vyvchennya p’yezooptychnoho efektu v krystallakh lanhasytu [Complete study of the piezooptical effect in langasite crystals]. Ukrainskyi Fizychnyi Zhurnal [Ukrainian Journal of Physics], 8, 800–809.
92. Weber, M. J. (2002). Handbook of optical materials (Vol. 19). Boca Raton, FL: CRC press.
93. N-BK7 Optical Glass Datasheet. (Jan 2014). SCHOTT Advanced Optics. http://www.schott.com/advanced_optics/us/abbe_datasheets/schott-datasheet-n-bk7.pdf. Accessed 25 Jan 2018.
94. Vlokh, R., Pyatak, Y., & Skab, I. (1992). Elastooptic effect in $LiNbO_3$ under crystal bending. Ferroelectrics, 126(1), 239–242.
95. Adamiv, V., Teslyuk, I., Dyachok, Y., Romanyuk, G., Krupych, O., Mys, O., Martynyuk-Lototska, I., Burak, Ya., & Vlokh, R. (2010). Synthesis and optical characterization of $LiKB_4O_7$, $Li_2B_6O_{10}$, and $LiCsB_6O_{10}$ glasses. Appl. Opt., 49(28), 5360–5365.
96. Adamiv, V., Teslyuk, I., Dyachok, Y., Romanyuk, G., Krupych, O., Mys, O., Martynyuk-Lototska, I., Burak, Ya., & Vlokh, R. (2014). Synthesis and optical characterization of $LiKB_4O_7$, $Li_2B_6O_{10}$, and $LiCsB_6O_{10}$ glasses: erratum. Appl. Opt., 53(20), 4481–4482.
97. Smith, R. T., & Welsh, F. S. (1971). Temperature dependence of the elastic, piezoelectric, and dielectric constants of lithium tantalate and lithium niobate. Journ. Appl. Phys., 42(6), 2219–2230.
98. Bechmann, R., & Fair, I. E. (1958). IRE standards on piezoelectric crystals: determination of the elastic, piezoelectric, and dielectric constants-the electromechanical coupling factor. Proc. IRE, 46, 764–778.
99. Standards on piezoelectric crystals. (1949). Proc. IRE, 37, 1378–1395.
100. Mytsyk, B., Demyanyshyn, N., Martynyuk-Lototska, I., & Vlokh, R. (2011). Piezo-optic, photoelastic, and acousto-optic properties of SrB_4O_7 crystals. Appl. Opt., 50(21), 3889–3895.

101. Andrushchak, A. S., Mytsyk, B. G., Laba, H. P., Yurkevych, O. V., Solskii, I. M., Kityk, A. V., & Sahraoui, B. (2009). Complete sets of elastic constants and photoelastic coefficients of pure and MgO-doped lithium niobate crystals at room temperature. Journ. Appl. Phys., 106(7), 73510.
102. Avakyants, L. P., Kiselev, D. F., & Shchitov, N. N. (1976). Fotouprugost' $LiNbO_3$ [Photoelasticity of $LiNbO_3$]. Fizika Tverdogo Tela [Physics of the Solid State], 18, 1547–1551.
103. Krupych, O., Kushnirevych, M., Mys, O., & Vlokh, R. (2015). Photoelastic properties of $NaBi(MoO_4)_2$ crystals. App. Opt., 54(16), 5016–5023.
104. Haussühl, S., Liebertz, J., & Schmidt, H. (1991). Crystal growth and elastic properties of tetragonal $NaBi(MoO_4)_2$. Cryst. Res. Techn., 26(6), K136–K140.
105. Antonenko, A. M., Stolpakova, T. M. (1984). Akusticheskiye svoyctva kristallov $NaBi(MoO_4)_2$ [Acoustic properties of $NaBi(MoO_4)_2$ crystals]. Ukrainskyi Fizychnyi Zhurnal [Ukrainian Journal of Physics], 29(4), 612–614.
106. Martynyuk-Lototska, I., Mys, O., Kushnirevych, M., Krupych, O., & Vlokh, R. (2015). Acoustic anisotropy for acoustooptic $NaBi(MoO_4)_2$ crystals. Ukr. J. Phys. Opt., 16(2), 69–76.
107. Akimov, S. V., Stolpakova, T. M., Dudnik, E. F., Sinyakov, E. V. (1977). Fotouprugiye svoystva $NaBi(MoO_4)_2$ [Photoelastic properties of $NaBi(MoO_4)_2$]. Fizika Tverdogo Tela [Physics of the Solid State], 19(9), 1832–1833.
108. Podgórska, D., Kaczmarek, S. M., Drozdowski, W., Berkowski, M., & Worsztynowicz, A. (2005). Growth and optical properties of $Li_2B_4O_7$ single crystals pure and doped with Yb, Co and Mn ions for nonlinear applications. Acta Phys. Pol. A, 107(3), 507–518.
109. Shiosaki, T., Adachi, M., Kobayashi, H., Araki, K., & Kawabata, A. (1985). Elastic, piezoelectric, acousto-optic and electro-optic properties of $Li_2B_4O_7$. Jap. Journ. Appl. Phys., 24(S1), 25–27.
110. Krupych, O., Mys, O., Kryvyy, T., Adamiv, V., Burak, Ya., & Vlokh, R. (2016). Photoelastic properties of lithium tetraborate crystals. App. Opt., 55(36), 10457–10462.
111. Sugawara, T., Komatsu, R., & Uda, S. (1998). Linear and nonlinear optical properties of lithium tetraborate. Sol. St. Commun., 107(5), 233–237.
112. Martynyuk-Lototska, I., Mys, O., Adamiv, V., Burak, Ya., & Vlokh, R. (2002). Elastical, piezooptical and acoustooptical properties of lithium tetraborate crystals. Ukr. J. Phys. Opt., 3(4), 264–266.

113. Bohaty, L., Haussühl, S., & Liebertz, J. (1989). Electrooptical coefficients and temperature and pressure derivatives of the elastic constants of tetragonal $Li_2B_4O_7$. Cryst. Res. Techn., 24(11), 1159–1163.